

This dissertation has been
microfilmed exactly as received 68-14,212

TINNEY, Joseph Fredrick, 1937-
THE APPLICATION OF X-RAY FLUORESCENCE TO
IN-VIVO BIOLOGICAL STUDIES.

The University of Oklahoma, Ph.D., 1968
Biology-Genetics

University Microfilms, Inc., Ann Arbor, Michigan

THE UNIVERSITY OF OKLAHOMA

GRADUATE COLLEGE

THE APPLICATION OF X-RAY FLUORESCENCE TO
IN-VIVO BIOLOGICAL STUDIES

A DISSERTATION

SUBMITTED TO THE GRADUATE FACULTY

in partial fulfillment of the requirements for the

degree of

DOCTOR OF PHILOSOPHY

BY

JOSEPH FREDRICK TINNEY

Norman, Oklahoma

1968

THE APPLICATION OF X-RAY FLUORESCENCE TO IN-VIVO
BIOLOGICAL STUDIES

APPROVED BY

Robert W. Evans

Winfield W. Evans

Harry J. Kearn, M.D.

Stewart H. Kleber

DISSERTATION COMMITTEE

ACKNOWLEDGMENT

It is a pleasure to acknowledge indebtedness to the many individuals that made this study possible. In particular, appreciation is extended to Dr. Robert Y. Nelson for his valuable criticisms and helpful suggestions during his direction of the study.

Mr. Jamie Shotts, Mr. Harold Cook, Mr. Johnny James, and Mr. Ivan Meeks assisted in the construction of the experimental equipment, health physics monitoring, and accumulation of the data.

The financial assistance provided by the Bendix Corporation during the program is gratefully acknowledged. Special thanks are also due the Civil Defense Organization of Oklahoma for supplying the x-ray equipment that was used for the experimental studies.

Finally, I wish to express my sincere thanks and appreciation to my wife, Garlan, for providing continuous encouragement and understanding during my entire university program.

TABLE OF CONTENTS

	Page
LIST OF TABLES	vi
LIST OF ILLUSTRATIONS	vii
 Chapter	
1. INTRODUCTION	1
2. THEORETICAL CONSIDERATIONS	3
2.1. Narrow-Beam Primary Source-Narrowbeam Detector Geometry	3
2.1.1 Fluorescent X-Ray Intensity	5
2.1.2 Scattered Radiation Intensity	10
2.1.3 Radiation Dose Considerations	15
2.1.4 Detector Collimation	16
2.2. Narrow Beam Primary Source-Wide Beam Detector Geometry	22
2.3. X-Ray Physics	27
2.3.1 K-Fluorescence Yield	28
2.3.2 K-Absorption Jump Ratio	28
2.3.3 Absorption, Attenuation, and Scattering Coefficients . .	36
2.4. Dependence of Fluorescent X-Ray Intensity on Excitation Source - Biological System - and Fluorescent X-Ray De- tector Parameters	48
2.4.1 Dependence of Fluorescent X-Ray Intensity on Tracer Element Atomic Number	52
2.4.2 Dependence of Fluorescent X-Ray Intensity on Tracer Element Concentration	56
2.4.3 Dependence of Fluorescent X-Ray Intensity on Excitation Energy	63
2.4.4 Defect Localization	74

	Page
2.5. Fluorescent X-Ray to Single Compton Scatter X-Ray Intensity Ratio	76
2.6. Comparison with Conventional Radioisotope Studies	77
2.6.1 Dynamic Function Studies	78
2.6.2 Radioisotope Scanning	80
2.7. Primary X-Ray Source Considerations	84
2.8. Radiation Detector Considerations	89
3. EXPERIMENTAL VERIFICATION	93
3.1. Experimental Equipment	94
3.1.1 Excitation Source	94
3.1.2 Biological Phantoms	96
3.1.3 X-Ray Detector	99
3.1.4 Scanner	103
3.1.5 Signal Processing and Readout	103
3.2. Experimental Procedure	106
3.2.1 Concentration Sensitivity Measurements	106
3.2.2 Defect Localization	112
3.2.3 Dosimetry	115
4. DATA REDUCTION AND EXPERIMENTAL RESULTS	117
4.1. Dependence of Fluorescent X-Ray Intensity on Tracer Element Concentration and Organ Depth	117
4.2. Dependence of Fluorescent X-Ray Intensity on Excitation Energy	127
4.3. Defect Localization	131
5. SUMMARY	136
6. LIST OF REFERENCES	138

LIST OF TABLES

Table	Page
2-1. Measured and calculated values of K-fluorescence yield w_k^Z	29
2-2. Measured and calculated values of K-absorption jump ratio r_k^Z	33
2-3. Mass absorption and attenuation coefficients for iodine ($z = 53$)	43
2-4. Mass scattering and attenuation coefficients for water . .	45
2-5. Mass energy absorption coefficients for water.	46
2-6. Gamma-ray emitting radiopharmaceuticals used for scanning.	81
2-7. X-ray and gamma-ray sources.	88
4-1. Example iodine K X-ray intensity data.	119

LIST OF ILLUSTRATIONS

Figure	Page
2-1. General experimental configuration for calculating fluorescent X-ray intensity.	4
2-2. Experimental configuration for scattered radiation intensity calculations	11
2-3. System with horizontal resolution determined by detector collimator	17
2-4. System with horizontal resolution determined by primary radiation beam	18
2-5. Configuration for simultaneously determining concentration distributions at several depths.	19
2-6. Narrow beam source - wide-beam detector geometry	23
2-7. Notation for wide-beam detector geometry calculations.	25
2-8. Comparison of observed and calculated values of fluorescent yield.	32
2-9. Comparison of observed and calculated values of K-absorption jump ratio	37
2-10. Photon intensity per unit surface dose rate as a function of photon energy.	47
2-11. Dependence of $I_k^z/I_1 \cdot 4\pi R^2/A_1$, I_k^z/D , and C_k^z/D on tracer element atomic number for an excitation beam energy of 100 keV.	53
2-12. Dependence of $I_k^z/I_1 \cdot 4\pi R^2/A_1$ on tracer element atomic number for an excitation beam energy that just exceeds the tracer element K-absorption edge energy.	54
2-13. Dependence of I_k^z/K and C_k^z/D on tracer element atomic number for an excitation beam energy that just exceeds the tracer element K-absorption edge energy	55
2-14. Dependence of $I_k^z(4\pi R^2) / I_1 A_1$ on concentration for several tracker elements	57
2-15. Dependence of C_k^z/D and I_k^z/D on concentration for several tracker elements	58

Figure	Page
2-16. Dependence of $I_k^z(4\pi R^2)/I_1 A_1$, I_k^z/D , and C_k^z/D on iodine concentration for several organ depths	59
2-17. Dependence of $I_k^z(4\pi R^2)/I_1 A_1$, I_k^z/D , and C_k^z/D on iodine concentration for several organ thicknesses.	60
2-18. Dependence of $I_k^z(4\pi R^2)/I_1 A_1$ on excitation energy for several high-z elements.	65
2-19. Dependence of C_k^z/D and I_k^z/D on excitation energy for several high-z elements.	66
2-20. Dependence of C_k^z/D on excitation energy for several organ depths	67
2-21. Change in I_k^z as source-detector assembly passes over 1.0 cm "hot spot" defect in 3.0 cm thick organ.	68
2-22. Change in I_k^z as source-detector assembly passes over 1.0 cm "hot spot" defect in 1.0 cm thick organ.	69
2-23. Scheme for producing uniform depth sensitivity	70
3-1. Photograph of assembled x-ray machine.	95
3-2. Attenuation of tungsten target continuous spectrum	97
3-3. Photograph of biological phantom used for concentration sensitivity studies.	98
3-4. "Hot spot" defects phantom construction.	100
3-5. "Cold spot" defect phantom construction.	101
3-6. Construction of multihole focused collimator	102
3-7. Theoretical point source response for lateral displacement in focus plane	104
3-8. Photograph of modified chromatogram scanner.	105
3-9. Dimensional schematic of source - Biological-phantom-detector geometry used for concentration sensitivity measurements	107
3-10. Functional block diagram of experimental system for concentration sensitivity measurements	108
3-11. Photograph of the experimental area for concentration sensitivity measurements.	110

Figure	Page
3-12. Photograph of X-ray machine control and data acquisition area	111
3-13. Dimensional layout of defect scanning geometry	113
3-14. Functional block diagram of defect scanning system	114
3-15. Geometries used for dosimetry measurements	116
4-1. Iodine K X-ray count ratio as a function of iodine concentration for several sample depths.	118
4-2. Dependence of air dose rate on distance from X-ray tube target	121
4-3. Iodine K X-ray count per unit surface dose as a function of iodine concentration for several sample depths.	122
4-4. Geometry for calculating effective collimator resolution area	124
4-5. Measured excitation source X-ray spectrum and spectrum corrected to 35 cm source-detector distance.	126
4-6. Dependence of iodine K X-ray count rate on X-ray machine KV setting	128
4-7. Dependence of Air dose rate on X-ray machine KV setting. . .	130
4-8. Variation of iodine K X-ray count per unit surface dose with X-ray machine KV setting.	132
4-9. Linear scans of "hot spot" defect phantom.	133
4-10. Linear scans of "cold spot" defect phantom	134

CHAPTER I

INTRODUCTION

Historically, radioactive isotopes have been used to study organ circulation, function, and structure in vivo. Sophisticated radiation detectors and data processing systems have been developed for these studies. Advanced pharmaceutical techniques which permit higher selective uptake of radioactive tracers by the organ or tissue being studied have also evolved. Despite these advances, however, several limitations still exist. First, the patient must be given a radioactive material that must concentrate in the organ before measurements can begin, and second, after the measurements are completed, the patient will continue to receive a radiation dose until the radioisotope decays or is eliminated from the body. Since only small doses of radioactive material can be safely administered, the patient is frequently required to remain stationary for a long period of time to obtain statistically significant measurements. Blurring, introduced by organ motion, cannot presently be eliminated and poor defect resolution is obtained when the heart, lungs, etc. are studied.

Ideally, it would be desirable to eliminate the use of internally administered radioactive materials for these studies and to obtain the required data in a short period of time. A technique that may satisfy these idealistic objectives for some types of investigations involves the use of fluorescent X-rays.

When an atom is excited by the removal of an electron from an inner atomic orbit, it will subsequently undergo a transition to a lower energy level. The excess energy associated with this transition is carried away from the atom by either an "Auger" electron or a fluorescent X-ray photon. All elements yield fluorescent X-rays when exposed to sufficiently energetic sources of ionizing radiation and the energies of these X-rays are directly related to the atomic number of the element in which they are produced.

Several elements that could be used as nonradioactive tracers for in vivo biological studies have fluorescent X-rays in the energy range from about 17 keV (Mo) to 79 keV (Au). These energies are much higher than those produced in the major constituents of soft tissue (less than 4 keV) and are comparable to the gamma and X-ray energies of some radioisotopes, such as I-125 and Hg-197, that are normally used for these types of investigations. Thus, it should be possible to determine the concentration and concentration distribution of a high-Z tracer element in a biological system that is irradiated by a sufficiently energetic excitation source and "viewed" by an energy sensitive X-ray detector.

This research program was initiated to examine theoretically and experimentally the possibility of using fluorescent X-rays to study organ circulation, function, and structure in vivo. To accomplish this objective, several parameters associated with the biological system, the excitation source, the fluorescent X-ray detector, and the geometrical configuration of these components were investigated to determine their influence on concentration sensitivity and defect resolution as a function of radiation dose.

SECTION 2

THEORETICAL CONSIDERATIONS

2.1 NARROW BEAM PRIMARY SOURCE - NARROW BEAM DETECTOR GEOMETRY

If fluorescent X-rays emitted by high-Z tracer elements are to be useful for in vivo studies, several factors influencing concentration sensitivity, resolution, and radiation absorbed dose must be investigated and, where possible, optimized. These include the following:

1. The nature of the biological system including the size, shape, composition and physiological characteristics of the organ (or tissue) of interest; the size, shape and composition of any "defects" in the organ and the composition and thickness of the material surrounding the organ. Defect, as used in this context, refers to a region containing a higher or lower concentration of tracer element Z than the adjacent organ or tissue material.
2. The energy spectrum, intensity, cross-sectional area and shape of the primary radiation beam.
3. The size, shape, efficiency, and energy discrimination of the fluorescent X-ray detector.
4. The various geometrical factors associated with the experimental configuration of the primary radiation source, the biological system, and the X-ray detector.
5. The atomic properties of the constituent elements of the biological system.

The manner in which these factors influence concentration sensitivity, resolution, and radiation absorbed dose can be determined from the theoretical analysis of the generalized experimental configuration presented in Figure 2-1. The calculation procedures used in this section are similar to those introduced by Compton (Ref. 1) and expanded by Blokhin (Ref. 2) and (Ref. 3).

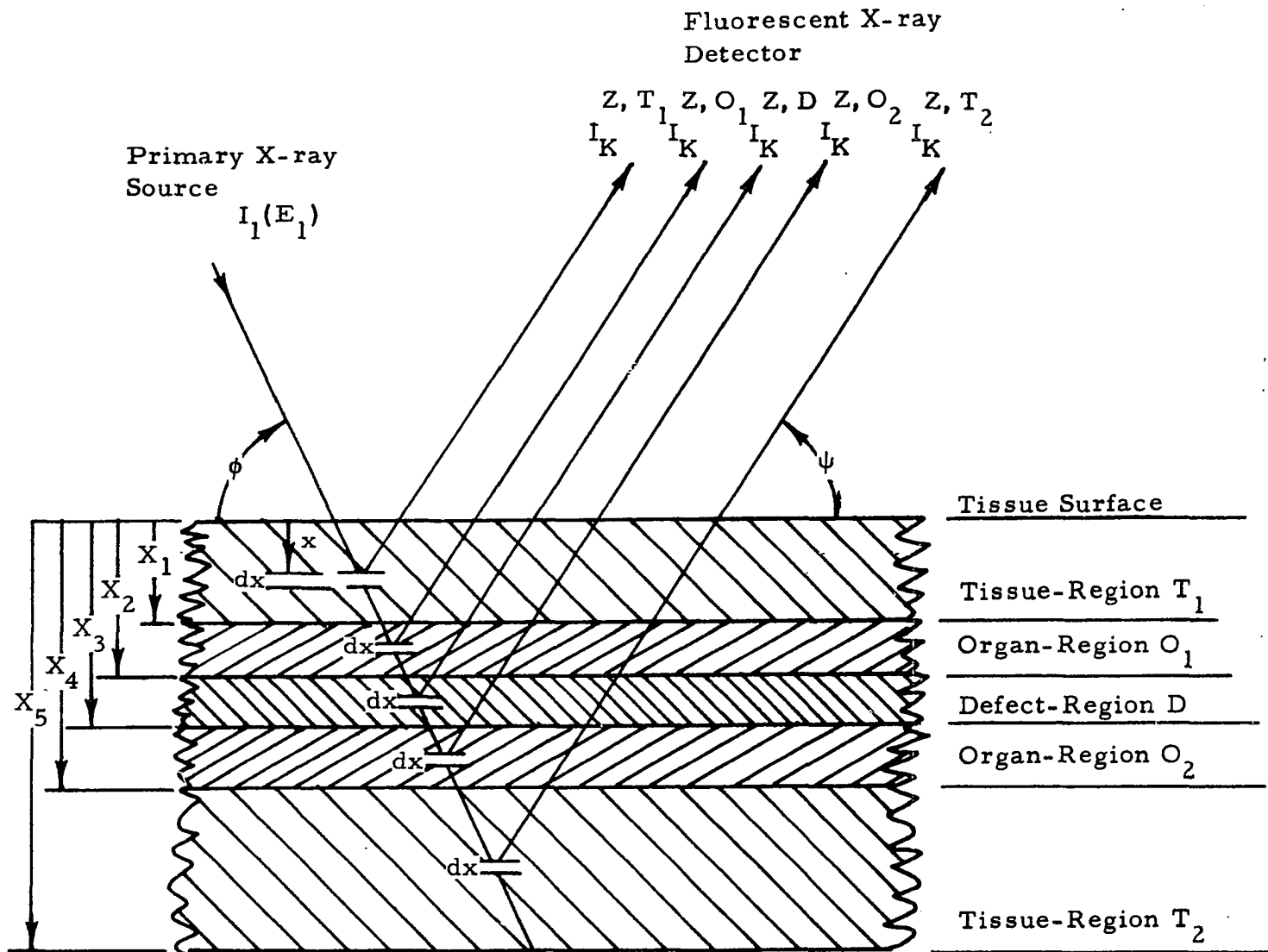


Figure 2-1 Generalized Experimental Configuration for Calculating Fluorescent X-Ray Intensity

2.1.1 Fluorescent X-Ray Intensity

The biological system illustrated in Figure 2-1 is considered a tissue slab containing an organ with a defect. It is assumed that the organ is a plane-parallel slab of thickness $X_4 - X_1$ at a depth X_1 in an otherwise continuous slab of tissue of thickness X_5 . The defect in the organ is a slab of thickness $X_4 - X_3$ at a depth X_3 . Using the notation, the analysis will be limited to cases for which $0 < X_1 < X_2 < X_3 < X_4 < X_5$. For convenience, the biological system has been divided into five regions designated by T_1 , O_1 , D , O_2 , and T_2 . It is further assumed that each region of the biological system is composed of a mechanical mixture of a high-Z tracer element, Z , and a tissue equivalent material W .

Referring to Figure 2-1, the biological system is irradiated by a well collimated-narrow beam of X-rays of intensity I_1 , area A_1 , and energy E_1 incident on the tissue surface at an angle ϕ . The fluorescent X-rays emitted by tracer element Z are measured at an exit angle ψ .

As the primary X-ray beam passes through the biological system to a depth x , it will be attenuated along the path $x/\sin \phi$ in the overburden material. In the differential segment dx at x , primary beam interactions will excite some atoms of element Z to the K level and these atoms will subsequently emit the entire K series fluorescent spectrum of element Z . Fluorescent X-rays with an exit angle ψ are attenuated in the overburden material along the path $x/\sin \psi$.

To limit the complexity of the calculations at this point, it will be assumed that the fluorescent X-ray detector is located at a distance R from dx which is large compared to the thickness of the biological system, the diameter of the primary beam, and the diameter of the detector. This restriction will be imposed to obtain the expression for the tracer element K series fluorescent X-ray intensity at the detector surface, I_K^Z , which does not involve exponential integrals. However, this restriction will be removed in a subsequent section of this report for the analysis of a system which uses a wide beam detector geometry.

At a depth x in region, T_1 of the biological system, the intensity of the primary X-ray beam, $I_1^{T_1}(x)$, is:

$$I_1^{T_1}(x) = I_1 e^{-\mu_1^T x/\sin \phi} \quad (\text{photons/cm}^2\text{-sec}) \quad (2-1)$$

where:

I_1 = primary radiation beam intensity at the tissue surface
(photons/cm²-sec)

μ_1^T = linear attenuation coefficient of primary radiation in tissue
(cm⁻¹)

In the incremental layer dx the primary X-ray beam intensity will decrease by:

$$dI_1^T(x) = -I_1^T(x) \mu_1^T \frac{dx}{\sin \phi} \quad (\text{photons/cm}^2\text{-sec}) \quad (2-2)$$

where dx/sin ϕ is the attenuation path length in dx. This decrease in intensity will result from scattering as well as absorption. However, here we are only interested in the absorption component, and the linear attenuation coefficient μ_1^T in Equation 2-2 can be replaced by the linear absorption coefficient τ_1^T . Scattering interactions will be treated in a subsequent section.

Since I_1 is the number of photons per cm² per sec in a beam of area A_1 , the number of photons per sec incident on dx will be $I_1^T(x) A_1 / \sin \phi$ and the number of primary photons absorbed per sec by all atoms in the layer dx, $dN_1^T(x)$, will be:

$$dN_1^T(x) = \frac{I_1^T(x) A_1 \tau_1^T dx}{\sin^2 \phi} \quad (\text{photons/sec}) \quad (2-3)$$

To obtain the number of tracer element K-level absorptions per sec in dx, $(dN_1^{Z, T1}(x))_K$, the tissue linear absorption coefficient, τ_1^T , in Equation 2-3 must be replaced by the element Z linear absorption coefficient $\tau_1^{Z, T}$ and multiplied by $(r_K^Z - 1)/r_K^Z$, where r_K^Z is the absorption jump ratio of the K-absorption edge of element Z. With these substitutions, Equation 2-3 can be rewritten as:

$$(dN_1^{Z, T1}(x))_K = \frac{I_1^T(x) A_1 \tau_1^{Z, T}}{\sin^2 \phi} \cdot \frac{r_K^Z - 1}{r_K^Z} \cdot dx \quad (\text{photons/sec}) \quad (2-4)$$

Substituting Equation 2-1 for $I_1^{Z, T_1}(x)$ in Equation 2-4, we get:

$$(dN_1^{Z, T_1}(x))_K = \frac{I_1 e^{-\mu_1^T x/\sin\phi} A_1 \tau_1^{Z, T}}{\sin^2 \phi} \cdot \frac{r_K^{Z-1}}{r_K^Z} \cdot dx \text{ (photons/sec)} \quad (2-5)$$

Due to the Auger effect, all K-level absorptions in tracer element Z will not result in the production of K series fluorescent X-rays. Therefore, to obtain the number of element Z atoms per sec in dx emitting K-series fluorescent X-rays, $(dN_1^{Z, T_1}(x))_{K, f}$, equation 2-5 must be multiplied by the K fluorescence yield, ω_K^Z , or:

$$(dN_1^{Z, T_1}(x))_{K, f} = \frac{I_1 A_1 \tau_1^{Z, T} \omega_K^Z}{\sin^2 \phi} \cdot \frac{r_K^{Z-1}}{r_K^Z} \cdot e^{-\mu_1^T x/\sin\phi} dx \text{ (photons/sec)} \quad (2-6)$$

By considering $(dN_1^{Z, T_1}(x))_{K, f}$ as a point source at a depth x in the biological system, the intensity of tracer element K X-rays at a detector distance R, $dI_K^{Z, T}$, can be obtained from the equation:

$$dI_K^{Z, T} = \frac{(dN_1^{Z, T_1}(x))_{K, f}}{4\pi R^2} \cdot e^{-\mu_K^T x/\sin\psi} \text{ (photons/cm}^2\text{-sec)} \quad (2-7)$$

where:

μ_K^T = linear attenuation coefficient of tracer element K X-rays in tissue

$\frac{x}{\sin\psi}$ = attenuation path length in overburden tissue

The total tracer element K-series fluorescent X-ray intensity at R from region T_1 of the biological system, I_K^{Z, T_1} , can now be determined by substituting Equation 2-6 for $(dN_1^{Z, T_1}(x))_{K, f}$ in Equation 2-7 and integrating over x from $x = 0$ to $x = X_1$.

$$I_{K}^{Z, T_1} = \frac{I_1 A_1 \tau_1^{Z, T} \omega_K^Z}{4\pi R^2 \sin^2 \phi} \cdot \frac{r_K^Z - 1}{r_K^Z} \cdot \int_0^{X_1} e^{-\left(\frac{\mu_1^T}{\sin \phi} + \frac{\mu_K^T}{\sin \psi}\right) x} dx \quad (2-8)$$

or:

$$I_{K}^{Z, T_1} = B \frac{\tau_1^{Z, T}}{\alpha^T} \left[1 - e^{-\alpha^T X_1} \right] \text{ (photons/cm}^2\text{-sec)} \quad (2-9)$$

where:

$$B = \frac{I_1 A_1 \omega_K^Z}{4\pi R^2 \sin^2 \phi} \cdot \frac{r_K^Z - 1}{r_K^Z}$$

$$\alpha^T = \frac{\mu_1^T}{\sin \phi} + \frac{\mu_K^T}{\sin \psi}$$

A similar procedure can be used to determine the intensity of tracer element K X-rays at R from regions O_1 , D, O_2 , and T_2 . However, for these regions the primary and secondary X-rays will be attenuated by overburden materials of different compositions.

An examination of Figure 2-1 and Equation 2-8 shows that the tracer element K X-ray intensity at R from region O_1 of the biological system, I_{K}^{Z, O_1} , can be obtained from the following equation:

$$I_{K}^{Z, O_1} = + \frac{I_1 A_1 \tau_1^{Z, O} \omega_K^Z}{4\pi R^2 \sin^2 \phi} \cdot \frac{r_K^Z - 1}{r_K^Z} \cdot e^{-\left(\frac{\mu_1^T}{\sin \phi} + \frac{\mu_K^T}{\sin \psi}\right) X_1} \int_{X_1}^{X_2} e^{-\left(\frac{\mu_1^O}{\sin \phi} + \frac{\mu_K^O}{\sin \psi}\right) x} dx \quad (2-10)$$

where:

- $\tau_1^{Z, O}$ = linear absorption coefficient of primary radiation in tracer element Z in the organ
- μ_1^O = linear attenuation coefficient of primary radiation in the organ
- μ_K^O = linear attenuation coefficient of tracer element K X-rays in the organ.

When the integration over x is completed, Equation 2-10 becomes:

$$I_{K}^{Z, O_1} = \frac{B \tau_1^{Z, O} e^{-\alpha^T X_1}}{\alpha^O} \left[1 - e^{-\alpha^O (X_2 - X_1)} \right] \quad (2-11)$$

where:

$$\alpha^O = \frac{\mu_1^O}{\sin \phi} + \frac{\mu_K^O}{\sin \psi}$$

Similarly, the tracer element K X-ray intensities at R from regions D, O_2 , and T_2 are:

$$I_{K}^{Z, D} = B \frac{\tau_1^{Z, D}}{\alpha^D} \cdot e^{-\alpha^T X_1 - \alpha^O (X_2 - X_1)} \left[1 - e^{-\alpha^D (X_3 - X_2)} \right] \quad (2-12)$$

$$I_{K}^{Z, O_2} = B \frac{\tau_1^{Z, O}}{\alpha^O} \cdot e^{-\alpha^T X_1 - \alpha^O (X_2 - X_1) - \alpha^D (X_3 - X_2)} \left[1 - e^{-\alpha^O (X_4 - X_3)} \right] \quad (2-13)$$

$$I_{K}^{Z, T_2} = B \frac{\tau_1^{Z, T}}{\alpha^T} \cdot e^{-\alpha^T X_1 - \alpha^O (X_2 - X_1) - \alpha^D (X_3 - X_2) - \alpha^O (X_4 - X_3)} \left[1 - e^{-\alpha^T (X_5 - X_4)} \right] \quad (2-14)$$

where:

- $\tau_1^{Z, D}$ = linear absorption coefficient of primary radiation in tracer element Z in the defect
- μ_1^D = linear attenuation coefficient of primary radiation in the defect
- μ_K^D = linear attenuation coefficient of tracer element K X-rays in the defect

$$\alpha^D = \frac{\mu_1^D}{\sin\phi} + \frac{\mu_K^D}{\sin\psi}$$

The tracer element K X-ray intensity at R from the entire biological system I_K^Z is the sum of the contributions from the five regions, or

$$I_K^Z = B \left\{ \begin{aligned} & \frac{\tau_1^{Z,T}}{\alpha^T} \left(1 - e^{-\alpha^T X_1} + e^{-\alpha^T X_1 - \alpha^O(X_2 - X_1) - \alpha^D(X_3 - X_2) - \alpha^O(X_4 - X_3)} \left[1 - e^{-\alpha^T(X_5 - X_4)} \right] \right) \\ & + \frac{\tau_1^{Z,O}}{\alpha^O} \left(e^{-\alpha^T X_1} \left[1 - e^{-\alpha^O(X_2 - X_1)} \right] + e^{-\alpha^T X_1 - \alpha^O(X_2 - X_1) - \alpha^D(X_3 - X_2)} \left[1 - e^{-\alpha^O(X_4 - X_3)} \right] \right) \\ & + \frac{\tau_1^{Z,D}}{\alpha^D} \cdot e^{-\alpha^T X_1 - \alpha^O(X_2 - X_1)} \left[1 - e^{-\alpha^D(X_3 - X_2)} \right] \end{aligned} \right\} \quad (2-15)$$

To obtain the tracer element K X-ray count rate, C_K^Z , from a detector located at R, I_K^Z must be multiplied by the detector efficiency for element Z K X-rays, ϵ_K^Z , and the detector area A_2 .

$$C_K^Z = I_K^Z \epsilon_K^Z A_2$$

2.1.2 Scattered Radiation Intensity

2.1.2.1 Single Compton Scattering

Since the Compton mass scattering coefficient is only slightly dependent on the atomic number of the scattering material, varying approximately as $Z^{-0.13}$, and relatively low concentrations of the high-Z tracer element will be present in the biological system, the single Compton scattered radiation intensity can be calculated by assuming that the biological system is a slab of tissue of thickness X_5 .

Referring to Figure 2-2, the intensity of the primary X-ray beam, $I_1^T(x)$, at a depth x in the biological system will be:

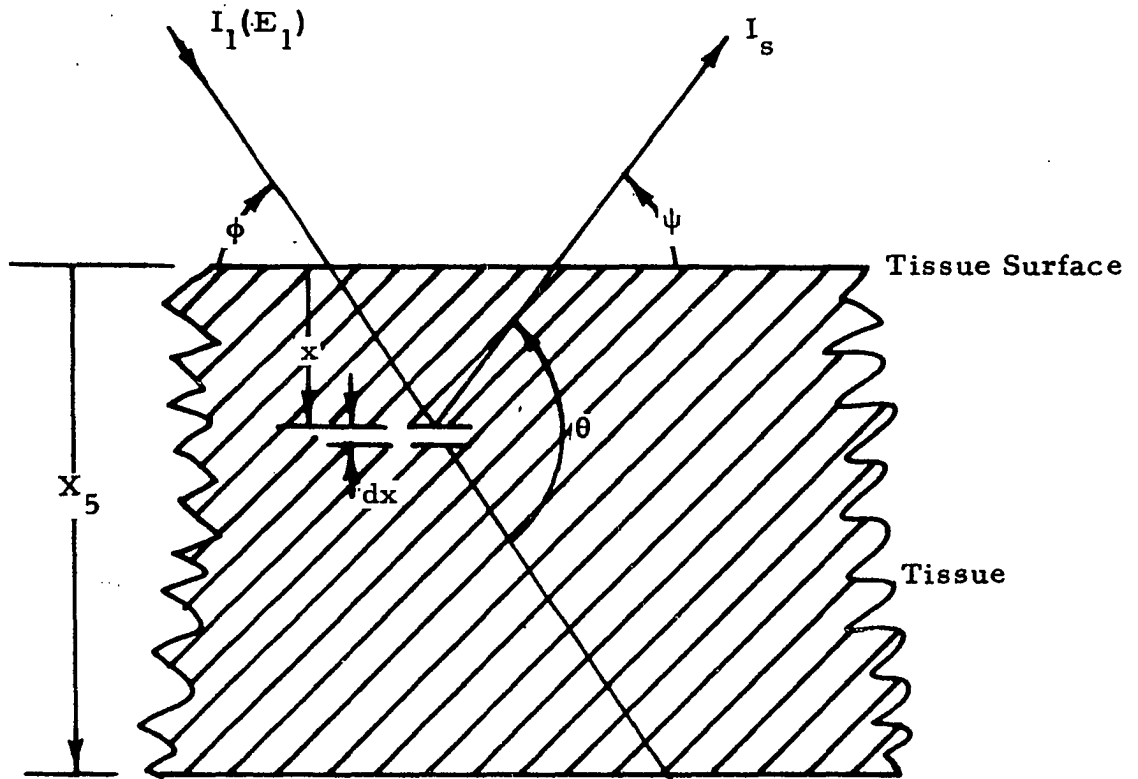


Figure 2-2 Experimental Configuration for Scattered Radiation Intensity Calculations

$$I_1^T(x) = I_1 e^{-\mu_1^T x / \sin\phi} \quad (\text{photons / cm}^2 \text{-sec}) \quad (2-17)$$

and the primary X-ray beam intensity decrease in the layer dx , will be given by the equation

$$dI_1^T(x) = -I_1^T(x) \cdot \frac{dx}{\sin\phi} \quad (\text{photons / cm}^2 \text{-sec}) \quad (2-18)$$

where the superscript T refers to tissue. Since I_1 is the number of photons per cm^2 per sec in a primary beam of area A_1 , the number of primary photons scattered per sec in the layer dx , $(dN_1^T(x))_S$, is:

$$(dN_1^T(x))_S = \frac{I_1^T(x) A_1 \sigma_1^T dx}{\sin^2 \phi} \quad (\text{photons / sec}) \quad (2-19)$$

where the linear attenuation coefficient μ_1^T has been replaced by the linear scattering coefficient of the primary radiation in tissue, σ_1^T .

The number of photons per second scattered in dx through an angle θ , $(dN_1^T(x))_{S, \theta}$, is given by:

$$(dN_1^T(x))_{S, \theta} = \frac{I_1 A_1 e^{-\mu_1^T x / \sin\phi} \sigma_1^T}{\sin^2 \phi} \cdot \frac{3(1 + \cos^2 \theta)}{16\pi} dx \quad (2-20)$$

where $I_1^T(x)$ has been replaced by Equation 2-17 and $3(1 + \cos^2 \theta)/16\pi$ is the probability that a scattered photon will be deflected through an angle θ . Compton scattered photons with an exit angle ψ will be attenuated along the path $x/\sin\psi$ and the single Compton scattered radiation intensity, dI_S , at a detector located a distance R from dx will be:

$$dI_S = \frac{I_1 A_1 \sigma_1^T}{4\pi R^2 \sin^2 \phi} \frac{3(1 + \cos^2 \theta)}{16\pi} e^{-\left(\frac{\mu_1^T}{\sin \phi} + \frac{\mu_S^T}{\sin \psi}\right) x} dx \quad (\text{photons / cm}^2\text{-sec}) \quad (2-21)$$

where μ_S^T = linear attenuation coefficient of scattered radiation in tissue,

$$R \gg X_5 \gg A_1$$

$$\theta = \phi + \psi$$

The total single Compton scattered radiation intensity at the detector can be obtained by integrating Equation 2-21 over x from $x = 0$ to $x = X_5$.

$$I_S = \frac{I_1 A_1 \sigma_1^T}{4\pi R^2 \sin^2 \phi} \left[\frac{3(1 + \cos^2 \theta)}{16\pi} \int_0^{X_5} e^{-\left(\frac{\mu_1^T}{\sin \phi} + \frac{\mu_S^T}{\sin \psi}\right) x} dx \right] \quad (2-22)$$

or:

$$I_S = L \sigma_1^T \left[\frac{1 - e^{-\beta^T X_5}}{\beta^T} \right] \quad (\text{photons / cm}^2\text{-sec}) \quad (2-23)$$

where:

$$L = \frac{I_1 A_1}{4\pi R^2 \sin^2 \phi} \left[\frac{3(1 + \cos^2 \theta)}{16\pi} \right], \quad \beta^T = \frac{\mu_1^T}{\sin \phi} + \frac{\mu_S^T}{\sin \psi}$$

From Compton's equation, the energy of a scattered photon that undergoes a single diffusion through an angle θ is:

$$E_S = \frac{E_1}{\left[1 + \frac{E_1}{510} (1 - \cos \theta) \right]} \quad (\text{kev}) \quad (2-24)$$

where E_1 and E_S are given in kev.

The single Compton scatter count rate, C_S from a detector located at R is the product of I_S , the detector efficiency for scattered radiation ϵ_S , and the detector area A_2 .

$$C_S = I_S \epsilon_S A_2 \quad (\text{counts/sec}) \quad (2-25)$$

In a subsequent section of this paper, it will be shown that single Compton scattered radiation provides a means of obtaining a tracer element concentration measurement that is independent of the matrix composition and density of the region of the biological system being examined.

2.1.2.2 Multiple Compton Scattering

The energy spectrum and the angular distribution of multiple Compton scattered photons is best determined by Monte Carlo techniques. Since these photons only contribute to the background radiation level and do not contain information related directly to the concentration of the tracer element in the biological system, calculations of their intensity contribution at the detector have not been attempted. Instead, it has been assumed that the background radiation intensity can be determined experimentally and accounted for in the data reduction procedure.

2.1.2.3 Rayleigh Scattering

The total Rayleigh scattering cross-section is much smaller than the total Compton cross-section per atom, the ratio between the two being approximately (Ref. 4): *

$$\frac{\sigma_{\text{Rayleigh}}}{\sigma_{\text{Compton}}} \approx 1.1 \times 10^{-2} \frac{Z^{5/3}}{E_0} \quad (2-26)$$

where E_0 is given in kev.

*References are listed in Section 6.

Since the energies of interest in this application are greater than 20 kev and the effective atomic number of tissue is about 7, the Rayleigh to Compton scattering ratio per atom will have a maximum value of about 0.014.

2.1.3 Radiation Dose Considerations

One of the primary considerations, in evaluating the usefulness of high-Z tracer element fluorescent X-rays for in vivo studies, is the radiation dose that must be delivered to the biological system to obtain a statistically significant fluorescent X-ray count. This will depend on the resolution required, the properties of the biological system, the energy of the primary X-ray beam, the geometrical factors associated with the experiment, and the characteristics of the fluorescent X-ray detector.

An equation will be developed in this section, for determining the number of photons per square cm required to produce a surface dose of 1 mrad (millirad) as a function of primary X-ray energy. This equation will be used in subsequent sections for the analysis of some particular source-biological system-detector configurations.

The energy absorbed per sec in one gram of tissue, E_{1-abs}^T , from a primary X-ray beam of energy E_1 kev and intensity I_1 photons per cm^2 per sec is given by the equation:

$$E_{1-abs}^T = E_1 I_1 (\mu_{m-abs})_1^T \sin \phi \text{ (kev/g-sec)} \quad (2-27)$$

where $(\mu_{m-abs})_1^T$ = mass energy absorption coefficient for primary X-rays in tissue

ϕ = incidence angle of primary X-ray beam on tissue surface

By definition, 1 mrad is equal to an energy absorption of 0.1 ergs per gram by any material, and since 1 kev is equal to 1.602×10^{-9} ergs, the radiation absorbed dose rate, D , is:

$$D = E_1 I_1 (\mu_{m-abs})_1^T \left(\frac{1.6 \times 10^{-9}}{0.1} \right) \sin \phi \text{ (mrads/sec)}. \quad (2-28)$$

Solving Equation 2-28 for the ratio $\frac{I_1}{D}$, we obtain:

$$\frac{I_1}{D} = \frac{6.25 \times 10^7}{E_1 (\mu_{m-abs})_1^T \sin \phi} \quad (\text{photons/cm}^2/\text{mrad}) \quad (2-29)$$

Since I_K^Z in Equation 2-15 is a linear function of I_1 , we can solve this equation for the ratio I_K^Z/I_1 and obtain the tracer element K-series fluorescent X-ray intensity at the detector per unit surface dose rate I_K^Z/D , by combining I_K^Z/I_1 with Equation 2-29.

$$\frac{I_K^Z}{D} = \frac{I_K^Z}{I_1} \cdot \frac{I_1}{D} \quad (\text{photons/cm}^2/\text{mrad}) \quad (2-30)$$

2.1.4 Detector Collimation

Equations 2-15 and 2-23 indicate that primary X-ray beam scattering and tracer element fluorescent X-ray production in the tissue surrounding the organ will produce relatively high X-ray intensities at the detector. This background radiation would significantly reduce the sensitivity of the detector to tracer element concentration changes in the organ or defect of interest.

A focused collimator of the type used for conventional radiosotope scanning could be added to the detector to overcome this limitation. This collimator, in conjunction with the primary X-ray beam, would define the region of the biological system being examined. Some examples of how this might be accomplished are presented in Figures 2-3, 2-4, and 2-5.

With the geometry illustrated in Figure 2-3, the horizontal resolution is determined by the design of the detector collimator, and the vertical resolution is determined by the diameter of the primary radiation beam and the angle θ . Equation 2-15 for I_K^Z does not apply directly in this case since the area associated with the incremental

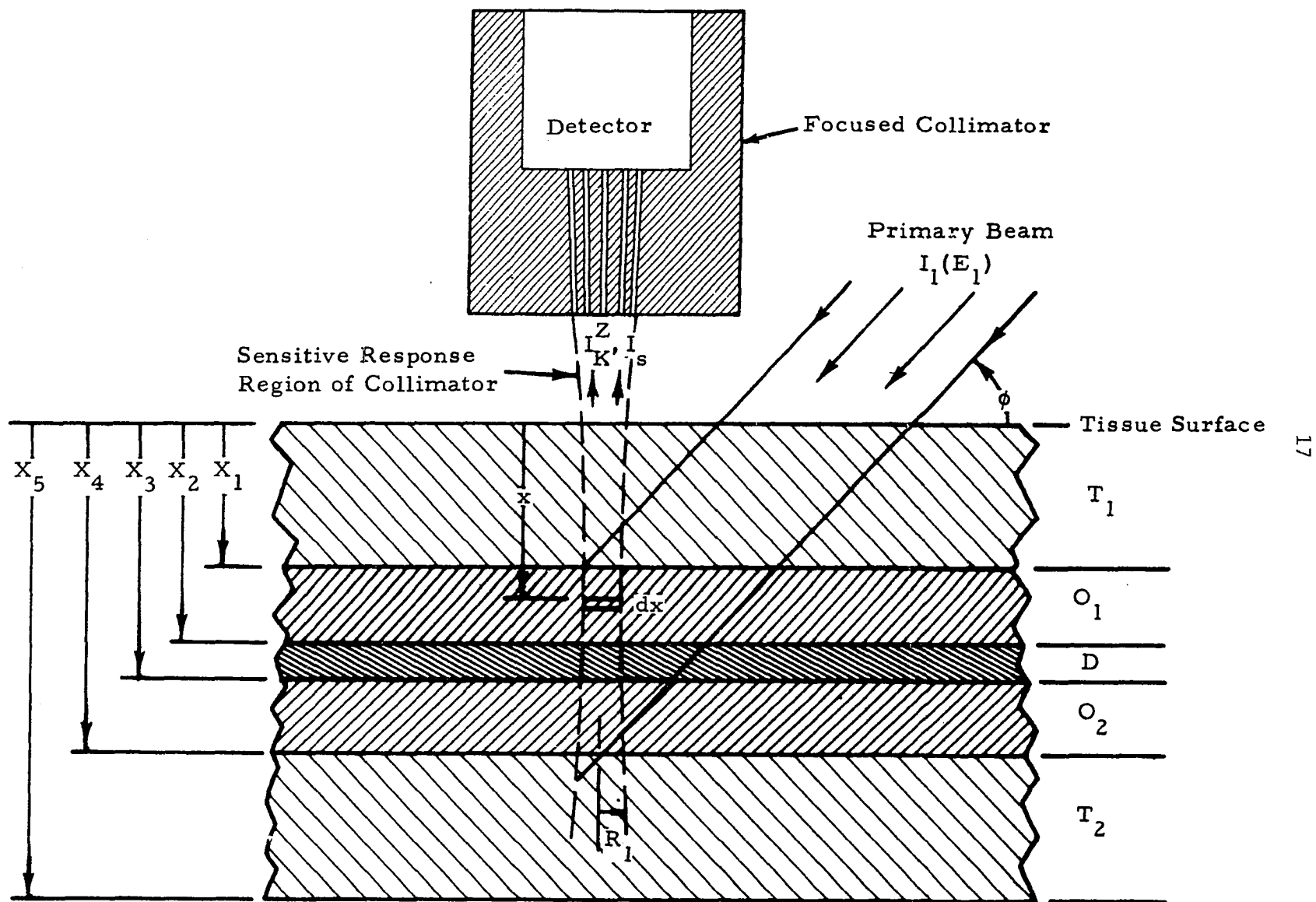


Figure 2-3 System with Horizontal Resolution Determined by Detector Collimator

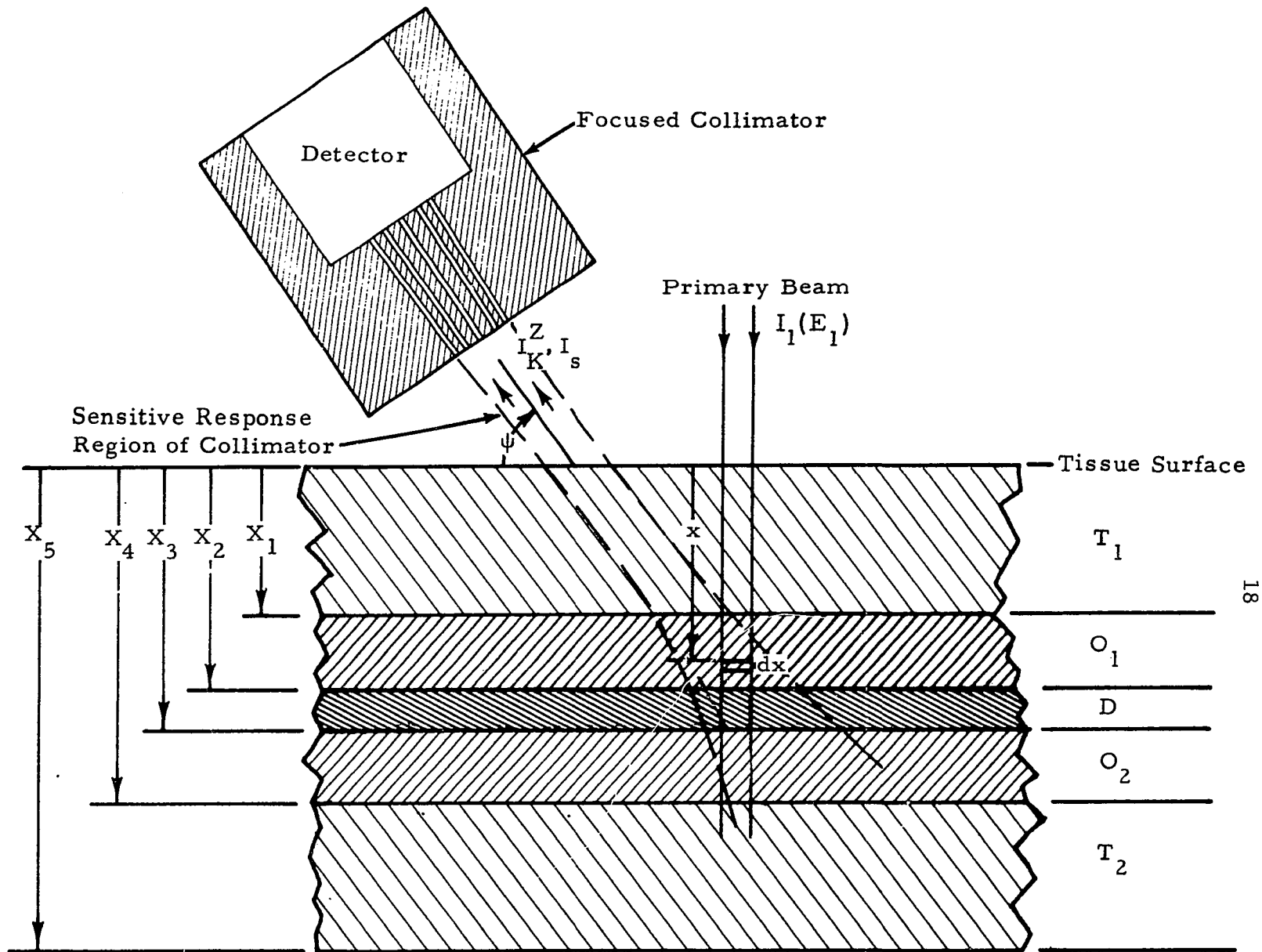


Figure 2-4 System with Horizontal Resolution Determined by Primary Radiation Beam

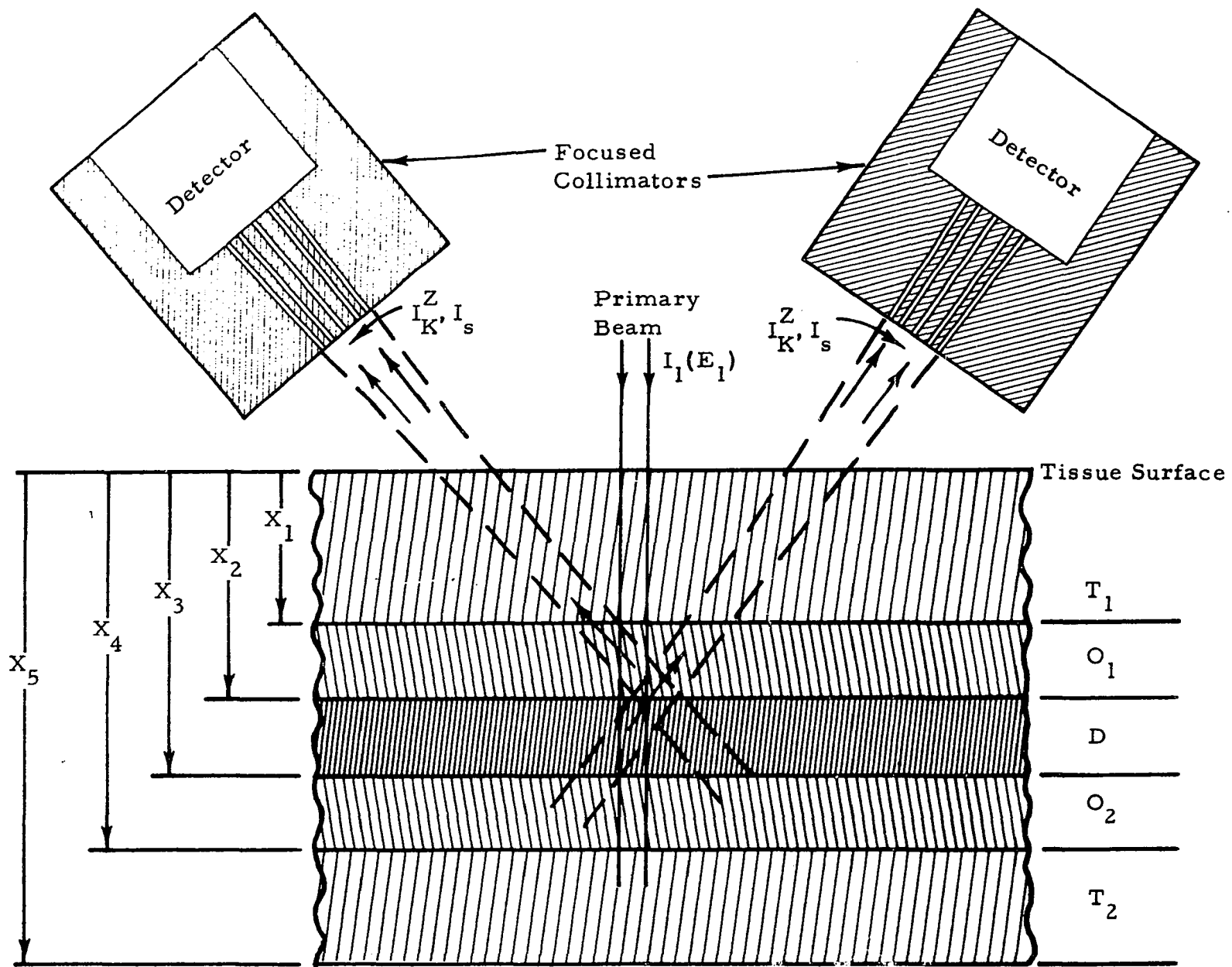


Figure 2-5 Configuration for Simultaneously Determining Concentration Distributions at Several Depths

thickness dx at x is determined by the resolution radius of the collimator, R_1 , which is independent of θ . Under these conditions the equation for I_K^Z is:

$$I_K^Z = B_1 e^{-\alpha^T X_1} \left\{ \frac{\tau_1^{Z,O}}{\alpha^O} \left(1 - e^{-\alpha^O(X_2-X_1)} + e^{-\alpha^O(X_2-X_1) - \alpha^D(X_3-X_2)} \left[1 - e^{-\alpha^O(X_4-X_3)} \right] \right) + \frac{\tau_1^{Z,D}}{\alpha^D} e^{-\alpha^O(X_2-X_1)} \left[1 - e^{-\alpha^D(X_3-X_2)} \right] \right\} \quad (\text{photons/cm}^2 \text{ sec}) \quad (2-31)$$

where the fluorescent X-ray contribution from the tissue surrounding the organ has been neglected and:

$$B_1 = \frac{I_1(\pi R_1^2) \omega_K^Z}{4\pi R^2 \sin \phi} \cdot \frac{r_{K-1}^Z}{r_K^Z}$$

Similarly, the single Compton scattered radiation intensity at the detector for the geometry illustrated in Figure 2-3 can be determined by noting that the resolution radius of the collimator defines the scattering volume $\pi R_1^2 dx$, and by changing the limits of integration in Equation 2-22 to $x = X_1$ and $x = X_4$. With these substitutions, the expression for I_S becomes:

$$I_S = L_1 \frac{\sigma_1^T e^{-\beta^T X_1}}{\beta^T} \left[1 - e^{-\beta^T(X_4-X_1)} \right] \quad (\text{photons/cm}^2 \text{-sec}) \quad (2-32)$$

where the scattered radiation contribution from the tissue surrounding the organ has been neglected and:

$$L_1 = \frac{I_1(\pi R_1^2)}{4\pi R^2 \sin \phi} \left[\frac{3(1 + \cos^2 \theta)}{16\pi} \right]$$

For the configuration shown in Figure 2-4, the horizontal resolution is determined by the diameter of the primary radiation beam, and the vertical resolution is determined by the design of the detector collimator and the angle ψ . Since the assumptions used in deriving Equation 2-15 apply in this case, I_K^Z can be obtained by simply neglecting the contribution to I_K^Z from the tissue surrounding the organ.

$$I_K^Z = B e^{-\alpha^T X_1} \left\{ \frac{\tau_1^{Z,O}}{\alpha^O} \left(1 - e^{-\alpha^O(X_2-X_1)} + e^{-\alpha^O(X_2-X_1) - \alpha^D(X_3-X_2)} \left[1 - e^{-\alpha^O(X_4-X_3)} \right] \right) + \frac{\tau_1^{Z,D}}{\alpha^D} e^{-\alpha^O(X_2-X_1)} \left[1 - e^{-\alpha^D(X_3-X_2)} \right] \right\} \text{ (photons/cm}^2\text{-sec)} \quad (2-33)$$

The single Compton scattered radiation intensity at the detector can also be determined from Equation 2-22 by changing the limits of integration to $x = X_1$ and $x = X_4$.

$$I_S = L \frac{\sigma_1^T e^{-\beta^T X_1}}{\beta^T} \left[1 - e^{-\beta^T(X_4-X_1)} \right] \text{ (photons/cm}^2\text{-sec)} \quad (2-34)$$

The two detector-collimator assemblies shown in Figure 2-5 illustrate one method by which tracer element concentration distributions at several depths could be obtained simultaneously.

Although the source-detector configurations in Figures 2-3, 2-4, and 2-5 are not optimum, they are relatively easy to establish using commercially available equipment, and they could be quite useful for some types of organ scanning and dynamic function studies. In practice, a primary radiation source could simply be attached externally to the detector-collimator assembly of a rectilinear scanner. However, some modifications of the data processing electronics would be required for background suppression. An X-ray machine or a radioisotope could be used for the primary radiation source.

2.2 NARROW BEAM PRIMARY SOURCE - WIDE BEAM DETECTOR GEOMETRY

As indicated by Equations 2-16, 2-30, and 2-33, the use of a small area fluorescent X-ray detector at a large distance from the biological system will result in a much higher radiation dose to the biological system, and a significantly longer data collection time than would be obtained by using a large area fluorescent X-ray detector near the surface of the biological system. An excitation source-fluorescent X-ray detector configuration of this type is illustrated in Figure 2-6.

The collimator is a depth-focusing type, such as the one designed by Glass (Ref. 5), which has been modified to contain the primary radiation source along the central axis. Adequate shielding around the source would be used to exclude direct primary radiation from the detector. This geometry permits the use of a large area fluorescent X-ray detector located at a minimum distance from the biological system while retaining the depth-focusing characteristics of the systems illustrated in the previous section.

The maximum response volume defined by the detector collimator aperture and primary radiation beam is indicated in Figure 2-6 by a dotted line. For calculation purposes, it will be assumed that only radiation emitted or scattered in this volume can reach the detector, and that the concentration of tracer element Z in this volume is uniform. It will also be assumed that the depth-focusing collimator has an open area to total area ratio of p.

If we let E_1 , I_1 , and A_1 represent the primary radiation beam energy, intensity, and cross sectional area respectively and assume that the primary beam is well collimated, the tracer element K-series fluorescent X-ray source term in dx at x is:

$$(dN_1^{Z,0}(X))_{K,f} = I_1 A_1 \tau \cdot \frac{Z,0}{1} \omega \frac{Z}{K} \cdot \frac{r_K^{Z-1}}{r_K^Z} \cdot e^{-\mu_1^T X_1 - \mu_1^O (x - X_1)} dx (\text{photons/sec}) \quad (2-35)$$

where $e^{-\mu_1^T X_1}$ is the attenuation of the primary radiation beam in an overburden tissue thickness of X_1 and $e^{-\mu_1^O (x - X_1)}$ is the attenuation of the primary radiation beam in the overburden organ material.

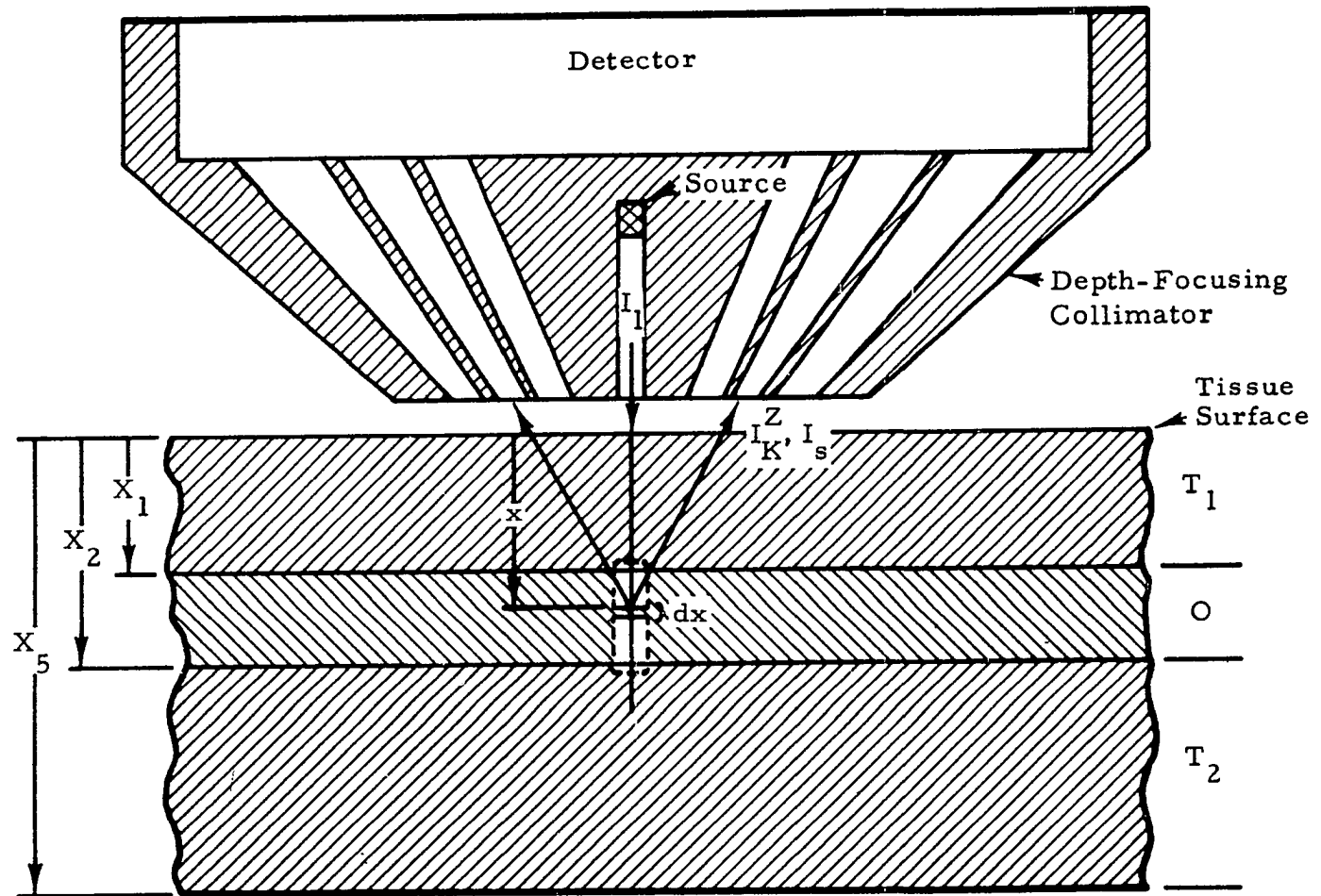


Figure 2-6 Narrow Beam Source-Wide Beam Detector Geometry

Referring to Figure 2-7 the flux of tracer element K-series fluorescent X-rays through the open area on the front surface of the collimator, dF_K^Z , is given in terms of the source in dx at depth x as follows:

$$dF_K^Z(x) = (dN_1^{Z,O(x)})_{K,f} \cdot P \cdot \int_{R_2}^{R_3} \frac{2\pi r}{4\pi(r^2+x^2)} e^{-\mu_K^T \sqrt{r^2+x^2}} dr \quad (2-36)$$

where it has been assumed that $\mu_K^O \approx \mu_K^T$.

The integration will first be completed over r from $r = R_2$ to $r = R_3$ and the total flux of tracer element K-series fluorescent X-rays through the collimator open area, F_K^Z , will be obtained by integrating $dF_K^Z(x)$ over x from $x = X_1$ to $x = X_2$.

If we let $\mu_K^T \sqrt{r^2+x^2} = y$, Equation 2-36 becomes:

$$dF_K^Z(x) = \frac{(dN_1^{Z,O(x)})_{K,f} \cdot P}{2} \cdot \int_{\mu_K^T x \sec \psi_1}^{\mu_K^T x \sec \psi_2} \frac{e^{-y}}{y} dy \quad (2-37)$$

or:

$$dF_K^Z(x) = \frac{(dN_1^{Z,O(x)})_{K,f} \cdot P}{2} \cdot \left\{ E_1(\mu_K^T x \sec \psi_1) - E_1(\mu_K^T x \sec \psi_2) \right\} (\text{photons/sec}) \quad (2-38)$$

where $E_1(\mu_K^T x \sec \psi_1)$ and $E_1(\mu_K^T x \sec \psi_2)$ are exponential integrals defined by the equation

$$E_1(a) = \int_a^{\infty} \frac{e^{-y}}{y} dy$$

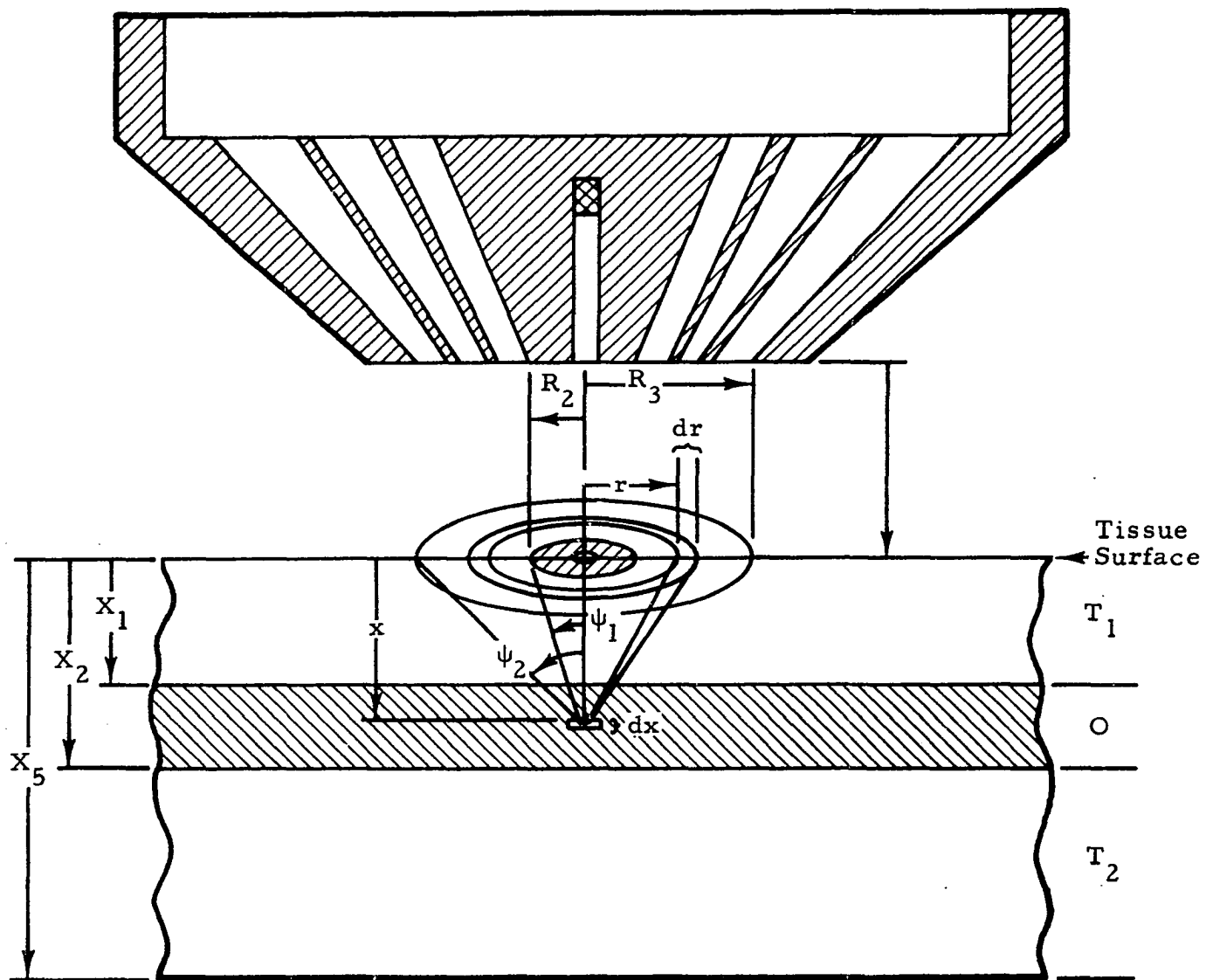


Figure 2-7 Notation for Wide Beam Detector Geometry Calculations

Since ψ_1 and ψ_2 are only slightly dependent on x over the range $X_1 \leq x \leq X_2$, the total flux of tracer element K-series fluorescent X-rays through the collimator open area can be obtained by substituting Equation 2-35 for $(dN_1^{Z,O}(x))_{K,f}$ in Equation 2-38 and integrating over x from $x = X_1$ to $x = X_2$.

$$F_K^Z = M \left[\int_{X_1}^{X_2} e^{-\mu_1^O x} E_1(ax) dx - \int_{X_1}^{X_2} e^{-\mu_1^O x} E_1(bx) dx \right] \text{ (photons/sec)} \quad (2-39)$$

$$\text{where } M = I_1 A_1 \tau_1^{Z,O} \omega_K^Z \cdot \frac{r_I^{Z-1}}{r_K^Z} \cdot \frac{p}{2} \cdot e^{-(\mu_1^T - \mu_1^O) X_1}$$

$$a = \mu_K^T \sec \psi_1$$

$$b = \mu_K^T \sec \psi_2$$

By changing the limits of integration, Equation 2-39 can be written as follows:

$$F_K^Z = M \left[\int_0^{X_2} e^{-\mu_1^O x} E_1(ax) dx - \int_0^{X_1} e^{-\mu_1^O x} E_1(ax) dx - \int_0^{X_2} e^{-\mu_1^O x} E_1(bx) dx + \int_0^{X_1} e^{-\mu_1^O x} E_1(bx) dx \right] \text{ (photons/sec)} \quad (2-40)$$

Closed form solutions cannot be obtained for these integrals. However, they can be expressed in terms of exponential integrals for which values have been tabulated (Ref. 6.) Polynomial equations have also been reported (Ref. 7) for calculating approximate values of exponential integrals.

Using the relationship:

$$\int_0^c e^{-pt} E_1(at) dt = \frac{1}{p} \left\{ \ln \left(\frac{p}{a} + 1 \right) - e^{-pc} E_1(ac) + E_1[(a+p)c] \right\}$$

the solution of Equation 2-40 is:

$$F_K^Z = \frac{M}{\mu_1} \left\{ e^{-\mu_1^O X_2} [E_1(bX_2) - E_1(aX_2)] + E_1[(a+\mu_1^O)X_2] - E_1[(b+\mu_1^O)X_2] \right. \\ \left. + e^{-\mu_1^O X_1} [E_1(aX_1) - E_1(bX_1)] + E_1[(b+\mu_1^O)X_1] - E_1[(a+\mu_1^O)X_1] \right\} \left(\frac{\text{photons}}{\text{sec}} \right) \quad (2-41)$$

The tracer element K-series fluorescent X-ray count rate from the detector, C_K^Z , can now be determined by multiplying F_K^Z by the detector efficiency for these X-rays, ϵ_K^Z .

$$C_K^Z = F_K^Z \epsilon_K^Z \quad (\text{counts/sec}) \quad (2-42)$$

2.3 X-RAY PHYSICS

In this section, measured values of the X-ray parameters that apply to this problem are summarized and approximate equations are developed that can be used for calculation purposes. The quantities of interest include the K-series fluorescence yield of element Z, the K-absorption jump ratio of element Z, and the absorption, attenuation, and scattering coefficients of the constituent elements of the biological system.

2.3.1 K-Fluorescence Yield

Experimental values of the K fluorescence yield, ω_K^Z , have been compiled for a number of elements from thirty-three references by Broyles, Thomas, and Haynes (Ref. 8) and more recent measurements have been reported by Heintze (Ref. 9) and by Davidson and Wyckoff (Ref. 10). Although these data show some rather wide variations in the measured values of ω_K^Z for a single element, the general relationship between ω_K^Z and atomic number can be established by taking unweighted average values of all the measurements reported. These average values and the number of measurements associated with each value are presented in Table 2-1. As suggested by Burhop (Ref. 11), the measurements for elements with $Z > 42$ by Berkey (Ref. 8,12) have been omitted since they have not been confirmed by other workers and appear unlikely to be correct on theoretical grounds.

Also presented in Table 2-1 are values of ω_K^Z calculated from Pincherle's (Ref. 13) theoretical equation:

$$\omega_K^Z = [1 + aZ^{-4}]^{-1} \quad (2-43)$$

using the value of a suggested by Blokhin (Ref. 1).

The results listed in Table 2-1 are illustrated graphically in Figure 2-8. It is apparent from this graph that the experimental data are in good agreement with Equation 2-43 for elements with $Z \geq 30$ which would be most useful for in vivo studies.

2.3.2 K-Absorption Jump Ratio

The K-absorption jump ratio of element Z , r_K^Z , is defined as the ratio of the values of the mass absorption coefficient of element Z , $(\tau_m)^Z$, on the high and low energy sides of the K-absorption edge. Average values of r_K^Z compiled by Blokhin (Ref. 1) from the data of various authors are given in Table 2-2.

TABLE 2-1

MEASURED AND CALCULATED VALUES
OF K-FLUORESCENCE YIELD Z/K

<u>Atomic Number Z</u>	<u>Element</u>	<u>Number of Measurements</u>	<u>Experimental Z ω_K</u>	<u>Theoretical Z ω_K</u>
6	C	1	0.0009	0.00120
7	N	1	0.0015	0.00223
8	O	2	0.0421	0.00380
9	F	0		0.00607
10	Ne	3	0.0364	0.00922
11	Na	0		0.0134
12	Mg	2	0.016	0.0189
13	Al	1	0.027	0.0259
14	Si	2	0.041	0.0345
15	P	0		0.0450
16	S	3	0.102	0.575
17	Cl	2	0.074	0.721
18	Ar	6	0.101	0.0890
19	K	0		0.108
20	Ca	2	0.179	0.130
21	Sc	0		0.153
22	Ti	1	0.160	0.0179
23	V	1	0.190	0.207
24	Cr	4	0.262	0.236
25	Mn	1	0.220	0.267
26	Fe	7	0.323	0.298
27	Co	1	0.380	0.331
28	Ni	9	0.404	0.364
29	Cu	8	0.454	0.397
30	Zn	8	0.496	0.430
31	Ga	0		0.462
32	Ge	0		0.494

TABLE 2-1 (Continued)

<u>Atomic Number Z</u>	<u>Element</u>	<u>Number of Measurements</u>	<u>Experimental Z ω_K</u>	<u>Theoretical Z ω_K</u>
33	As	1	0.530	0.525
34	Se	7	0.581	0.554
35	Br	4	0.594	0.583
36	Kr	3	0.570	0.610
37	Rb	0		0.635
38	Sr	2	0.682	0.660
39	Y	0		0.683
40	Zr	1	0.690	0.704
41	Nb	0		0.724
42	Mo	7	0.787	0.743
43	Tc	0		0.761
44	Ru	0		0.777
45	Rh	2	0.786	0.792
46	Pd	1	0.835	0.806
47	Ag	6	0.847	0.819
48	Cd	3	0.822	0.832
49	In	0		0.843
50	Sn	3	0.830	0.853
51	Sb	1	0.862	0.863
52	Te	1	0.872	0.872
53	I	1	0.880	0.880
54	Xe	3	0.763	0.888
55	Cs	1	0.890	0.895
56	Ba	2	0.885	0.901
57	La	0		0.908
58	Ce	0		0.913
59	Pr	1	0.880	0.919
60	Nd	0		0.923
61	Pm	0		0.928
62	Sm	0		0.932

TABLE 2-1 (Continued)

<u>Atomic Number Z</u>	<u>Element</u>	<u>Number of Measurements</u>	<u>Experimental Z ω_K</u>	<u>Theoretical Z ω_K</u>
63	Eu	0		0.936
64	Gd	0		0.940
65	Tb	0		0.943
66	Dy	0		0.946
67	Ho	0		0.949
68	Er	0		0.952
69	Tm	0		0.955
70	Yb	0		0.957
71	Lu	0		0.959
72	Hf	0		0.962
73	Ta	0		0.964
74	W	0		0.965
75	Re	0		0.967
76	Os	0		0.969
77	Ir	0		0.970
78	Pt	1	0.942	0.972
79	Au	0		0.973
80	Hg	1	0.946	0.974
81	Tl	0		0.976
82	Pb	1	0.890	0.977
83	Bi	2	0.955	0.978
84	Po	1	0.894	0.979

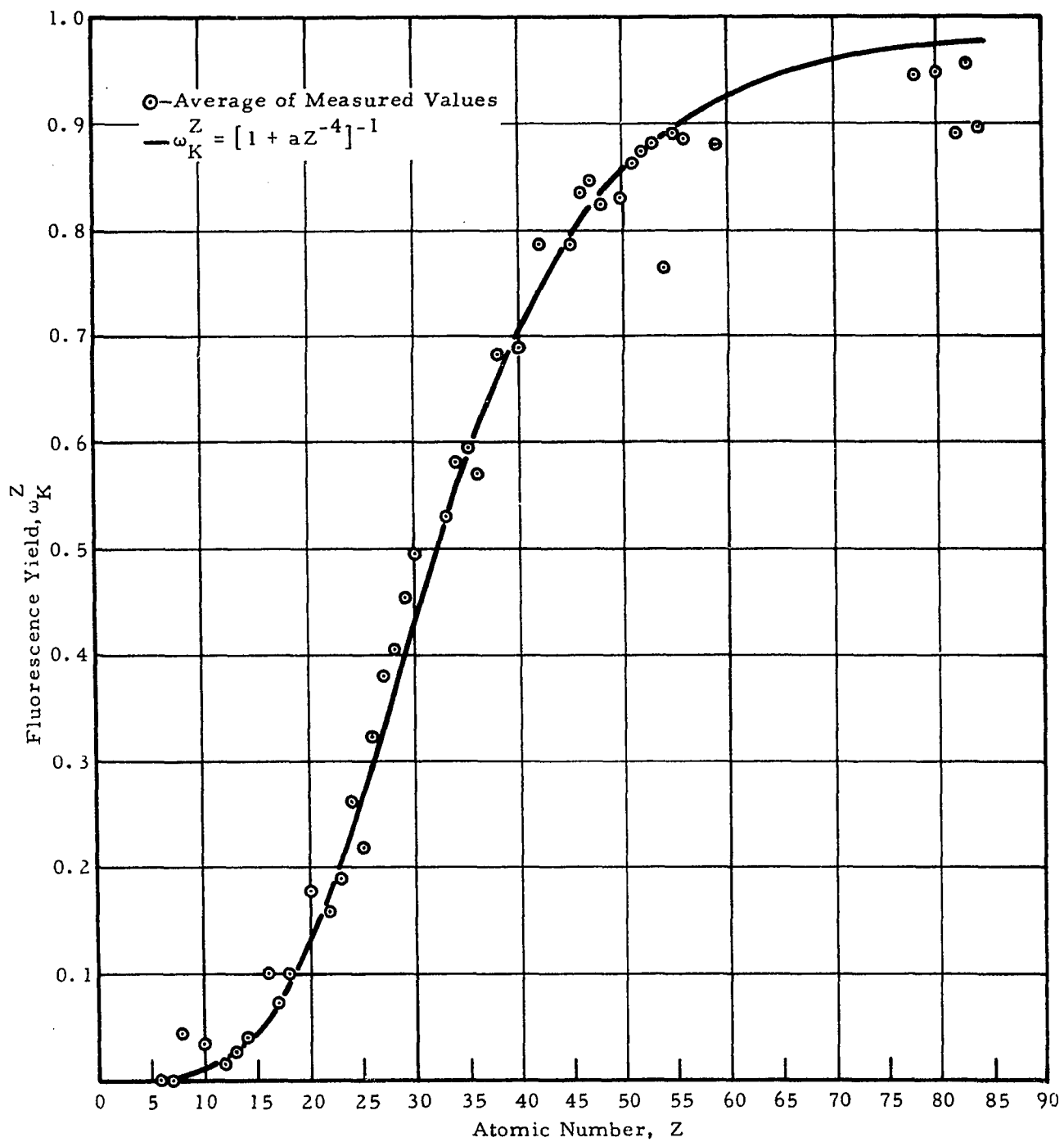


Figure 2-8 Comparison of Observed and Calculated Values of Fluorescent Yield

TABLE 2-2

MEASURED AND CALCULATED VALUES
OF K-ABSORPTION JUMP RATIO r_K^Z

Atomic Number Z	Element	Experimental r_K^Z	$r_K^Z = \frac{E_{K-abs}}{E_{L_1-abs}}$	$r_K^Z = \frac{5.88}{(1 - \frac{6.2}{Z})^2} - 1.2$
13	Al	12.6	17.9	
14	Si		15.6	
15	P		14.0	15.9
16	X	11.0	12.8	14.5
17	Cl	10.4	11.83	13.4
18	Ar	10.0	11.2	12.5
19	K		10.6	11.8
20	Ca		10.1	11.2
21	Sc		9.73	10.6
22	Ti		9.37	10.2
23	V		9.04	9.82
24	Cr		8.82	9.49
25	Mn		8.58	9.20
26	Fe	8.8	8.38	8.94
27	Co		8.30	8.71
28	Ni	8.3	8.21	8.50
29	Cu	8.3	8.16	8.31
30	Zn	7.9	8.05	8.14
31	Ga		7.98	7.99
32	Ge	6.3	7.82	7.85
33	As		7.76	7.72
34	Se		7.66	7.60
35	Br	7.3	7.51	7.48
36	Kr		7.42	7.38
37	Rb		7.35	7.29
38	Sr	7.4	7.25	7.20

TABLE 2-2 (Continued)

<u>Number Z</u>	<u>Element</u>	<u>Experimental $\frac{Z}{r_K}$</u>	<u>$r_K^Z = \frac{E_{K-abs}}{E_{L_1-abs}}$</u>	<u>$r_K^Z = \frac{5.88}{(1 - \frac{6.2}{Z})^2} - 1.2$</u>
39	Y		7.19	7.11
40	Zr		7.07	7.04
41	Nb		7.02	6.96
42	Mo	7.5	6.94	6.89
43	Tc		6.89	6.83
44	Ru		6.83	6.77
45	Rh		6.79	6.71
46	Pd	6.8	6.73	6.66
47	Ag	7.0	6.70	6.60
48	Cd		6.65	6.55
49	In		6.59	6.51
50	Sn	6.6	6.54	6.46
51	Sb		6.49	6.42
52	Te		6.44	6.38
53	I	5.5	6.39	6.34
54	Xe		6.34	6.30
55	Cs		6.29	6.27
56	Ba	5.2	6.24	6.24
57	La		6.20	6.20
58	Ce		6.17	6.17
59	Pr		6.13	6.14
60	Nd		6.10	6.11
61	Pm		6.07	6.09
62	Sm		6.04	6.06
63	Eu		6.01	6.03
64	Gd		5.98	6.01
65	Tb		5.96	5.99
66	Dy		5.92	5.96

TABLE 2-2 (Continued)

Atomic Number Z	Element	Experimental r_K^Z	$r_K^Z = \frac{E_{K-abs}}{E_{L_1-abs}}$	$r_K^Z = \frac{5.88}{(1 - \frac{6.2}{Z})^2} - 1.2$
67	Ho		5.91	5.94
68	Er		5.88	5.92
69	Tm		5.85	5.90
70	Yb		5.85	5.88
71	Lu		5.83	5.86
72	Hf		5.80	5.84
73	Ta	4.2	5.77	5.82
74	W	5.65	5.75	5.81
75	Re		5.72	5.79
76	Os		5.70	5.77
77	Ir		5.67	5.76
78	Pt	6.0	5.65	5.74
79	Au	5.65	5.62	5.72
80	Hg		5.60	5.71
81	Tl		5.57	5.70
82	Pb	5.4	5.55	5.68
83	Bi		5.52	5.67
84	Po		5.50	5.66
85	At		5.47	5.64
86	Rn		5.45	5.63
87	Fr		5.43	5.62
88	Ra		5.40	5.61
89	Ac		5.38	5.59
90	Th		5.36	5.58
91	Pa		5.34	5.57
92	U	2.9	5.31	5.56
93	Np		5.29	5.55
94	Pu		5.27	5.54

From an analysis of experimental data, it has been suggested (Ref. 14) that the K-absorption jump ratio can be found from the following formula:

$$r_K^Z = \frac{E_{K-abs}^Z}{E_{L_1-abs}^Z} \quad (2-44)$$

where E_{K-abs}^Z and $E_{L_1-abs}^Z$ are the energies of the K and L_1 absorption edges of element Z.

It would be desirable, for calculation purposes, to have an expression for r_K^Z which depends only on the atomic number of the element Z. However, exact values for the atomic X-ray levels E_{K-abs} and E_{L_1-abs} are difficult to calculate. Several attempts were therefore made to fit a form of Mosely's approximate law for the atomic energy levels to the data obtained from Equation 2-44. They resulted in the expression:

$$r_K^Z = \frac{5.88}{(1 - \frac{6.2}{Z})^2} - 1,2 \quad (2-45)$$

Values of r_K^Z calculated from Equation 2-44 using Blokhin's data for E_{K-abs} and E_{L_1-abs} and values of r_K^Z obtained from Equation 2-45 are presented in Table 2-2.

The measured and calculated values of r_K^Z listed in Table 2-2 are presented graphically in Figure 2-9. It is apparent from this graph that Equation 2-45 is in good agreement with the experimental data for elements with $Z \geq 30$ which are of primary concern in this application.

2.3.3 Absorption, Attenuation, and Scattering Coefficients

It will be assumed in subsequent sections of this paper that each region of the biological system is composed of a mixture of water, which

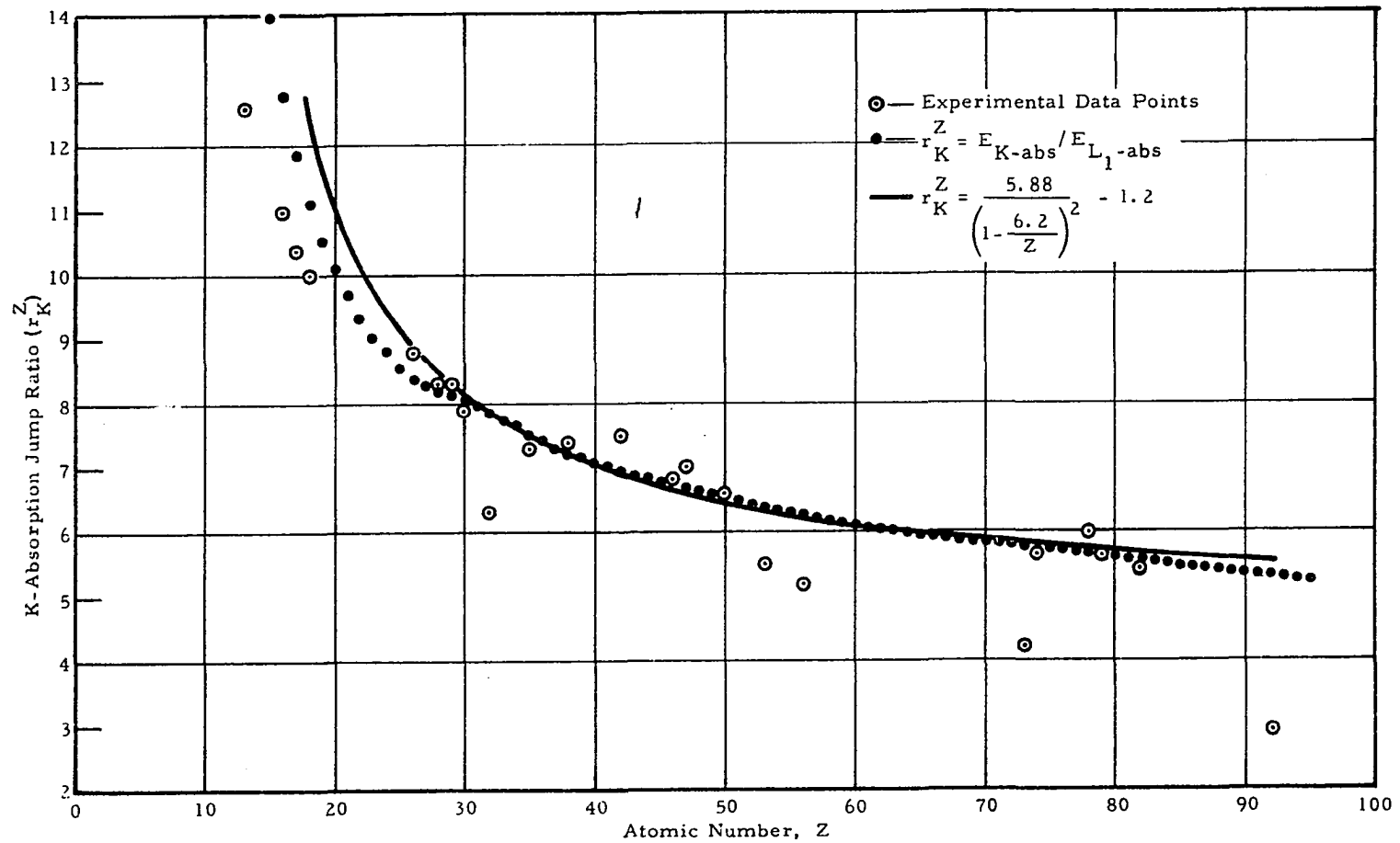


Figure 2-9 Comparison of Observed and Calculated Values of K-Absorption Jump Ratio

is a "tissue equivalent material," with a concentration by weight of C_W , and tracer element Z with a concentration by weight of C_Z . Since, by definition, ($C_W = 1 - C_Z$), the linear absorption, attenuation, and scattering coefficients in any region i of the biological system can be expressed in terms of the corresponding mass absorption, attenuation, and scattering coefficients as follows:

$$\tau_1^{Z,i} = (\tau_m)_1^Z \rho^i C_Z^i \quad (2-46)$$

$$\mu_1^i = (\mu_m)_1^Z \rho^i C_Z^i + (\mu_m)_1^W \rho^i (1 - C_Z^i) \quad (2-47)$$

$$\mu_K^i = (\mu_m)_K^Z \rho^i C_Z^i + (\mu_m)_K^W \rho^i (1 - C_Z^i) \quad (2-48)$$

$$\sigma_1^i = (\sigma_m)_1^Z \rho^i C_Z^i + (\sigma_m)_1^W \rho^i (1 - C_Z^i) \approx (\sigma_m)_1^W \quad (2-49)$$

where

$\tau_1^{Z,i}$ = linear absorption coefficient of primary radiation in element Z in region i

μ_1^i = linear attenuation coefficient of primary radiation in region i

μ_K^i = linear attenuation coefficient of element Z K X-rays in region i

σ_1^i = linear scattering coefficient of primary radiation in region i \approx mass scattering coefficient of primary radiation in water = $(\sigma_m)_1^W$

C_Z^i = concentration by weight of element Z in region i

$$\rho^i = \text{density of region } i = \frac{\rho^Z \rho^W}{\rho^Z + (\rho^W - \rho^Z) C_Z^i}$$

$$\rho^Z = \text{density of tracer element } Z$$

$$\rho^W = \text{density of water} = 1 \text{ g/cm}^3$$

$$(\tau_m)_1^Z = \text{mass absorption coefficient of primary radiation in element } Z$$

$$(\mu_m)_1^Z = \text{mass attenuation coefficient of primary radiation in element } Z$$

$$(\mu_m)_1^W = \text{mass attenuation coefficient of primary radiation in water}$$

$$(\mu_m)_K^Z = \text{mass attenuation coefficient of element } Z \text{ K X-rays in element } Z$$

$$(\mu_m)_K^W = \text{mass attenuation coefficient of element } Z \text{ K X-rays in water}$$

This list indicates that values of the mass absorption and attenuation coefficients of tracer element Z and the mass attenuation and scattering coefficients of water must be obtained to determine values of $\tau_1^{Z,i}$, μ_1^i , μ_K^i , and σ_1^i . Also, from Equation 2-29, the mass energy absorption coefficient of water $(\mu_{m-abs})^W$, is needed for radiation dose and dose rate calculations.

2.3.3.1 Mass Absorption and Attenuation Coefficients for High-Z Elements

A tabulation of narrow-beam absorption and attenuation coefficients of X- and gamma rays from 0.01 to 100 Mev for 29 materials has been prepared by Grodstein (Ref. 15) and similar data have been presented by other authors (Ref. 16, 17, 18). These data were derived primarily from theoretical calculations with experimental results being used as a check and to provide empirical corrections.

Although theoretical methods for calculating mass absorption and attenuation coefficients are well established, it is very difficult to calculate accurate values of these parameters for all elements over a wide energy range. A considerable effort was therefore devoted to the development of approximate equations that could be applied to elements with atomic numbers greater than 30 for energies below 150 keV for this reason. The selection of these atomic number and energy limits will be discussed in subsequent sections of this paper.

Bloclin (Ref. 1) has suggested that a semiempirical equation of the form:

$$(\tau_m)_E^Z = \frac{G Z^{2.65}}{E^{2.78}} \text{ (cm}^2/\text{g)} \quad (2-50)$$

where G is a constant, can be used to determine the mass absorption coefficient of element Z under the following conditions:

$$0.4 < \frac{Z}{E} < 8.1$$

$$E_K < E < 125 \text{ keV}$$

Normalizing this equation to Grodstein's values for $(\tau_m)_E^Z$ on the high energy side of the K-absorption edge, it was noted that the calculated values of $(\tau_m)_E^Z$ for $G = 16.5$ agree with Grodstein's results within 8 per cent and in most cases the error is less than 5 per cent if $E_K < E < 150$ keV. Since this error is less than the estimated uncertainty in these values (Ref. 15), the use of Equation 2-50 is justified in this application.

Since the total mass absorption coefficient is the sum of the partial mass absorption coefficients, the mass absorption coefficient of element Z for K-series X-rays of element Z , $(\tau_m)_K^Z$ can be obtained by dividing Equation 2-50 by the K-absorption jump ratio r_K^Z :

$$(\tau_m)_K^Z = \frac{16.5 Z^{2.65}}{r_K^Z E_K^{2.78}} \text{ (cm}^2/\text{g)} \quad (2-51)$$

where r_K^Z is given by Equation 2-45.

To determine the total mass attenuation coefficient of element Z,

$$(\mu_m)_E^Z = (\tau_m)_E^Z + (\sigma_m)_E^Z \quad (2-52)$$

an expression for the mass scattering coefficient, $(\sigma_m)_E^Z$, as a function of atomic number and energy is required. The classical expression for $(\sigma_m)_E^Z$ is:

$$(\sigma_m)_E^Z = \frac{K^1 Z}{A} \approx \frac{K^1}{1.4Z^{0.13}} \text{ (cm}^2/\text{g)} \quad (2-53)$$

where K^1 is a constant and the empirical relationship $A \approx 1.4 Z^{1.13}$ has been substituted for atomic weight. However, Equation 2-53 is only applicable to the lighter elements for energies less than about 50 keV. When these conditions do not obtain, more complicated equations which include energy-dependent terms must be used.

An examination of tabulated values of $(\sigma_m)_E^Z$ for energies within the range $E_K < E < 150$ keV and for elements with atomic numbers greater than 30, indicates that good agreement with experimental data will result if Equation 2-53 is modified to include an energy dependence as follows:

$$(\sigma_m)_E^Z = \frac{0.387}{(EZ)^{0.13}} \text{ (cm}^2/\text{g)} \quad (2-54)$$

where Grodstein's values of $(\sigma_m)_E^Z$ on the high energy side of the K absorption edge have been used for normalization.

Substituting Equations 2-50 and 2-54 for $(\tau_m)_E^Z$ and $(\sigma_m)_E^Z$ in Equation 2-52 we obtain:

$$(\mu_m)_E^Z = \frac{16.5 Z^{2.65}}{E^{2.78}} + \frac{0.387}{(EZ)^{0.13}} \text{ (cm}^2/\text{g)} \quad (2-55)$$

Similarly, from Equations 2-51 and 2-54, an approximate equation for $(\mu_m)_K^Z$ is:

$$(\mu_m)_K^Z = \frac{16.5 Z^{2.65}}{r_K^Z E^{2.78}} + \frac{0.387}{(EZ)^{0.13}} \text{ (cm}^2/\text{g)} \quad (2-56)$$

Calculated values of $(\tau_m)_E^Z$ and $(\mu_m)_E^Z$ from Equations 2-50 and 2-55 for iodine are presented in Table 2-3 along with the corresponding values reported by Grodstein. Additional values of mass absorption and attenuation coefficients for elements with atomic numbers in the range $42 \leq Z \leq 82$ can be calculated from these approximate equations.

2.3.3.2 Mass Scattering and Attenuation Coefficients for Water

It would appear, from Equation 2-55, that the mass absorption and attenuation coefficients for water could be determined from an equation of the form:

$$(\mu_m)_E^W = (\tau_m)_E^W + (\sigma_m)_E^W = \frac{K_1}{E^{2.78}} + \frac{K_2}{E^{0.13}} \text{ (cm}^2/\text{g)}$$

where the constants K_1 and K_2 are obtained from experimental data.

This equation provides fairly good agreement with tabulated values of $(\mu_m)_E^W$ and $(\sigma_m)_E^W$ if $K_1 = 2,110$ and $K_2 = 0.20$. However, for this low

atomic number material, a better description of the experimental data is obtained from the equation:

$$(\mu_m)_E^W = \frac{8,750}{E^{3.25}} + \frac{0.304}{E^{0.13}} \text{ (cm}^2/\text{g)} \quad (2-57)$$

where:

$$\frac{0.304}{E^{0.13}} = (\sigma_m)_E^W \text{ (cm}^2/\text{g)} \quad (2-58)$$

TABLE 2-3

MASS ABSORPTION AND ATTENUATION COEFFICIENTS FOR IODINE (Z=53)

Energy (kev)	Reference 15 Mass Absorption Coefficient (cm ² /g)	Equation (2. 50) Mass Absorption Coefficient (cm ² /g)	Reference 15 Mass Absorption Coefficient (cm ² /g)	Equation (2. 55) Mass Absorption Coefficient (cm ² /g)
34. 0	35. 7	36. 3	35. 8	36. 4
40	21. 3	21. 5	21. 5	21. 5
50	11. 7	11. 6	11. 9	11. 7
60	7. 12	6. 98	7. 26	7. 11
70		4. 54		4. 68
80	3. 21	3. 13	3. 34	3. 27
90		2. 26		2. 39
100	1. 71	1. 69	1. 83	1. 81
110		1. 29		1. 42
120		1. 02		1. 14
130		0. 813		0. 936
140		0. 662		0. 783
150	. 536	0. 546	0. 648	0. 667

Mass attenuation and scattering coefficients for water from Equations 2-57 and 2-58 as well as those reported by Grodstein (Ref. 15) are presented in Table 2-4 for comparison. Again, the error resulting from the use of these approximate equations is less than the estimated uncertainty in these values.

2.3.3.3 Mass Energy Absorption Coefficients for Water

As indicated in Section 2.1.3, the tissue mass energy absorption coefficient $(\mu_{m-abs})_1^T$, in Equation 2-29 can be replaced by the water mass energy absorption coefficient $(\mu_{m-abs})_E^W$ for dosimetry calculations.

It was determined from a graphical analysis of Evans' data (Ref. 19) that the mass energy absorption coefficient of water can be approximated by the equation:

$$(\mu_{m-abs})_E^W = \frac{7650}{E^{3.25}} + 1.45 \times 10^{-3} E^{0.6} \text{ (cm}^2/\text{g)} \quad (2-59)$$

for energies less than 150 kev. Values of $(\mu_{m-abs})_E^W$ obtained from this equation and those reported by Evans for several energies are listed in Table 2-5. These values agree within 7% over the energy range of interest with the largest error occurring at the highest energy.

When Equation 2-59 for $(\mu_{m-abs})_E^W$ is substituted in Equation 2-29 for $(\mu_{m-abs})_1^T$, we obtain an equation for calculating the number of photons per cm^2 required to produce a surface dose of one millirad as a function of incident photon energy.

$$\frac{I_1}{D} = \frac{6.25 \times 10^7}{\left[\frac{7650}{E^{2.25}} + 1.45 \times 10^{-3} E^{1.6} \right] \sin \phi} \text{ (photons/cm}^2\text{/mrad)} \quad (2-60)$$

The quantity I_1/D as a function of E for $\phi = 90^\circ$ is presented graphically in Figure 2-10.

TABLE 2-4

MASS SCATTERING AND ATTENUATION COEFFICIENTS FOR WATER

Energy (kev)	Reference 15 Mass Scattering Coefficient (cm ² /g)	Equation 2-58 Mass Scattering Coefficient (cm ² /g)	Reference 15 Mass Scattering Coefficient (cm ² /g)	Equation 2-57 Mass Scattering Coefficient (cm ² /g)
20	0.207	0.206	0.722	0.723
30	0.200	0.195	0.336	0.334
40	0.193	0.188	0.245	0.243
50	0.187	0.183	0.212	0.209
60	0.183	0.179	0.196	0.193
70		0.175		0.184
80	0.173	0.172	0.178	0.178
90		0.169		0.173
100	0.165	0.167	0.167	0.170
110		0.165		0.167
120		0.163		0.165
130		0.161		0.163
140		0.160		0.161
150	0.148	0.158	0.149	0.159

TABLE 2-5

MASS ENERGY ABSORPTION COEFFICIENTS FOR WATER

Energy (kev)	Reference 19 Mass Energy Absorption Coefficient (cm ² /g)	Equation 2-59 Mass Energy Absorption Coefficient (cm ² /g)
10	4.2	4.31
20	0.48	0.46
30	0.14	0.13
40	0.064	0.061
50	0.038	0.038
60	0.030	0.030
70	0.0265	0.0263
80	0.0250	0.0251
90	0.0250	0.0250
100	0.0255	0.0254
110		0.0261
120		0.0270
130		0.0279
140		0.0289
150	0.028	0.0300

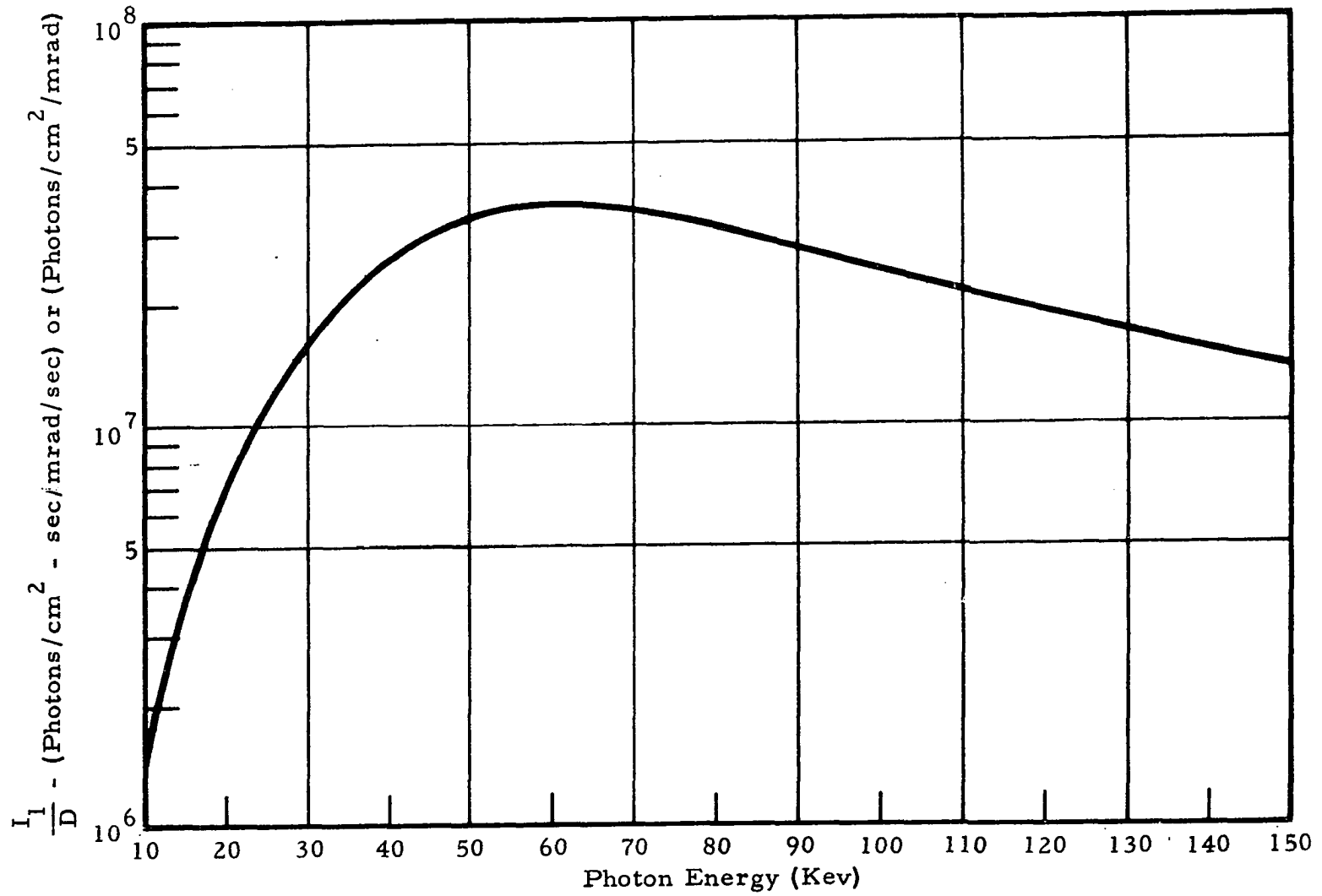


Figure 2-10 Photon Intensity Per Unit Surface Dose Rate as a Function of Photon Energy

2.4 DEPENDENCE OF FLUORESCENT X-RAY INTENSITY ON EXCITATION SOURCE - BIOLOGICAL SYSTEM - AND FLUORESCENT X-RAY DETECTOR PARAMETERS

In this section, the source - biological system - detector geometry illustrated in Figure 2-4 will be used to determine the dependence of K-series fluorescent X-ray intensity on the various parameters associated with the excitation source, the biological system and the fluorescent X-ray detector. It should be noted that this same general dependence will apply to all of the source-detector configurations illustrated in Section 2.1.4 for large angles ϕ and ψ .

Determining the fluorescent X-ray intensity for all possible values of the variable parameters would be an extensive undertaking and would require a detailed knowledge of physiology and biochemistry. For this reason, the parameter values selected for the example calculations in this section illustrate the variation of fluorescent X-ray intensity that will occur under certain conditions, and do not imply that these values can be obtained in a biological system that is functioning normally.

Iodine, in many of the calculations, has been assumed for the tracer element since several gram quantities of this element are administered routinely for radiological diagnostic purposes, and a variety of iodinated compounds have been developed for X-ray visualization of kidney, gall bladder, and gastrointestinal tract, as well as delineation of heart and peripheral blood vessels.

From Equation 2-33 it is apparent that I_K^Z is a rather complicated function of the following:

1. Organ depth
2. Organ thickness
3. Defect depth
4. Defect thickness
5. Primary X-ray beam energy
6. Tracer element atomic number
7. Tracer element concentration.

However, we are primarily interested in the general dependence of tracer element fluorescent X-ray intensity on these parameters, and several simplifying assumptions can be made without loss of generality.

First, it will be assumed that the organ does not contain a defect, in which case Equation 2-33 reduces to:

$$I_K^Z = \frac{B e^{-\alpha^T X_1} \tau_{1,Z,O}}{\alpha^O} \left[1 - e^{-\alpha^O (X_4 - X_1)} \right] \quad (2-61)$$

or:

$$I_K^Z = \frac{I_1 A_1 \omega_K^Z e^{-\alpha^T X_1} \tau_{1,Z,O}}{4\pi R^2 \alpha^O} \cdot \frac{r_K^Z - 1}{r_K^Z} \left[1 - e^{-\alpha^O (X_4 - X_1)} \right] \quad (2-62A)$$

To determine the fluorescent X-ray intensity at the detector per unit surface dose rate, Equations 2-29 and 2-62A can then be combined to give:

$$\frac{I_K^Z}{D} = \frac{(6.25 \times 10^7) A_1 \omega_K^Z}{E_1 (\mu_{m-abs})_1^w 4\pi R^2} \cdot \frac{r_K^Z - 1}{r_K^Z} \cdot \frac{\tau_{1,Z,O} e^{-\alpha^T X_1}}{\alpha^O} \left[1 - e^{-\alpha^O (X_4 - X_1)} \right] \quad (2-62B)$$

(photons/cm² - sec/mrad/sec)

Similarly, the fluorescent X-ray detector count rate per unit surface dose rate can be obtained from the equation:

$$\frac{C_K^Z}{D} = \frac{I_K^Z}{D} \cdot \epsilon_K^Z \cdot A_2 \cdot p \text{ (counts/sec/mrad/sec)} \quad (2-62C)$$

where:

ϵ_K^Z = detector efficiency

p = collimator open area to total area ratio

A_2 = detector cross-sectional area

The following quantities will be determined for each set of parameter values, in an effort to make the calculated results more useful:

$$1. \frac{I_K^Z (4\pi R^2)}{I_1 A_1}$$

$$2. \frac{I_K^Z}{D} \text{ (photons/cm}^2 \text{ - sec/mrad/sec) or (photons/cm}^2 \text{/mrad)}$$

$$3. \frac{C_K^Z}{D} \text{ (counts/sec/mrad/sec) or (counts/mrad)}$$

The quantity $I_K^Z (4\pi R^2)/I_1 A_1$ is useful because it is independent of the excitation beam intensity and cross sectional area as well as the X-ray detector characteristics. It can then be used as a starting point for making specific source-detector system calculations.

By making additional assumptions about the excitation beam cross-sectional area and the detector-organ separation distance, we can calculate the quantity I_K^Z/D which is independent of the type of X-ray detector being used. The fluorescent X-ray detector characteristics can then be incorporated to determine the fluorescent X-ray count per unit surface dose, C_K^Z/D .

The following assumptions have been made for the example calculations presented in this section:

1. A_1 = excitation beam cross-sectional area = 1 cm^2
2. R = Organ - detector separation = 20 cm
3. ψ = fluorescent X-ray exit angle = 60°

4. ϵ_K^Z = detector efficiency = 100%
5. A_2 = detector cross sectional area = 45.6 cm² (3 in. diameter)
6. p = collimator open area to total area ratio = 0.5.

Since most pharmaceuticals that have been developed for tracer studies have relatively high uptake ratios for the organ or tissue of interest, it will also be assumed that $\alpha^T \approx \alpha^W$, or that X-ray attenuation in the overburden tissue is the same as would be obtained for water. Under these conditions:

$$\alpha^T = \mu_1^W + \frac{\mu_K^W}{\sin \psi} \quad (2-63)$$

$$\alpha^O = \mu_1^O + \frac{\mu_K^O}{\sin \psi} \quad (2-64)$$

and, from Equations 2-46, 2-47, and 2-48,

$$\mu_1^W = (\mu_m)_1^W \rho^W = (\mu_m)_1^W \quad (2-65)$$

$$\mu_K^W = (\mu_m)_K^W \rho^W = (\mu_m)_K^W \quad (2-66)$$

$$\mu_1^O = (\mu_m)_1^Z \rho^O C_Z^O + (\mu_m)_1^W \rho^O (1 - C_Z^O) \quad (2-67)$$

$$\mu_K^O = (\mu_m)_K^Z \rho^O C_Z^O + (\mu_m)_K^W \rho^O (1 - C_Z^O) \quad (2-68)$$

$$\tau_1^{Z,O} = (\tau_m)_1^Z \rho^O C_Z^O \quad (2-69)$$

The approximate equations developed in Section 2.3 can now be used to examine the dependence of $\frac{I_K^Z}{I_1} \cdot \frac{(4\pi R^2)}{A_1}$, $\frac{I_K^Z}{D}$, and $\frac{C_K^Z}{D}$ on the source,

biological system and detector parameters.

2.4.1 Dependence of Fluorescent X-Ray Intensity on Tracer Element Atomic Number

Figures 2-11 through 2-13 illustrate the variations of $\frac{I_K^Z \cdot (4\pi R^2)}{I_1 A_1}$, $\frac{I_K^Z}{D}$, and $\frac{C_K^Z}{D}$ with tracer element atomic number, under the experimental conditions listed on each figure.

The dependence of these quantities on tracer element atomic number is illustrated in Figure 2-11, for an organ depth of 2 cm, an organ thickness (or detector collimator aperture) of 2 cm, a tracer element concentration of 0.01, and an excitation energy of 100 kev. A rather sharp increase in C_K^Z/D is noted with increasing tracer element atomic number for this fixed excitation energy. There are two reasons for this: (1) the K-absorption edge energy is approaching the excitation energy as the atomic number increases, which results in a higher fluorescent X-ray production efficiency, and (2) the fluorescent X-rays from the higher atomic number elements undergo less attenuation in the overburden tissue.

A much different effect is noted if the excitation energy just exceeds the K-absorption edge energy of each element as shown in Figures 2-12 and 2-13. In Figure 2-12, the quantity $I_K^Z (4\pi R^2)/I_1 A_1$ is found to have a maximum value at $Z \approx 56$. Below the maximum, this quantity increases with increasing atomic number because the fluorescent X-ray penetration of overburden tissue is increasing more rapidly than the photoelectric absorption cross section is decreasing. Above the maximum, the opposite condition will obtain. This same type of dependence is observed when we plot I_K^Z/D and C_K^Z/D versus Z for $E_1 \approx E_{K-abs}$ as shown in Figure 2-13. However, in this case the maximum is shifted to a higher atomic number as a result of the increase in I_1/D with E_1 in this energy range (see Figure 2-10).

It should be noted that the variation of C_K^Z/D with tracer element atomic number will also depend on organ depth, organ thickness, and tracer element concentration.

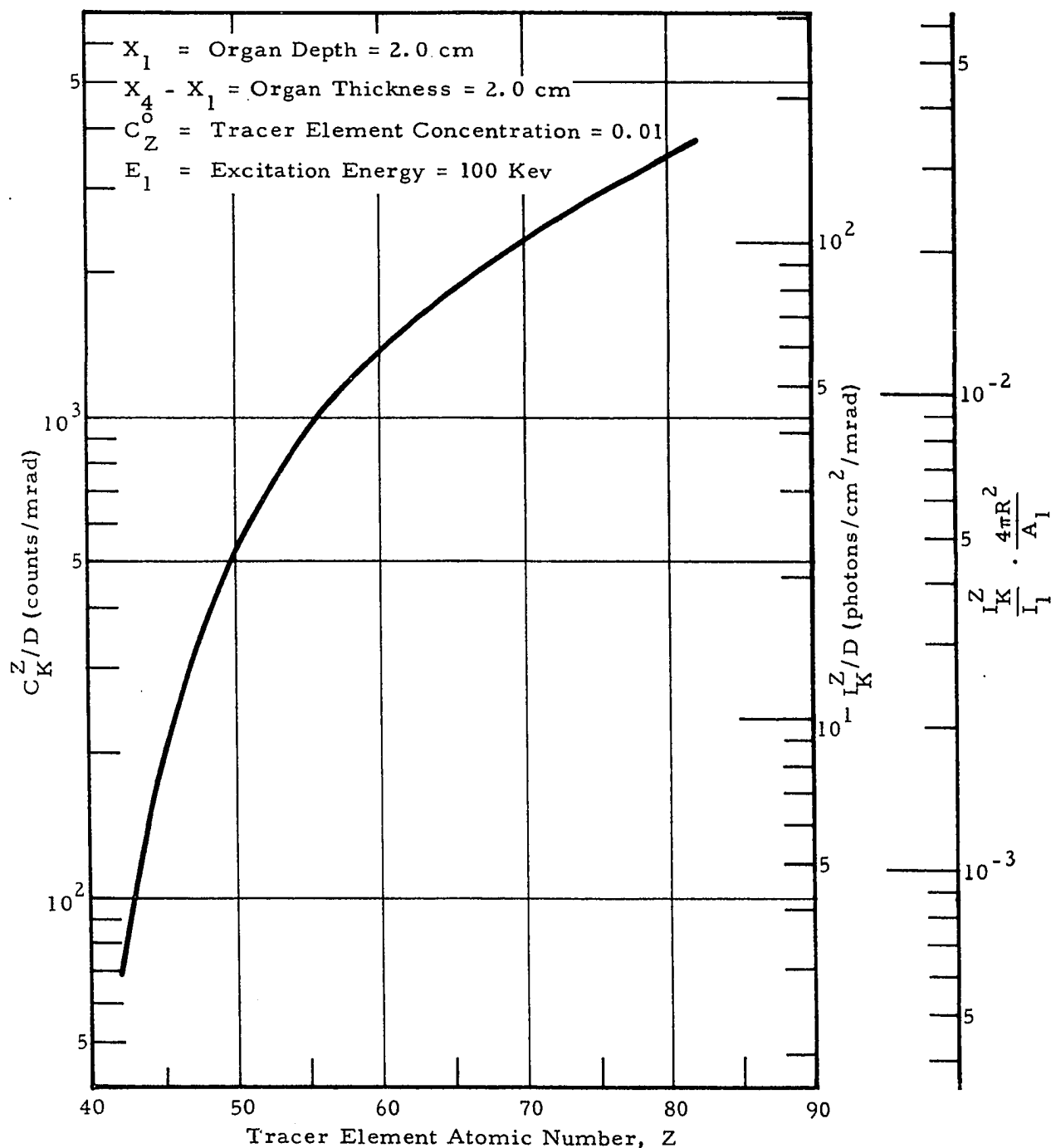


Figure 2-11 Dependence of $I_K^Z/I_1 \cdot 4\pi R^2/A_1$, I_K^Z/D , and C_K^Z/D on Tracer Element Atomic Number for an Excitation Beam Energy of 100 Kev

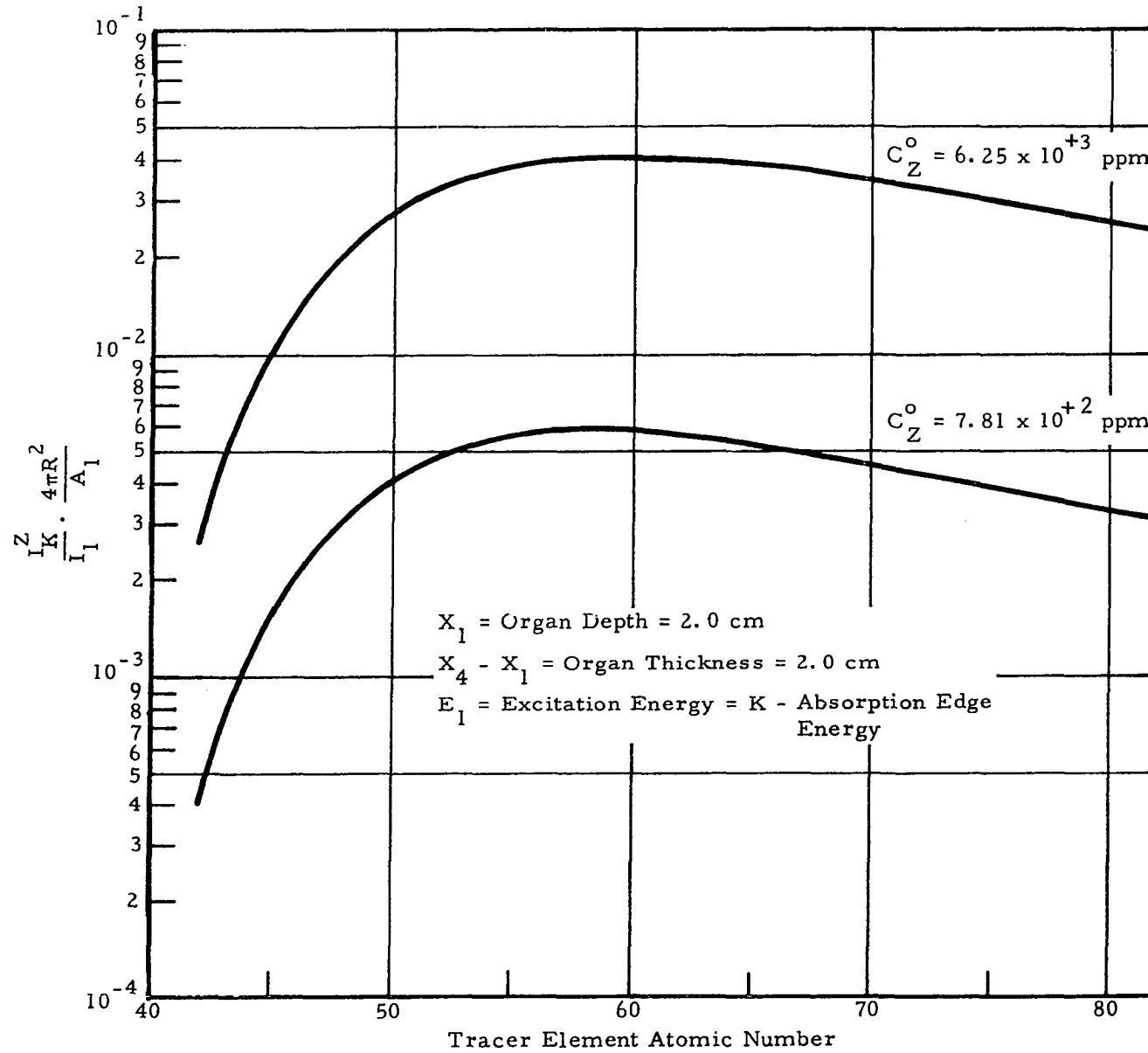


Figure 2-12 Dependence of $\frac{I_K^Z}{I_1} \cdot \frac{4\pi R^2}{A_1}$ on Tracer Element Atomic Number for an Excitation Beam Energy That Just Exceeds the Tracer Element K - Absorption Edge Energy

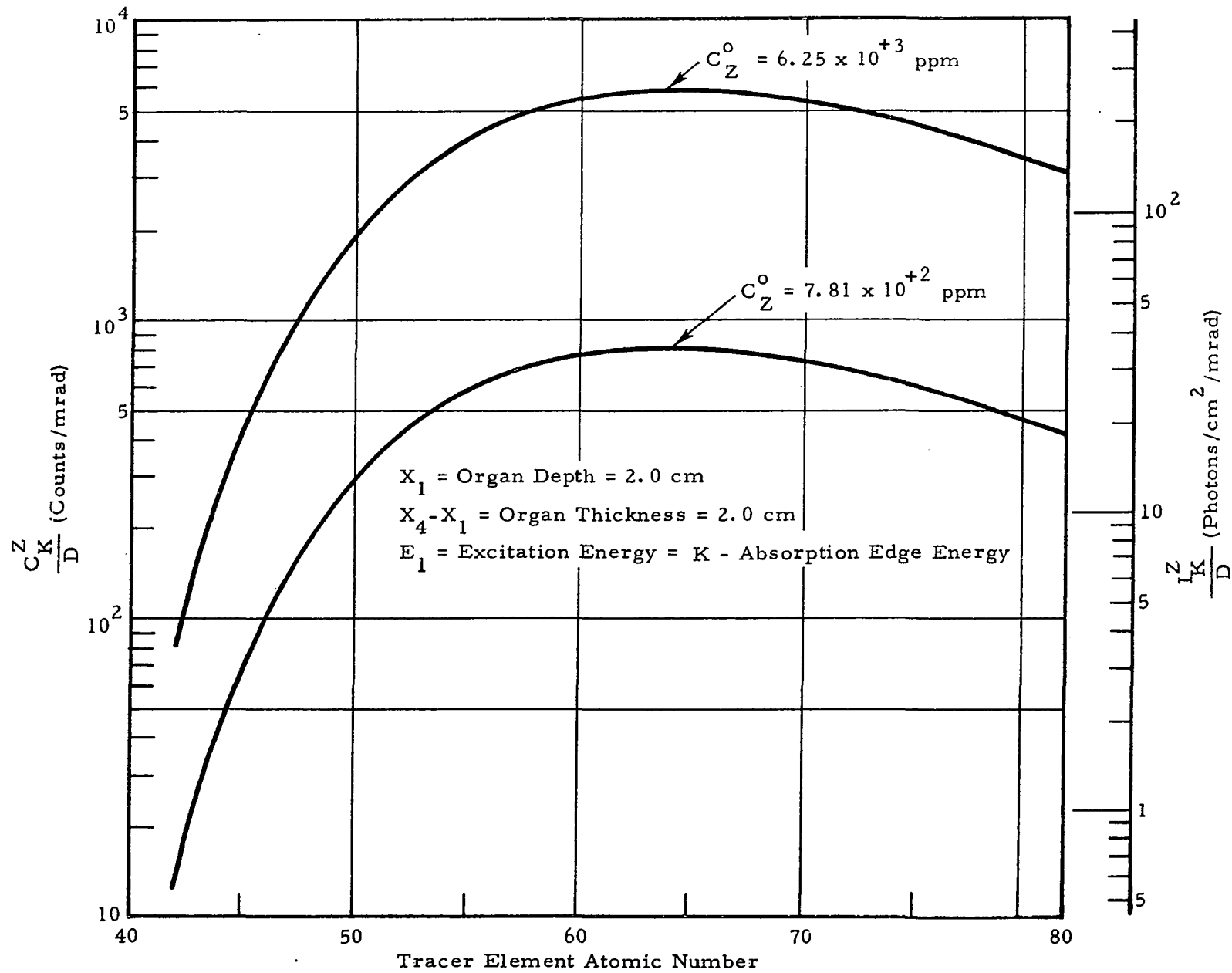


Figure 2-13 Dependence of $\frac{I_K^Z}{D}$ and $\frac{C_K^Z}{D}$ on Tracer Element Atomic Number for an Excitation Beam Energy That Just Exceeds the Tracer Element K - Absorption Edge Energy

2.4.2 Dependence of Fluorescent X-Ray Intensity on Tracer Element Concentration

The dependence of $I_K^Z (4\pi R^2)/I_1 A_1$, I_K^Z/D , and C_K^Z/D on tracer element concentration can be determined from Equations 2-62A, 2-62B and 2-62C when α^O , α^T and $\tau_1^{Z,0}$ are expressed in terms of C_Z^0 by Equations 2-63 through 2-69. Results of some example calculations which illustrate the variation of these quantities with C_Z^0 are presented in Figures 2-14 through 2-17.

The quantity $I_K^Z (4\pi R^2)/I_1 A_1$ is plotted versus concentration in Figure 2-14 for five somewhat randomly selected tracer elements for an organ depth of 2.0 cm, an organ thickness (or detector collimator aperture) of 2.0 cm and an excitation energy that just exceeds the K-absorption edge energy for each element. Under these conditions $I_K^Z (4\pi R^2)/I_1 A_1$ increases almost linearly with tracer element concentration for C_Z^0 less than about 5,000 ppm, but for higher concentrations the increase is less than linear.

Similar curves are obtained when I_K^Z/D and C_K^Z/D are plotted versus C_Z^0 as illustrated in Figure 2-15. These curves illustrate the importance of tracer element selection. Curves of this type would be quite useful for comparing several tracer elements which have different maximum permissible concentrations in a given biological system.

Figures 2-16 and 2-17 illustrate the dependence of $I_K^Z (4\pi R^2)/I_1 A_1$, I_K^Z/D , and C_K^Z/D on tracer element (iodine) concentration for several values of organ depth and organ thickness. The decrease in these quantities with organ depth shown in Figure 2-16 results from the attenuation of primary and secondary radiation in the overburden tissue. The slopes of these curves will then depend on excitation beam energy and tracer element atomic number.

It can be seen from Figure 2-17 that for a given tracer element concentration, the value of C_K^Z/D will approach a maximum value as the

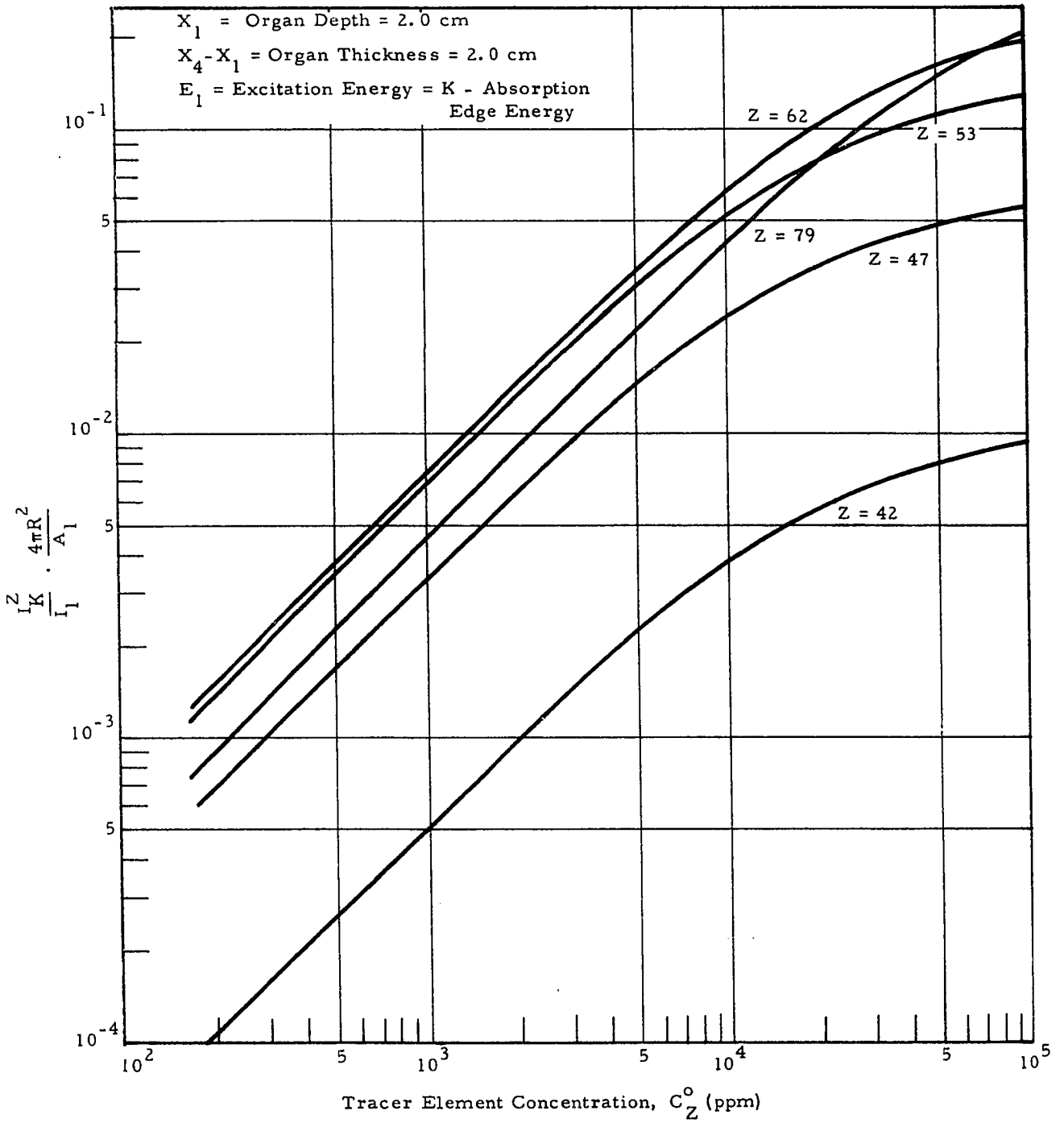


Figure 2-14 Dependence of $I_K^Z (4\pi R^2)/I_1 A_1$ on Concentration for Several Tracer Elements

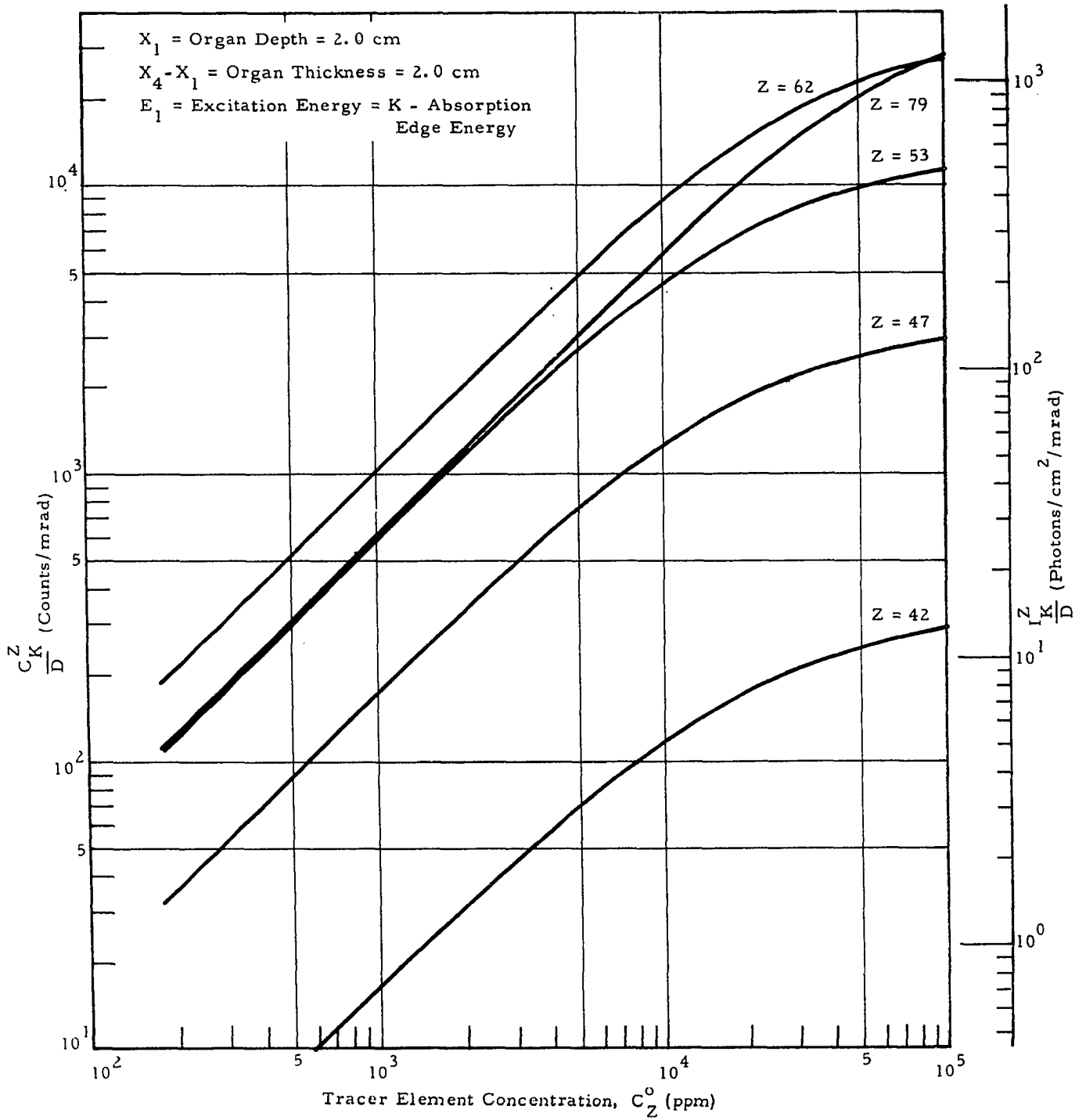


Figure 2-15 Dependence of C_K^Z/D and I_K^Z/D on Concentration for Several Tracer Elements

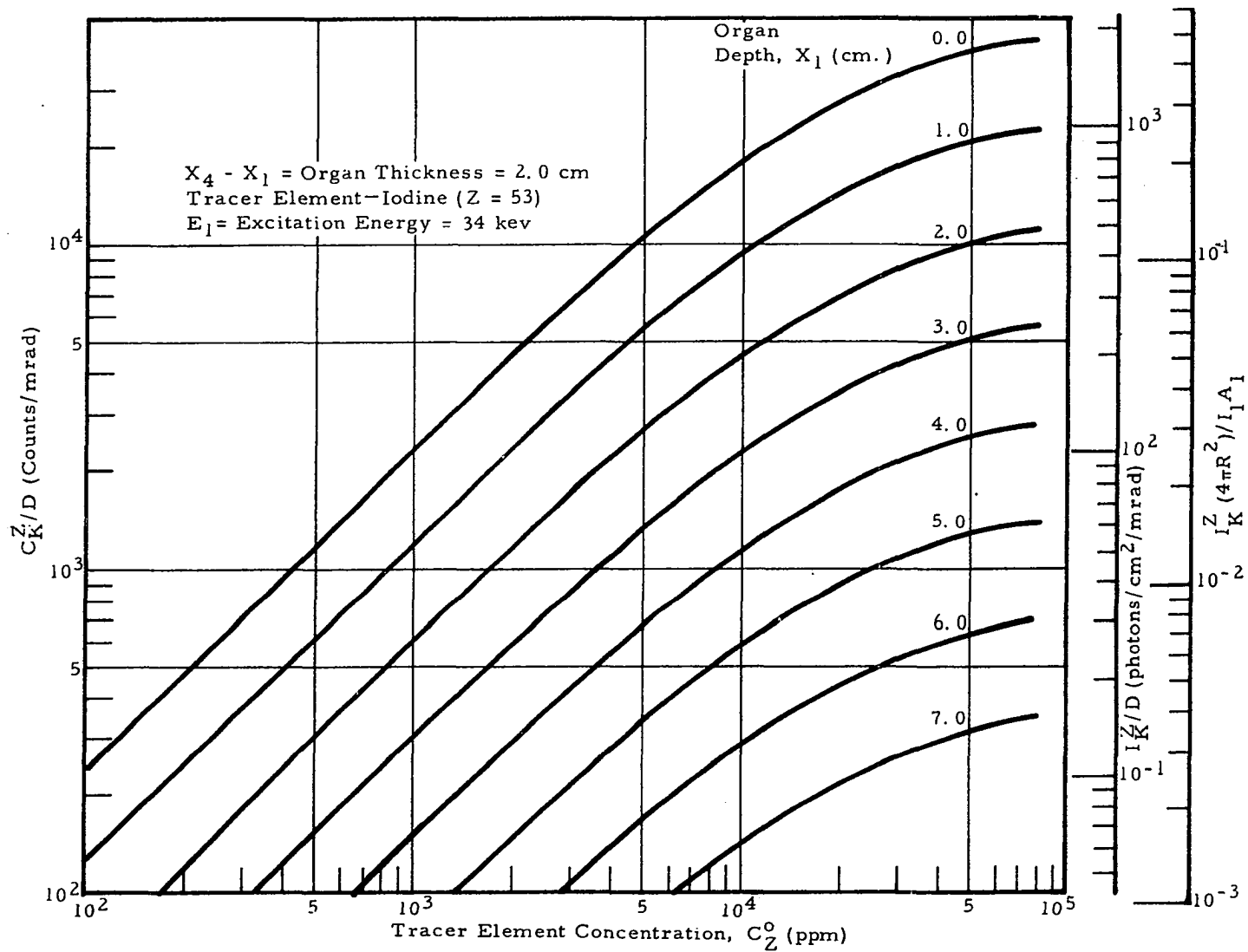


Figure 2-16 Dependence of $I_K^Z(4\pi R^2)/I_1A_1$, I_K^Z/D , and C_K^Z/D on Iodine Concentration for Several Organ Depths

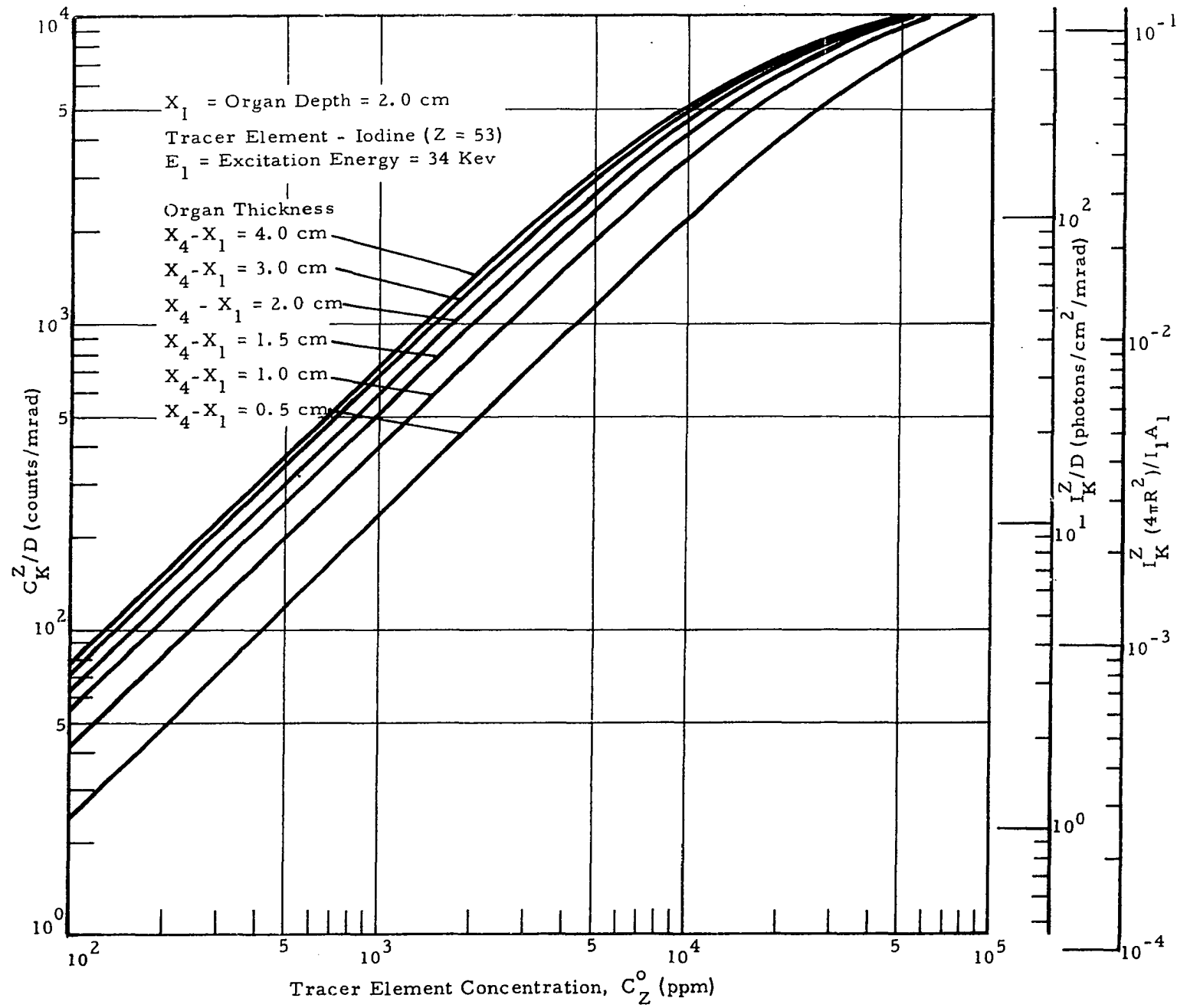


Figure 2-17 Dependence of $I_K^Z/(4\pi R^2)/I_1A_1$, I_K^Z/D , and C_K^Z/D on Iodine Concentration for Several Organ Thicknesses

organ thickness increases. This is a result of excitation beam and fluorescent X-ray attenuation in the organ, and the maximum value of C_K^Z/D will depend on the excitation beam energy as well as the tracer element atomic number and concentration.

Whenever low energy gamma emitters or high-Z tracer element fluorescent X-rays are used for in vivo biological studies, the radiation attenuation along the path from the organ to the detector will be fairly high. However, with fluorescent X-rays the radiation production rate will also decrease as depth in the organ increases. With radioactive tracers, the specific activity will be fairly independent of depth. It is important therefore, to examine the dependence of the fluorescent X-ray production rate on depth in the organ and to compensate for this effect if necessary. One method of achieving this will be described in Section 2.9.

It is apparent from Equation 2-61 and Figures 2-14 through 2-17 that "thin organ" and "thick organ" approximations can be made to simplify the calculation of fluorescent X-ray intensity for some application. This same approximation procedure has been applied to X-ray spectroscopy (Ref. 3).

Thin Organ Approximation

If the organ is "thin", or the term $\alpha^O(X_4 - X_1)$ is small, the exponential term $e^{-\alpha^O(X_4 - X_1)}$ in Equation 2-61 can be approximated by:

$$e^{-\alpha^O(X_4 - X_1)} \approx 1 - \alpha^O(X_4 - X_1) \quad (2-70)$$

The error resulting from this substitution will be less than 10 percent if the value of $\alpha^O(X_4 - X_1)$ is less than 0.4, or if:

$$(X_4 - X_1) < \frac{0.4}{\alpha^O}$$

where α^O is a function of tracer element atomic number, tracer element concentration, and X-ray energy. In this case, Equation 2-61 reduces to:

$$I_K^Z = B e^{-\alpha^T X_1} \tau_1^Z \alpha^O(X_4 - X_1) \quad (2-71)$$

or:

$$I_K^Z = B e^{-\alpha^T X_1} (\tau_m^Z)^Z \frac{\rho^Z C_Z^0 (X_4 - X_1)}{\rho^Z + (1 - \rho^Z) C_Z^0} \quad (2-72)$$

where $\tau_1^{Z,0}$ has been replaced by Equation 2-69. Equation 2-72 illustrates that for a "thin organ", I_K^Z is linearly dependent on organ thickness $(X_4 - X_1)$ and the dependence of I_K^Z on tracer element concentration C_Z^0 is given by equation:

$$I_K^Z \propto \frac{C_Z^0}{\rho^Z + (1 - \rho^Z) C_Z^0} \quad (2-73)$$

If the tracer element concentration in the organ is less than about 50,000 ppm, the term $(1 - \rho^Z) C_Z^0$ in the denominator of Equation 2-73 can be neglected and I_K^Z is directly proportional to C_Z^0 .

Thick Organ Approximation

If the organ is "thick", or the term $\alpha^0 (X_4 - X_1)$ is large, the exponential term $e^{-\alpha^0 (X_4 - X_1)}$ in Equation 2-61 can be neglected. This approximation will result in an error of less than 10 percent if the value of $\alpha^0 (X_4 - X_1)$ is larger than 2.3, or if:

$$(X_4 - X_1) > \frac{2.3}{\alpha} \quad (2-74)$$

Under these conditions Equation 2-61 becomes:

$$I_K^Z = \frac{B e^{-\alpha^T X_1} \tau_1^{Z,0}}{\alpha^0} \quad (2-75)$$

or:

$$I_K^Z = \frac{Be^{-\alpha} T_{X_1} (\tau_m)_1^Z C_Z^0}{(\mu_m)_1^w + \frac{(\mu_m)_K^w}{\sin \psi} + (\mu_m)_1^Z - (\mu_m)_1^w + \frac{(\mu_m)_K^Z - (\mu_m)_K^w}{\sin \psi}} C_Z^0 \quad (2-76)$$

where $\tau_1^{Z,O}$ and α^O have been expressed in terms of C_Z^0 by using Equations 2-69, 2-64, 2-67, and 2-68. As expected, I_K^Z is independent of organ thickness and, for very low concentrations of tracer element Z in the organ, I_K^Z is directly proportional to C_Z^0 .

Equation 2-74 has particular significance if one is interested in looking for defects in a relatively thick organ. If the detection system being used requires a 10% change in I_K^Z for positive identification, then

$(X_4 - X_1)$ described in Equation 2-74 is essentially an infinite thickness. Thus, small defects at a depth approaching X_4 would not be expected to produce an identifiable change in I_K^Z . Equation 2-74, from this standpoint, can be used as a rough indication of the maximum organ thickness for which small defects in the organ can be suitably delineated. This point will be discussed in more detail in Section 2.9.

2.4.3 Dependence of Fluorescent X-Ray Intensity on Excitation Energy

In this section, two types of excitation sources will be considered: (1) monoenergetic sources such as gamma emitting radioisotopes, internal conversion radioisotopes that emit fluorescent X-rays, and X-ray machines fitted with secondary radiators (Ref. 20, 21) and (5) mixed radiation sources such as X-ray machines and beta excited X-ray sources (Ref. 22-32).

2.4.3.1 Monoenergetic Excitation Source

Since a monoenergetic excitation source was assumed in the development of Equations 2-62A, 2-62B, and 2-62C, the dependence of $I_K^Z (4\pi R^2)/I_1 A_1$, I_K^Z/D , and C_K^Z/D can be determined from these equations

by making use of the assumptions and calculation procedures described in the introduction of this section. The results of some example calculations using different assumed values of the variable parameters are presented graphically in Figures 2-18 through 2-23.

In Figure 2-18, the dependence of $I_K^Z(4\pi R^2)/I_1 A_1$ on the ratio of excitation energy to K-absorption edge energy is illustrated for several elements with an assumed organ depth of 2.0 cm, an organ thickness of 2.0 cm, and a tracer element concentration of 10^4 ppm. Similar curves for I_K^Z/D and C_K^Z/D under these same conditions are presented in Figure 2-19. It is apparent that a rather rapid decrease in fluorescent X-ray production efficiency occurs as the ratio E_1/E_{K-abs} increases. However, it should not be assumed from these results that under all conditions, the most suitable excitation energy is just above the K-absorption edge energy of the tracer element. The fact that this is not always true can be seen from Figure 2-20 where Iodine K X-ray intensity has been plotted versus E_1/E_{K-abs} for several organ depths. Iodine, in this example, is the tracer element with a concentration of 1.56×10^3 ppm in a 2.0 cm thick organ. We see here, that for an organ depth of 8.0 cm, the highest fluorescent X-ray count per unit surface dose is obtained for $E_1/E_{K-abs} \approx 1.5$ which results from the increased excitation beam penetration at this energy. The most suitable monoenergetic source must therefore be determined from a detailed examination of the biological system parameters involved in any given experiment.

2.4.3.2 Mixed Radiation Excitation Source

The radiation spectrum from an X-ray machine or a beta excited X-ray source is determined by the energy distribution of the electrons that are incident on the target, the target composition, and various geometry factors. The following discussion will be restricted to D.C. X-ray machines for which the electrons striking the tube target can be considered monoenergetic for simplicity. However, this type of analysis can be extended with some difficulty, to include full-wave and half-wave rectified X-ray machines as well as beta excited X-ray sources.

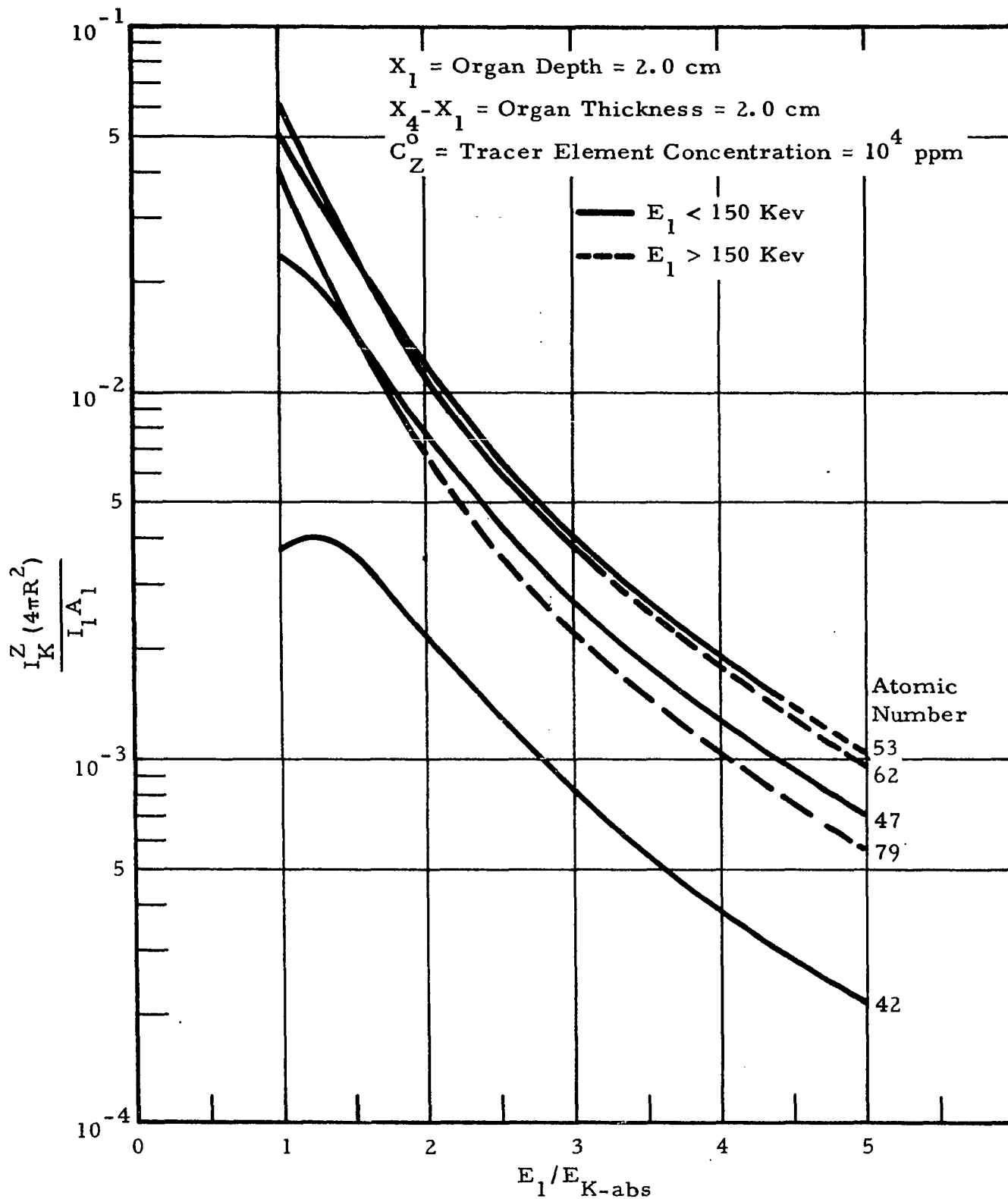


Figure 2-18 Dependence of $I_K^Z (4\pi R^2) / I_1 A_1$ on Excitation Energy for Several High-Z Elements

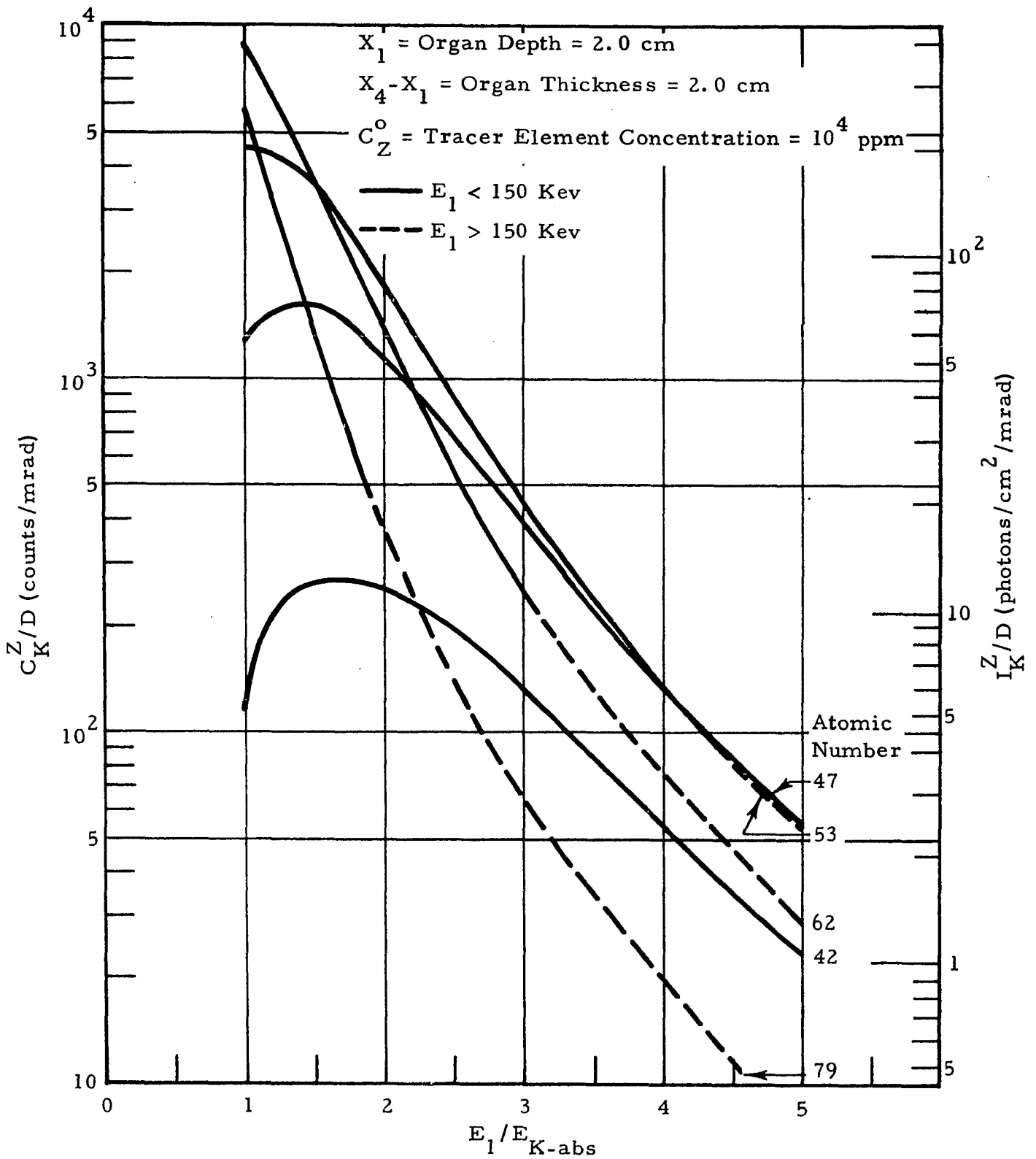


Figure 2-19 Dependence of C_K^Z/D and I_K^Z/D on Excitation Energy for Several High-Z Elements

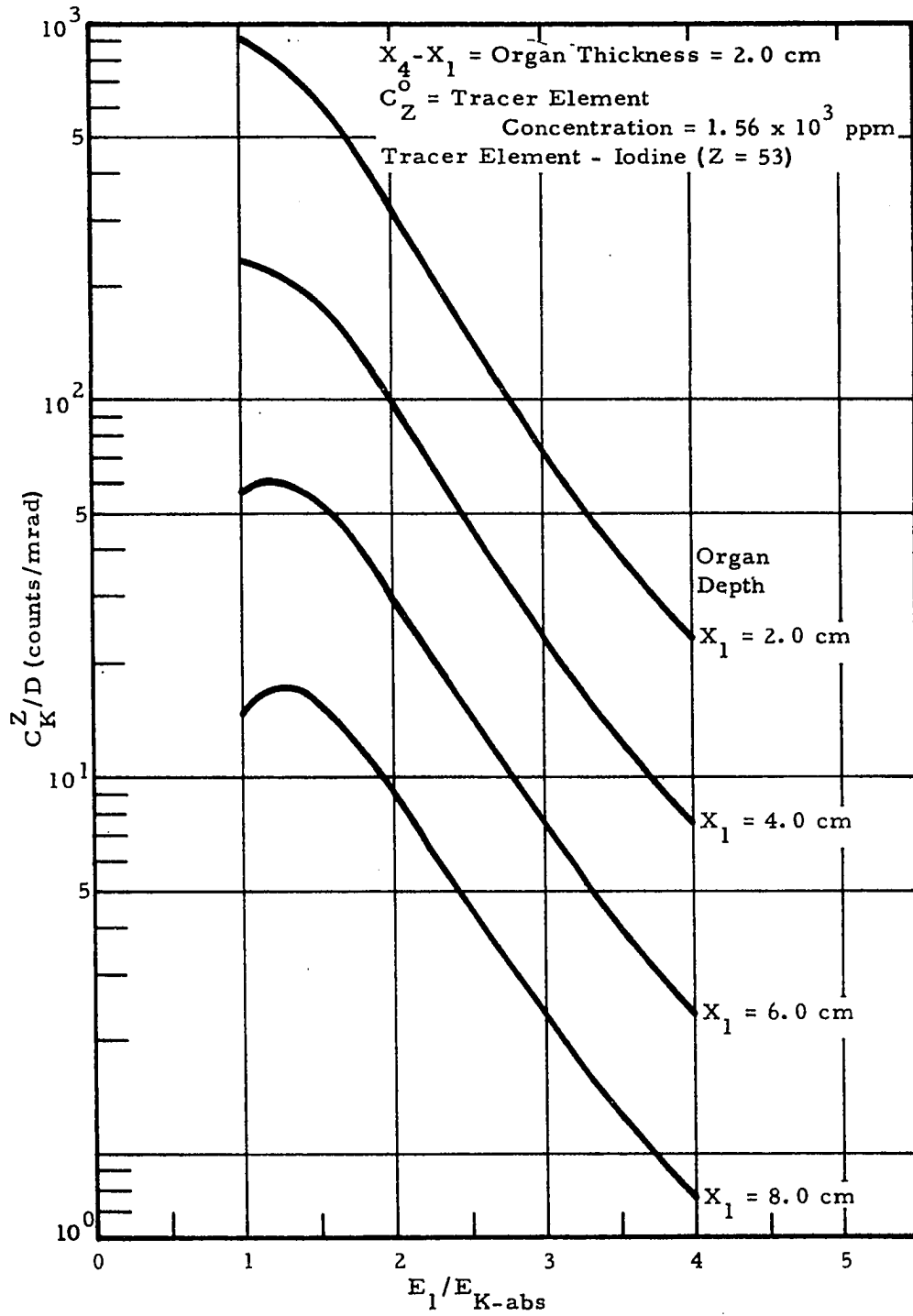


Figure 2-20 Dependence of C_K^Z / D on Excitation Energy for Several Organ Depths

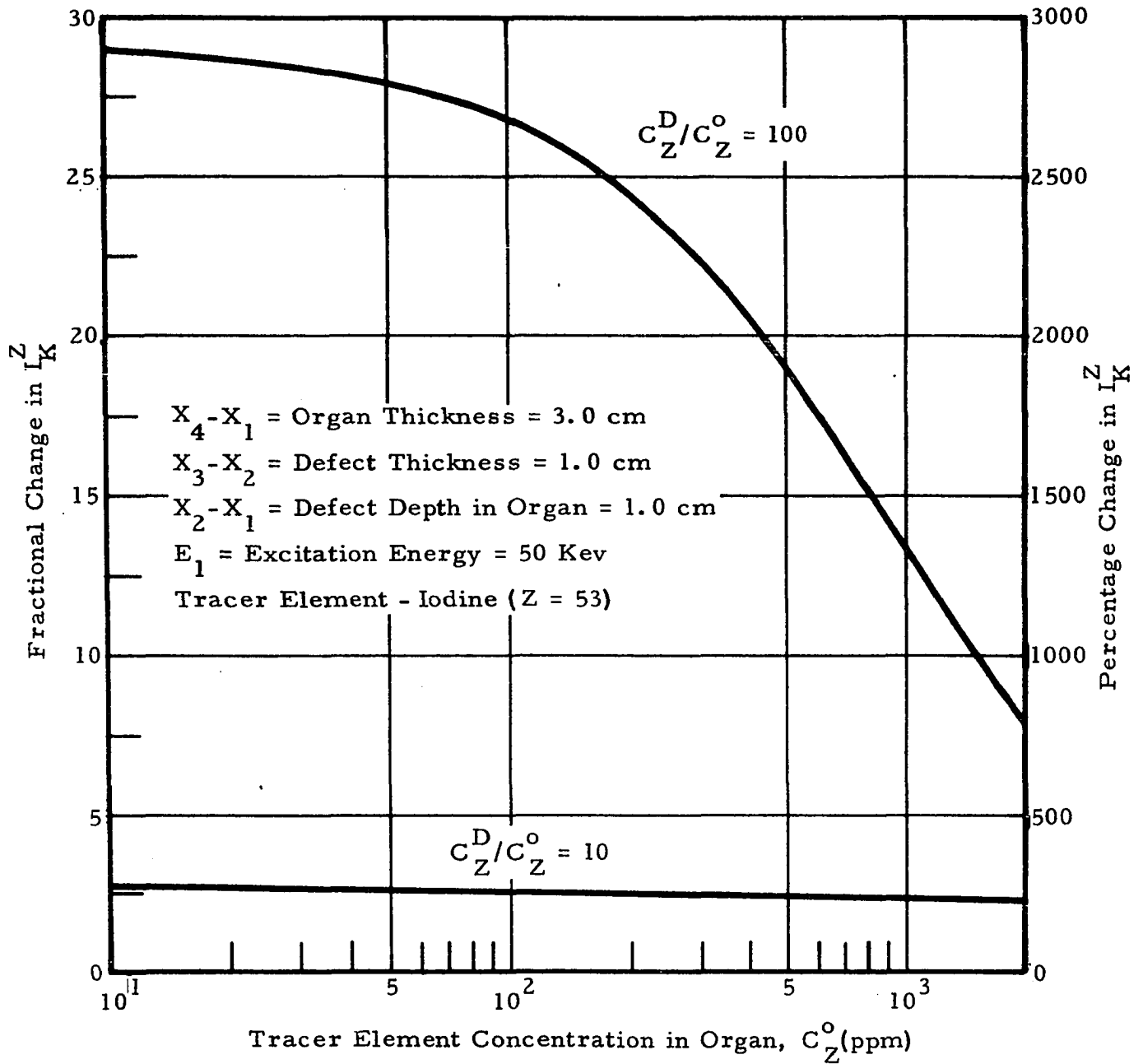


Figure 2-21 Change in I_K^Z as Source-Detector Assembly Passes
 Over 1.0 cm "Hot Spot" Defect in 3.0 cm Thick Organ

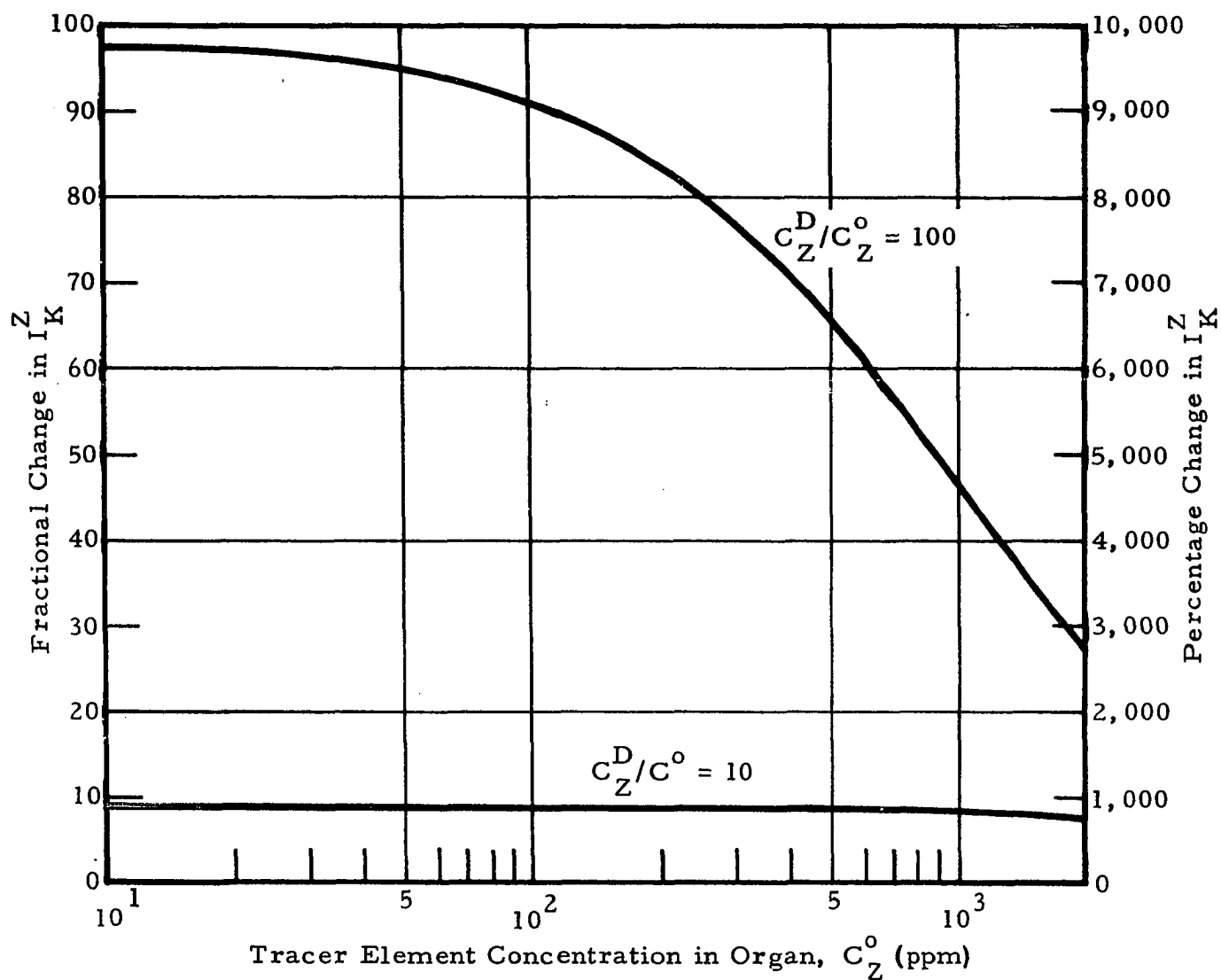


Figure 2-22 Change in I_K^Z as Source Assembly Passes Over 1.0 cm "Hot Spot" Defect in 1.0 cm Thick Organ

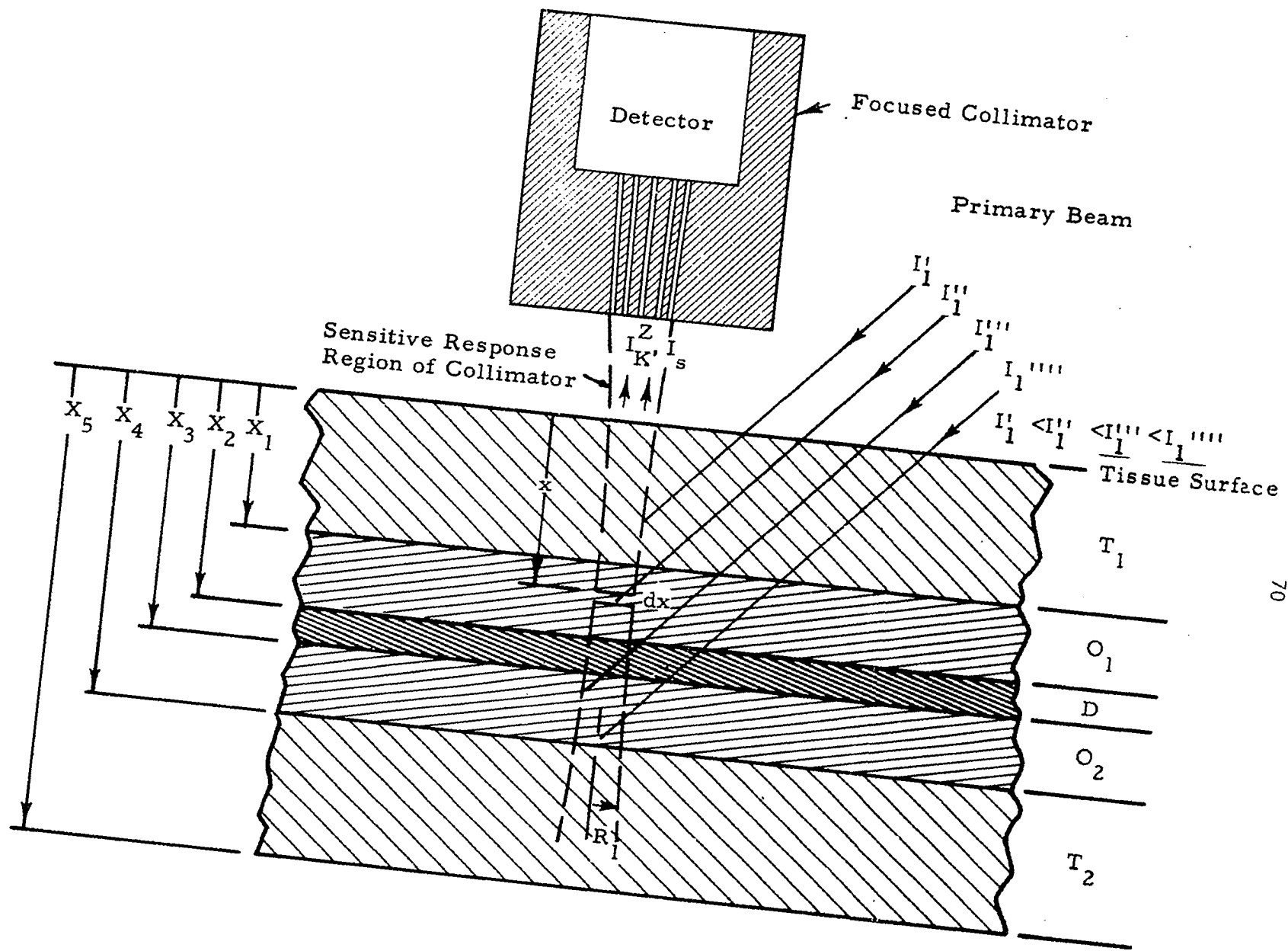


Figure 2-23 Scheme for Producing Uniform Depth Sensitivity

The radiation produced by a D. C. X-ray machine is composed of the fluorescent X-ray line spectrum of the target material superimposed on a continuous bremsstrahlung spectrum. The intensities of these two radiation components can be expressed in terms of the D. C. voltage applied to the X-ray tube by the approximate equations (Ref. 1):

$$I_{1K'} = K_1 (V - E_{K'-abs})^2 \text{ (photons/cm}^2\text{-sec)} \quad (2-77)$$

$$I_{1C} = K_2 (VE_1^2 - E_1^3) \text{ (photons/cm}^2\text{-sec)} \quad (2-78)$$

where $I_{1K'}$ = intensity of target material K' - series fluorescent X-rays

$E_{K'-abs}$ = excitation potential of target material K' -series fluorescent X-rays

V = X-ray tube voltage ($V < 3E_{K'-abs}$)

I_{1C} = intensity of continuous spectrum at energy E_1

K_1 and K_2 are constants

If the K' -series fluorescent X-rays from the X-ray tube target have energies greater than the K -absorption edge energy of the tracer element in the biological system, I_K^Z can be expressed as the sum of two terms:

$$I_K^Z = I_K^Z(1K') + I_K^Z(1C) \quad (2-79)$$

where $I_K^Z(1K')$ represents the tracer element K -series fluorescent X-ray intensity at the detector produced by K' -series fluorescent X-rays from the tube target and $I_K^Z(1C)$ represents the intensity resulting from bremsstrahlung excitation.

According to Equation 2-61, I_K^Z is directly proportional to I_1 . Thus, from Equation 2-77 for $I_{1K'}$, we can write the variation of $I_K^Z(1K')$ with V as:

$$I_K^Z(1K') \propto (V - E_{K'-abs})^2 \quad (2-80)$$

The development of an expression for $I_K^Z(1C)$ is slightly more complicated. In this case I_K^Z and I_1 in Equation 2-61 must be replaced by $dI_K^Z(1C)$ and dI_{1C} , to determine the intensity of tracer element fluorescent X-rays produced by bremsstrahlung photons in the incremental energy range dE_1 at energy E_1 . Or:

$$dI_K^Z(1C) = \frac{A_1 \omega_K^Z}{4\pi R^2} \cdot \frac{r_K^Z - 1}{r_K^Z} \cdot \frac{e^{\alpha^T X_1} \tau_1^{Z,0}}{\alpha^0} \left[1 - e^{-\alpha^0 (X_4 - X_1)} \right] dI_{1C} \quad (2-81)$$

where α^T , α^0 and $\tau_1^{Z,0}$ depend on the primary X-ray energy E_1 . From Equation 2-78, dI_{1C} can be expressed in terms of V and E_1 by the equation:

$$dI_{1C} = K_2 (2VE_1 - 3E_1^2) dE_1 \quad (2-82)$$

and $dI_K^Z(1C)$ can now be determined as a function of X-ray tube voltage by replacing α^T , α^0 , and $\tau_1^{Z,0}$ in Equation 2-81 by the corresponding mass absorption and attenuation coefficients according to Equation 2-63 through 2-69 and using the approximate equations developed in Section 2.3, which relate these coefficients to primary X-ray energy, E_1 . The expression for $dI_K^Z(1C)$ must then be integrated over E_1 from $E_1 = E_{K-abs}$ to $E_1 = V$:

$$I_K^Z(C1) = \frac{K_2^A \omega_K^Z}{4\pi R^2} \cdot \frac{r_K^Z - 1}{r_K^Z} \int_{E_{K-abs}}^V \frac{e^{-\alpha^T(E_1)X_1} \tau_1^{Z, 0}(E_1)}{\alpha^0(E_1)} \left\{ 1 - e^{-\alpha^0(E_1)[X_4 - X_1]} \right\} [2VE_1 - 3VE_1^2] dE_1 \quad (2-83)$$

which results in a rather complicated polynomial expression for $I_K^Z(C1)$ in terms of V and E_{K-abs} .

The dependence of the intensity of the K_α line of the secondary spectrum of copper excited by the continuous spectrum of an X-ray tube with a silver anode was studied by Blokhin (Reference 1). The curve of the data could be fit by an empirical formula:

$$I_K^Z(C1) \propto (V - E_{K-abs})^{1.79} \quad (2-84)$$

where E_{K-abs} is the excitation potential of the K-level of copper. This same variation of $I_K^Z(C1)$ with V has been observed when iodine K-series X-rays are excited by the continuous radiation from an X-ray tube with a tungsten target. These results will be discussed in the experimental verification section of this thesis.

From a practical standpoint, it can be seen from Figures 2-19 and 2-20 that mixed radiation sources are inferior to monoenergetic sources for exciting high-Z tracer element fluorescent X-rays in a biological system. This results from the fact that primary X-rays below the K-absorption edge energy of the tracer element will not excite K-series fluorescent X-rays and the efficiency for fluorescent X-ray production decreases rapidly above this energy. However, all primary X-rays will contribute to the radiation dose delivered to the biological system. This problem can be minimized by selective filtration but it cannot be completely eliminated. The use of a mixed primary X-ray beam can also result in an excessive scattered radiation component at the detector. These

considerations will be discussed in more detail in subsequent sections of this paper and are introduced at this time only to illustrate the limitations associated with this type of excitation source.

2.4.4 Defect Localization

Medical radioisotopic scanning is a well established technique for locating organ defects, such as brain, thyroid, liver, and bone tumors in vivo. Depending on the physiological characteristics of the biological system and the radiopharmaceutical involved, the defect will have a higher or lower radioactive tracer concentration than the surrounding organ or tissue. Such regions are conventionally designated as "hot spots" and "cold spots".

Through the development of suitable primary X-ray sources and fluorescent X-ray detectors, it is quite possible that fluorescent X-rays produced in nonradioactive high-Z tracer elements can be used to conduct these same types of investigations. One must first determine the change in fluorescent X-ray intensity that will occur when a defect is present in the biological system being examined to evaluate this possibility.

From Figure 2-4 and Equation 2-33, the fractional change, F. C. in tracer element fluorescent X-ray intensity at the detector as the source-detector assembly passes over a region of the biological system that contains a defect is given by the equation:

$$\begin{aligned}
 \text{F. C.} &= \frac{I_K^Z(0+D) - I_K^Z(0)}{I_K^Z(0)} = \\
 &= \frac{-e^{-\alpha^0(X_2 - X_1)} \left\{ e^{\alpha^0(X_2 - X_1)} - 1 + e^{-\alpha^D(X_4 - X_3)} [1 - e^{-\alpha^0(X_4 - X_3)}] \right.}{\left. + \frac{\tau_{Z, D}^0}{\tau_{Z, 0}^D} \left[1 - e^{\alpha^D(X_3 - X_2)} \right] \right\}}{[1 - e^{-\alpha^0(X_4 - X_1)}]} \quad (2-85)
 \end{aligned}$$

where $I_K^Z(0+D)$ is the fluorescent X-ray intensity from the region of the organ which contains a defect and $I_K^Z(0)$ is the fluorescent X-ray intensity from the adjacent organ material. The usefulness of this equation can be demonstrated by calculating values of F. C. for the following special

cases: (1) a 3.0 cm thick organ containing a 1.0 cm thick defect at its center, and (2) a 1.0 cm thick organ containing a 1.0 cm thick defect. It will be assumed that the tracer element is iodine and that the primary X-ray energy is 50 keV for these calculations.

Equation 2-85 in the first case, reduces to:

$$\frac{e^{-\alpha O} \left[e^{-2\alpha O} - 1 + (1 - e^{-\alpha D}) \left(e^{-\alpha D} + \frac{\tau_1^{Z, D} \alpha^O}{\tau_1^{Z, O} \alpha^D} \right) \right]}{1 - e^{-3\alpha O}} \quad (2-86)$$

and for the second case we obtain:

$$(F. C.)_2 = \frac{\tau_1^{Z, D} \alpha^O}{\tau_1^{Z, O} \alpha^D} \left[\frac{1 - e^{-\alpha D}}{1 - e^{-\alpha O}} \right] - 1 \quad (2-87)$$

where: $\tau_1^{Z, D} = (\tau_m)^Z \rho^D C_Z^D$

$$\alpha^D = \mu_1^D + \mu_K^D / \sin \psi$$

$$\mu_1^D = (\mu_m)^Z \rho^D C_Z^D + (\mu_m)^W \rho^D (1 - C_Z^D)$$

$$\mu_K^D = (\mu_m)_K^Z \rho^D C_Z^D + (\mu_m)_K^W \rho^D (1 - C_Z^D)$$

Values of (F. C.) calculated from Equation 2-86 for "hot spot" defects with defect-to-organ concentration ratios of 10 and 100 are presented in Figure 2-21 as a function of tracer element (iodine) concentration in the organ. These changes are quite large compared to the fraction changes in fluorescent X-ray intensity for "cold spot" defects under these same conditions. For "cold spot" defects, (F. C.) varies

from about -0.26 to -0.30 (26 to 30%) for $C_Z^D \leq 0.1 C_Z^0$, and is essentially independent of the ratio C_Z^D/C_Z^0 (for $C_Z^D \leq 0.1 C_Z^0$) over tracer element concentration range illustrated in Figure 2-21.

"Hot spot" defect fractional changes in fluorescent X-ray intensity for defect-to-organ concentration ratios of 10 and 100 are shown in Figure 2-22 for a 1.0 cm thick organ containing a defect of the same thickness. Again, the fractional change in fluorescent X-ray intensity for "hot spot" defects is quite large and approaches the value of C_Z^D/C_Z^0 at low organ concentrations. Under these same conditions, the value of $(F.C.)_2$ for "cold spot" defects can be approximated by the equation:

$$(F.C.)_2 \approx \frac{C_Z^D - C_Z^0}{C_Z^0} \quad (2-88)$$

which is essentially - 1.0(100%) for $C_Z^D < 0.1 C_Z^0$.

2.5 FLUORESCENT X-RAY TO SINGLE COMPTON SCATTER X-RAY INTENSITY RATIO

When a monoenergetic excitation source with an energy that just exceeds the K-absorption edge energy of the tracer element is used, two high intensity X-ray peaks are recorded by the X-ray detector. One of these peaks corresponds to the K-series fluorescent X-rays from the tracer element and the other to single Compton scattered primary X-rays. If we consider an organ that does not contain a defect, the intensity ratio of these two peaks I_K^Z/I_S for the geometry illustrated in Figure 2-4 can be obtained from Equations 2-34 and 2-61.

$$\frac{I_K^Z}{I_S} = \frac{\frac{B e^{-\alpha^T X_1} \tau_1}{\alpha^0} [1 - e^{-\alpha^0 (X_4 - X_1)}]}{\frac{L e^{-\beta^T X_1} \sigma_1}{\beta^T} [1 - e^{-\beta^T (X_4 - X_1)}]} \quad (2-89)$$

However, since it has been assumed that $E_1 \approx E_{K-abs}$ and, to a first approximation, $E_K \approx E_{K-abs} \approx E_s$ for large angle scattering at low energies, we can assume that $\alpha^T \approx \alpha^O \approx \beta^T$. Equation 2-89 then reduces to the approximate expression:

$$\frac{I_K^Z}{I_S} \approx \frac{\beta \tau_1^{Z,O}}{L \sigma_1^T} \quad (2-90)$$

If the linear absorption and scattering coefficients in this equation are replaced by the corresponding mass absorption and scattering coefficients, we obtain:

$$\frac{I_K^Z}{I_S} \approx G C_Z^0 \quad (2-91)$$

where:

$$G = \frac{B(\tau_m)^Z}{L(\sigma_m)^T} = \text{constant}$$

Under these conditions, the intensity ratio I_K^Z/I_S depends primarily on the concentration of tracer element and is essentially independent of the densities and absorption coefficients of the biological system, including the overburden material. This type of relationship has already been used effectively for the analysis of ores by radioisotope X-ray spectrometry (Ref. 33) and could be quite useful for in vivo fluorescent X-ray studies when the region being examined includes a bone, void, or other discontinuities.

2.6 COMPARISON WITH CONVENTIONAL RADIOISOTOPE STUDIES

In this section, a brief attempt will be made to illustrate some of the basic similarities and differences between the techniques of using

gamma rays emitted by radioactive materials and fluorescent X-rays emitted by externally excited high-Z tracer elements for studying organ circulation, function, and structure in vivo. To develop the fluorescent X-ray technique described in this report to a level at which meaningful in vivo studies can be conducted will require close collaboration between physicians, physicist, engineers, and pharmaceutical chemists over an extended period of time. However, it is possible at this time to examine the types of investigations that are presently being conducted with radioactive tracers and to discuss some of the advantages and limitations of using externally excited fluorescent X-rays for these applications. The following discussion will be separated into the two general categories of dynamic function studies and scanning for convenience.

2.6.1 Dynamic Function Studies

Dynamic function studies are concerned primarily with the rate of uptake, total accumulation, and subsequent release of a tracer element from an organ or other biological structure. This can be accomplished in either of two ways; the circulating blood can be examined to determine the change of concentration with time of a material that is selectively removed from the blood by the organ of interest, or the organ can be examined directly to determine the three basic parameters listed above. (Ref. 34).

The examination of the circulating blood can be achieved by an arterial puncture to divert the flow of blood to an external detector, by the extraction of a blood sample, or by monitoring in vivo the concentration of the tracer element in a large artery or blood pool such as the heart or brain. The later method has been applied to the measurement of hepatic blood flow based on the rate of removal of colloidal particles from the peripheral blood by the reticuloendothelial cells. Since the primary sites of reticuloendothelial cells are the liver and spleen, the rate of clearance of colloidal material must depend mainly on the blood flow to these organs (Ref. 34). Colloidal radio-gold has been utilized for studies of this type with the gamma-ray detector being placed laterally over the temporal region of the head. (Ref. 35-36).

A similar technique has been developed to study renal blood flow following the administration of ^{131}I -tagged O-iodohippurate (Hippuran). (Ref. 37).

When an organ is examined in vivo to determine the rate of uptake, total accumulation, and rate of disappearance of a tracer element from the organ, two types of tracer materials can be employed: (1) tracer materials that can be injected into the organ without being metabolized, and (2) tracer materials that are removed from circulation by the organ. This first group of materials includes noble gases such as Xe¹³³ and Kr⁸⁵, which can be used for coronary, (Reference 38) hepatic, and brain cortical blood-flow (Reference 5) investigations, as well as various radioactive tracers that have been used to measure cardiac output (Reference 39 - 43). Included in the second group are bromsulfalein and radioiodine-tagged rose bengal which have been used for liver function tests (Reference 44) (hepatogram) and Hippuran, a material used in kidney function studies (renogram).

In each of the examples given above, a fixed-position external gamma-ray detector is used to monitor the concentration of radioactive material either in a large blood pool or in the organ being investigated. Typically, collimators are added to the detector to define the region of maximum response.

The use of radioactive tracers for these studies, though widely used and providing several excellent diagnostic procedures, has some basic limitations. For example, when the required information must be obtained in a short period of time, such as for cardiac output calculations, a relatively large tracer dose must be administered to obtain a statistically acceptable count rate at the detector. As a result, the patient will continue to receive a high radiation dose rate after the investigation has been completed. The accumulated dose and depth dose distribution will depend on the gamma ray energy as well as the physical and physiological properties of the radiopharmaceutical being used.

Interference can result from the accumulation of tracer material in adjacent tissues. This effect can be minimized by proper collimator design and the development of tracer materials that have high uptake ratios for the organ being examined, but it is still troublesome in many applications.

In the event that suitable instruments, pharmaceutical materials, and clinical techniques can be developed for conducting dynamic function studies with fluorescent X-rays emitted by externally excited high-Z

tracers, several unique advantages over some of the existing procedures can be realized. Most important is the possibility of reducing the radiation dose to the biological system. This can be accomplished by confining the primary X-ray beam to the immediate region under investigation, terminating the radiation exposure at the conclusion of the study, and using a low duty cycle on the primary X-ray beam when the tracer element concentration must be monitored over a long time interval. Although it is impossible to predict the radiation dose reduction that can be realized in any particular application until the necessary instruments and pharmaceutical techniques have been developed, it is apparent from the calculations in the preceding section that it could be substantial. Another advantage of this technique would be the ability to control the region of the biological system from which radiation that will subsequently reach the detector is emitted. Presently, this is being accomplished by the use of radioactive tracers that have high uptake ratios for the organ or tissue of interest and by detector collimation. However, if externally excited fluorescent X-rays are used, the primary X-ray beam in conjunction with the aperture of the detector collimator, will define precisely the region of the biological system that is being examined. In some cases, this technique could be used to reduce the interference that frequently results from the accumulation of the tracer material in adjacent tissues. Also, since the tracer material is not radioactive, the study could be repeated if the radiation dose is not excessing, or a number of studies involving various organs could be conducted simultaneously by administering one or more tracer materials and using multiple source-detector assemblies.

2.6.2 Radioisotope Scanning

Medical radioisotope scanning has developed into an important diagnostic technique. Through the delineation of tracer material distribution in a biological system, it is possible to determine organ structure *in vivo* from a two-dimensional scan made with an external gamma-ray detector. Some examples of organs that are examined by scanning and the radiopharmaceuticals frequently used are presented in Table 2-6 (Ref. 45). This list is continually expanding with the major emphasis in radiopharmaceuticals being placed on medium energy isotopes with short half-lives.

Two basic constraints are imposed, in conventional radioisotope scanning, on the concentration of radioactive material that can be used to scan a given organ with a particular scanning device. First, to obtain a

TABLE 2-6

GAMMA-RAY EMITTING RADIOPHARMACEUTICALS
USED FOR SCANNING

Organ	Radiopharmaceutical
Brain	Chlormerodrin - ^{203}Hg
	Chlormerodrin - ^{197}Hg
	Pertechnetate - $^{99\text{m}}\text{Tc}$
	Serum albumin - ^{131}I
Bone	Strontium nitrate - ^{85}Sr
Kidney	Chlormerodrin - ^{203}Hg
	Chlormerodrin - ^{197}Hg
Liver	Rose bengal - ^{131}I
	Colloidal gold - ^{198}Au
	Aggregated albumin - ^{131}I
	Technetium sulfide - $^{99\text{m}}\text{Tc}$
Lung	Macro-aggregated serum albumin - ^{131}I
	Macro-aggregated serum albumin - ^{51}Cr
Pancreas	Selenomethionine - ^{75}Se
Placenta	Serum albumin - $^{99\text{m}}\text{Tc}$
	Serum albumin - ^{131}I

TABLE 2-6 (CONT.)

Pericardial effusion	Cholografin - ^{131}I
	Serum albumin - $^{99\text{m}}\text{Tc}$
Spleen	Heated red cells - ^{51}Cr
	BMHP - ^{197}Hg
Thyroid	Sodium iodide - ^{131}I
	Sodium iodide - ^{125}I

statistically acceptable representation of the tracer element distribution in a reasonable period of time, the concentration of radioactive material in the organ must be high. Second, the maximum permissible concentration is limited by the radiation absorbed dose which depends on the physical and physiological properties of the radiopharmaceutical being used. Thus, in a fixed scanning time, one can obtain a high resolution scan of a small area or a low resolution scan of a somewhat larger area. It is entirely possible that this situation can be improved in some cases through the use of fluorescent X-rays emitted by high-Z tracer materials.

In theory, the advantages that can be realized by using fluorescent X-rays for medical scanning include those described above for dynamic function studies. For example, by using source collimation, the primary X-ray beam can be confined to the region of the biological system being "viewed" by the detector. The radiation dose to the biological system is limited to the minimum level required to record a statistically acceptable fluorescent X-ray count from each resolution element of the scan in this manner. The time available to complete a scan will therefore not be a primary consideration if the primary X-ray beam has sufficient intensity. Or, stated another way, for a fixed resolution and statistical accuracy, the radiation absorbed dose is independent of the scanning speed and the total scanning time. Since the radiation dose is confined to the immediate vicinity of the scan, a number of organs could be examined in sequence if the dose per scan is not excessive.

Proper alignment of the primary X-ray beam and detector collimator can also minimize the interference resulting from the accumulation of tracer material in adjacent tissue.

Another advantage might be realized if the source-detector geometry is such that horizontal resolution is determined by the diameter of the primary X-ray beam (see Figure 2-4). The resolution element size in this case, can be decreased by source collimation until the radiation dose, which varies as the inverse square of resolution for a given statistical accuracy, increases to the maximum permissible level. This is an approximation since the area of the primary X-ray beam will increase with

depth of penetration in the biological system as the result of Compton and coherent scattering. However, the effective beam broadening can be minimized by using a primary X-ray energy that just exceeds the K-absorption edge energy of the tracer element. Many of the Compton scattered photons will then have energies that are too low to excite tracer element K-series fluorescent X-rays.

One limitation of using fluorescent X-rays for organ scanning is the inability to delineate small defects near the back surface of a thick organ. A similar limitation, resulting from attenuation, is also encountered in radioisotope scanning when low energy X- and gamma ray emitters are used. However, since the local rate of fluorescent X-ray production is determined by the intensity of the primary X-ray beam, a unique scheme can be employed to produce a concentration sensitivity that is independent of depth as illustrated in Figure 2-23. Here, the primary X-ray beam intensity is graduated to create a fluorescent X-ray production rate that increases with depth in the organ to compensate for the attenuation of primary and secondary X-rays in the overburden organ and tissue. This, in practice, could be accomplished by passing a primary X-ray beam of uniform intensity through a tapered wedge filter. It is interesting to speculate about the possibility of developing a technique for making three dimensional scans with the source-detector geometry illustrated in Figure 2-5. This would require a considerable development effort, but the results obtained could improve diagnostic procedures.

2.7 PRIMARY RADIATION SOURCE CONSIDERATIONS

The selection of a suitable X-ray source for high-Z tracer element excitation will depend on the following factors:

1. Type of investigation being conducted
 - a. dynamic function study
 - b. scan
2. Permissible radiation dose
3. Tracer element atomic number
4. Tracer element concentration

5. X-ray detector characteristics
 - a. size
 - b. efficiency
 - c. energy resolution
 - d. resolving time
6. Source-detector geometry
7. Organ depth
8. Organ thickness
9. Time available for the investigation

The most important consideration for any in vivo study involving the use of radiation is the dose that must be delivered to the biological system to obtain the required information. It is mandatory that the primary X-ray source be selected with this point in mind.

It is apparent, from the calculations presented in preceding sections, that if the region of the biological system being examined is not too deep (less than 8 centimeters for iodine), the primary X-ray energy should just exceed the K-absorption edge energy of the high-Z tracer element to obtain the maximum fluorescent X-ray count for a given surface dose. For deeper regions, the excitation energy should be increased somewhat to compensate for the attenuation of primary X-rays in overburden tissue.

Another consideration in selecting a suitable primary X-ray source is the energy distribution of scattered radiation that will be seen by the detector. The energy of single Compton scattered primary X-ray can be determined from Equation 2-24. However, primary X-rays that are coherently scattered as well as those that undergo multiple Compton diffusions will also reach the detector. Since background radiation can limit concentration sensitivity, it is important to select a primary X-ray energy and source-detector geometry that will result in a low scattered radiation intensity near the tracer element fluorescent X-ray energy.

For a monoenergetic excitation source, coherently scattered primary X-rays will always be more energetic than the tracer element K-series fluorescent X-rays. Compton scattered primary X-rays, on the other hand, will cover a wide energy range. The tracer element atomic number and scattering angle can be adjusted so that all Compton scattered photons will have lower energies than the tracer element K X-rays under certain conditions. This can be accomplished, for example, if the tracer element atomic number is greater than about 58 and the scattering angle is between 150 and 180 degrees. However, for lower tracer element atomic numbers or smaller scattering angles, some Compton scattered photons will be sufficiently energetic to create unwanted background counts in the fluorescent X-ray detector. This background interference can be minimized by selecting the primary X-ray energy and source-detector geometry so that the single Compton scattered photon and tracer element K-series X-ray energies can be resolved by the detector.

When the primary X-ray beam is mixed or continuous, scattered radiation will always be a major problem and will place a lower limit on the tracer element concentration that can be used.

The intensity of the primary X-ray source will determine the fluorescent X-ray intensity at the detector. It is therefore important for dynamic function studies to select a source with sufficient intensity to provide a statistically acceptable fluorescent X-ray count in a sampling period that is short compared to the accumulation and release constants of the tracer element in the region being examined. An analysis of radioactive tracer studies indicates that the sampling period could vary from a few seconds up to several minutes.

The selection of a primary X-ray source for a medical scanning system must be based on all the considerations outlined above. It should be noted however, that at conventional scanning speeds (20 to 400 cm/min) a high source intensity is required since the effective sampling time is very short. To obtain a concentration sensitivity that is essentially independent of depth for the examination of thick organs, it will be necessary to filter the primary X-ray beam as indicated in Figure 2-23. Any filtering of this type will necessitate the use of a more intense primary X-ray source.

The maximum source intensity that can be used will depend on the area, efficiency, and resolving time of the fluorescent X-ray detector as well as the radiation dose delivered to the biological system.

Based on these general source selection guide lines, we can now compare several primary radiation sources that could be used for this application. Some example sources are listed in Table 2-7 with the principal radiations emitted. Of these four types of sources, only gamma ray emitters and X-ray machines with secondary radiator targets can supply the nearly monoenergetic excitation beams required to obtain a maximum signal-to-background ratio at the detector, and minimize the radiation dose delivered to the biological system.

Unfortunately, suitable gamma emitting radioisotopes are not presently available for many of the high-Z tracer elements that could be used for in vivo studies. However, under experimental conditions for which gamma emitting radioisotopes of suitable energy and intensity can be obtained at a reasonable cost, they offer many unique advantages. In addition to the above advantages, sources of this type are easily shielded and collimated and do not require elaborate high voltage power supplies and control systems.

The most versatile excitation source is obtained by fitting a conventional X-ray machine with interchangeable external secondary radiator targets. The output from this source consists primarily of the radiator element K-series X-rays with a very weak continuous spectrum background (Ref. 20). In most cases, a secondary radiator with an atomic number slightly higher than that of the tracer element can be obtained at a reasonable cost. This source can be used to excite a wide range of tracer elements by simply changing the secondary radiator and the X-ray intensity is readily adjustable.

The secondary radiator can be mounted inside the X-ray tube envelope to obtain a somewhat higher beam intensity (Ref. 21). However, the inability to rapidly change the secondary radiator limits the usefulness of this configuration.

While mixed excitation sources do not provide all of the advantages of monoenergetic sources for this application, they do have relatively high intensities and can provide fairly efficient fluorescent X-ray excitation. In fact, X-ray machines are used extensively as excitation sources for X-ray fluorescence analysis and special beta excited X-ray sources have also been developed for this purpose (Ref. 22 -32).

TABLE 2-7

X-RAY AND GAMMA-RAY SOURCES

Source Type	Typical Isotopes	Principal Radiations Emitted
Gamma Emitter	Cd^{109}	88 kev γ -ray
	I^{125}	35 kev γ -ray Te K X-ray
	Am^{241}	59.6 kev γ -ray Am and Np L X-rays
Beta Emitter with Conversion Target	Pm^{147}	10-50 kev bremsstrahlung
	$\text{Sr}^{90} + \text{Y}^{90}$	70-150 kev bremsstrahlung Target K X-rays
	Kr^{85}	30-80 kev bremsstrahlung Target K X-rays
X-ray Machine		10-300 kev bremsstrahlung Target K X-rays
X-ray Machine with Secondary Radiator Target		Secondary Radiator K X-rays

Beta excited X-ray sources are attractive for this application because β -emitting radioisotopes are relatively inexpensive, the X-ray intensity is very stable, no additional excitation equipment is required, and the beta emitter and target material can be selected to provide a high X-ray intensity at an energy that just exceeds the tracer element K-absorption edge. Filters can also be employed to suppress the low energy region of the continuous X-ray spectrum and minimize the radiation absorbed dose.

These same considerations apply to X-ray machine sources but the target selection is limited to a few elements in commercially available sealed X-ray tubes.

Using demountable X-ray tubes, however, the anode material can be chosen to provide a suitable excitation source for many of the tracer elements that might be considered for this application.

2.8 RADIATION DETECTOR CONSIDERATIONS

As with the selection of the primary X-ray source, a number of factors will influence the selection of the fluorescent X-ray detector. These include:

1. Type of investigation being conducted
 - a. dynamic function study
 - b. scan
2. Tracer element atomic number
3. Tracer element concentration
4. Excitation source characteristics
 - a. energy spectrum
 - b. intensity
5. Source - detector geometry
6. Time available for experiment

The detector parameters of interest for this application are size, detection efficiency, energy resolution, and resolving time.

Detector size is important because a large detection solid angle will provide a high fluorescent X-ray count per unit surface dose. The maximum detector size will depend on the efficiency and resolving time of the detector, as well as physical limitation imposed by the experimental geometry.

The efficiency of the radiation detector should be nearly 100 percent at the tracer element K X-ray energy to ensure that the available fluorescent X-ray intensity is fully utilized. At other energies, the detection efficiency need not, and preferably should not be very high to provide some discrimination against background and scattered radiation.

Since the fluorescent X-rays to be measured are accompanied by scattered primary radiation, the detector must have good energy resolution to provide a maximum signal-to-background detection ratio. Some improvement in energy dispersion can be obtained by using a detector filter that has a K-absorption edge that just exceeds the tracer element K X-ray energy and in many instances, balanced filters (Ref. 18, 46, 47) can be used for energy selection.

To accurately determine the concentration of a high-Z tracer element in a biological system in a short period of time, a high intensity excitation source and a large area fluorescent X-ray detector must be used. It is important therefore to select a radiation detector with a short resolving time to minimize counting losses which would reduce concentration sensitivity.

The radiation detectors that should be considered for this application include those that have received wide spread use in fluorescent X-ray analysis; namely, gas proportional, scintillation, and semiconductor detectors.

The high-Z tracer elements that would be most useful for in vivo studies have K X-ray energies of about 15 to 75 keV. This will restrict the use of gas proportional detectors for this application because of the low detection efficiencies at these energies. Space charge effects which result in a decreased output pulse height can also occur at high X-ray intensities. In spite of these limitations, gas proportional counters have very good resolution (Ref. 48) (6 - 12 percent FWHM) over the energy

range of interest and can be used for some in vivo studies if suitable precautions are observed.

Scintillation detectors, usually with NAI(Tl) crystals, have been used for several years in X-ray fluorescence analysis with excellent results. Crystals with a wide variety of sizes and shapes are available and a modest crystal thickness will absorb essentially all of the fluorescent X-rays that strike the detector. These detectors have fairly good resolution (Ref. 49) (\approx 15 to 30 percent FWHM) from 15 to 75 keV and, with suitable electronics can be used at counting rates in excess of 10^5 counts per second. In addition to these advantages, scintillation detectors will operate satisfactorily at room temperature.

Semiconductor detectors, both silicon and germanium, have recently been applied to the measurement of fluorescent X-rays and X-ray spectrometers using these detectors are commercially available. Resolutions of less than 1.4 percent FWHM have been reported (Ref. 50) for the energy range from 15 to 75 keV and very high counting rates ($> 10^5$ cps) can be recorded with suitable electronics. These detectors must be operated at low temperatures to realize their maximum performance but this is not a restrictive requirement for laboratory applications. An important consideration is the fact that large area semiconductor detectors are not commercially available at the present time. Continued research in fabrication technology and new semiconductor materials could eliminate this restriction in the future but, until this occurs, the large solid angle detection geometry required to minimize the dose to the biological system can only be achieved by using an array of these devices.

Filmed as received
without page(s) 92.

UNIVERSITY MICROFILMS.

SECTION 3

EXPERIMENTAL VERIFICATION

The theoretical equations and example calculations presented in Section 2 of this report indicate that externally excited high-Z tracer element fluorescent X-rays have potential use for in vivo biological and medical studies. To verify these theoretical equations, and subsequently this hypothesis, a number of experiments must be conducted to determine the concentration sensitivity and resolution that can be obtained as a function of the radiation dose delivered to the biological system. Obviously, many of the preliminary experiments can be conducted with biological "phantoms" using standard laboratory equipment. However, the full potential of this technique must ultimately be established by actually performing in vivo biological studies with an instrumentation system that is designed specifically for this application.

To provide experimental verification of some of the concepts and theoretical equations developed in Section 2, a number of preliminary experiments were performed using specially designed biological phantoms and the equipment available in this laboratory. Specifically, the fluorescent X-ray intensity per unit surface dose rate was measured as a function of excitation beam energy, tracer element concentration in the organ of interest, and organ depth for a given tracer element atomic number and organ thickness. Additional experiments were conducted to investigate the possibility of using excitation beam collimation in defining horizontal resolution for the delineation of tracer element concentration distribution.

One of the primary considerations in deciding on the tracer element for these investigations was the desirability of using an element for which extensive clinical data had been obtained from other types of diagnostic procedures. It was also important to select a high atomic number element that could be administered in fairly large quantities without producing harmful effects. As mentioned previously, iodine compounds have been used extensively in radioisotope scanning and for radiological diagnostic purposes. In addition, the normal thyroid gland contains a high concentration of iodine, and abnormal thyroid iodine concentrations and concentration distributions are associated with certain disease states. For these reasons, iodine was chosen as the tracer element for these preliminary experiments.

3.1 EXPERIMENTAL EQUIPMENT

3.1.1 Excitation Source

The excitation source for the experiments described in this report was a portable radiographic and fluoroscopic X-ray machine manufactured by the Picker X-Ray Corporation (Cat. No. F-12). A photograph of the assembled X-ray unit is shown in Figure 3-1. The table and tube stand were used to support and align the X-ray tube head, biological phantom, and detector assembly.

The X-ray tube has a tungsten target and the inherent filtration of the tube window is 0.5 mm aluminum equivalent. A cone mounting assembly attached to the X-ray tube head provides a fixed filtration of 0.5 mm aluminum equivalent and contains a slide for adding additional filters.

Controls for the X-ray machine include a mode change-over switch (radiography-fluoroscopy), a KV selector switch, and a filament current control potentiometer. Meters on the control console monitor the X-ray tube voltage and current.

With the mode switch in the radiography position, the X-ray tube current is fixed at 15 MA and the tube voltage can be set at approximately 5-KV intervals from 40 to 85 KV. For fluoroscopy, the X-ray tube current is variable from 1 to 5 MA and the tube voltage can be adjusted in discrete steps (approximately 5 KV/step) from about 50 to 85 KV.

Unfortunately, this X-ray machine does not have many of the features that would be desirable for the proposed application. The X-ray tube voltage and current are not well regulated and were found to fluctuate with line voltage and X-ray tube temperature. It was also noted that an increase in tube current was accompanied by a slight decrease in tube voltage for a fixed KV setting. The influence of these factors can be minimized by taking suitable precautions, such as letting the X-ray tube temperature stabilize before starting the experiment and making the necessary measurements at a fixed current. However, it is apparent from the data presented in this thesis as well as the published literature on X-ray fluorescence analysis that a well regulated X-ray source is required to obtain satisfactory results for low tracer element concentrations.

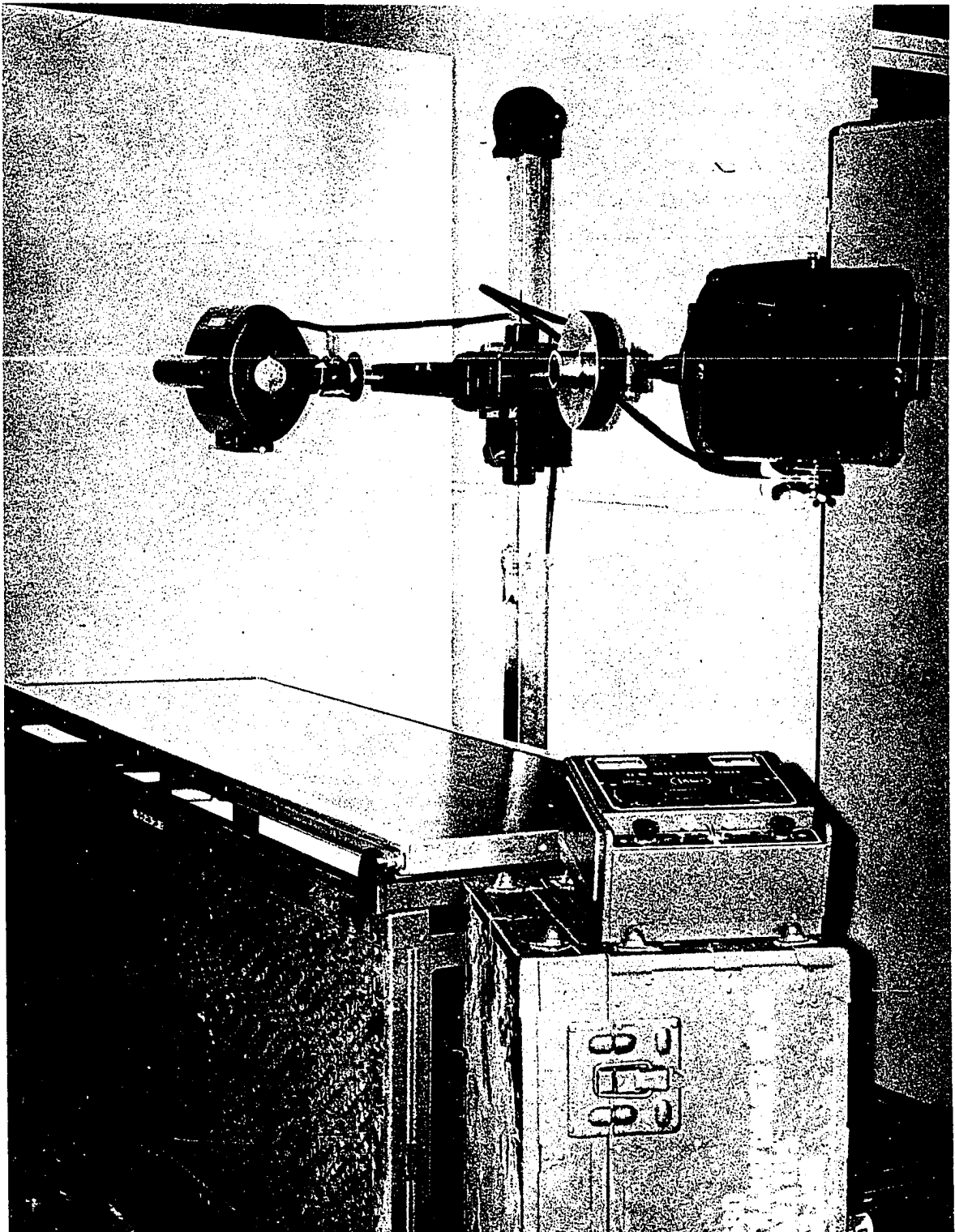


Figure 3-1 Photograph of Assembled X-Ray Machine

For these experiments, the X-ray machine was operated at a maximum power level of 78 KV-3MA with a total beam filtration of 1.75 mm aluminum equivalent. The selection of these operating conditions was based on X-ray tube heating considerations and the data presented in Figure 3-2. Here, it has been assumed that the X-ray tube voltage is 78 KV and that an effective electron energy, $E_{e, \text{eff}}$, for half-wave rectification is:

$$E_{e, \text{eff}} \approx V_{\text{rms}} \approx 0.7V$$

where V_{rms} is the rms voltage for the conducting half-cycle and V is the maximum tube voltage, 78 KV. This is only a rough approximation of course, since the true electron energy will vary from $E_e = 0$ to $E_e = V$ during each cycle.

To define the cross-sectional area of the primary X-ray beam, two 0.093-in. thick lead annular rings spaced 1.6 in. apart were mounted in a lead-lined brass housing that attached to the X-ray tube head in place of the cone.

3.1.2 Biological Phantoms

Three biological phantoms were constructed for investigating concentration sensitivity and defect localization. Figure 3-3 is a photograph of the phantom used for the concentration sensitivity studies.

Tissue simulation was provided by 15.2 x 15.2 x 0.635 cm lucite sheets stacked on aluminum support rods. Six of these sheets had match-drilled center holes to accept small polyethylene containers that were used for organ simulation. "Organ depth" variations were accomplished by simply rearranging the stacking order of the lucite sheets.

The organ simulation containers were cylindrical with an inside diameter of 1.65 cm and length of 3.3 cm. These were filled with potassium iodide solutions with iodine concentrations ranging from 783 to 100,000 ppm. Each container was completely filled and covered with a layer of parafilm "M" before capping to eliminate air bubbles and prevent evaporation.

$E_{e, \text{eff}} = 55 \text{ Kev}$

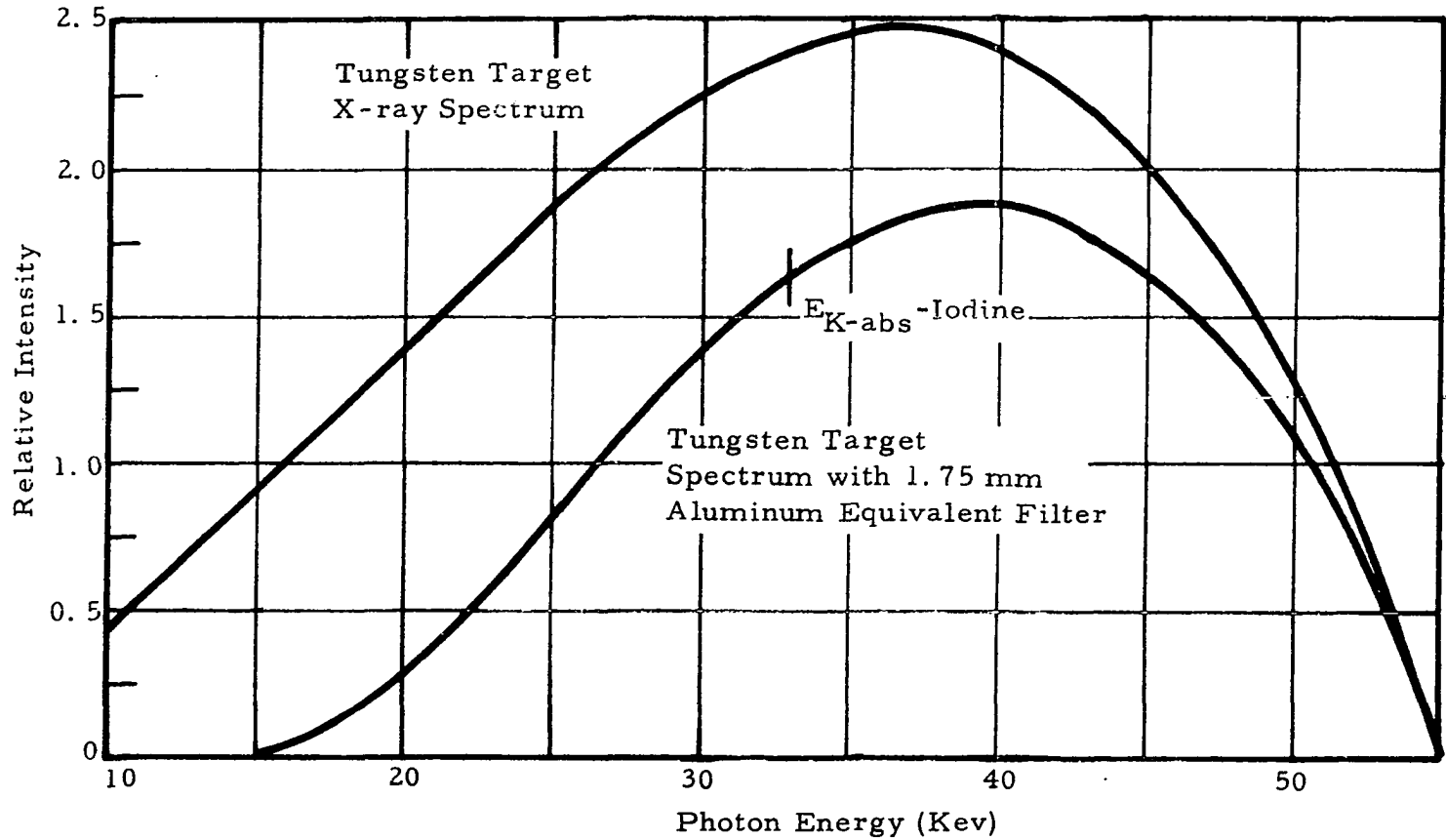


Figure 3-2 Attenuation of Tungsten Target Continuous Spectrum

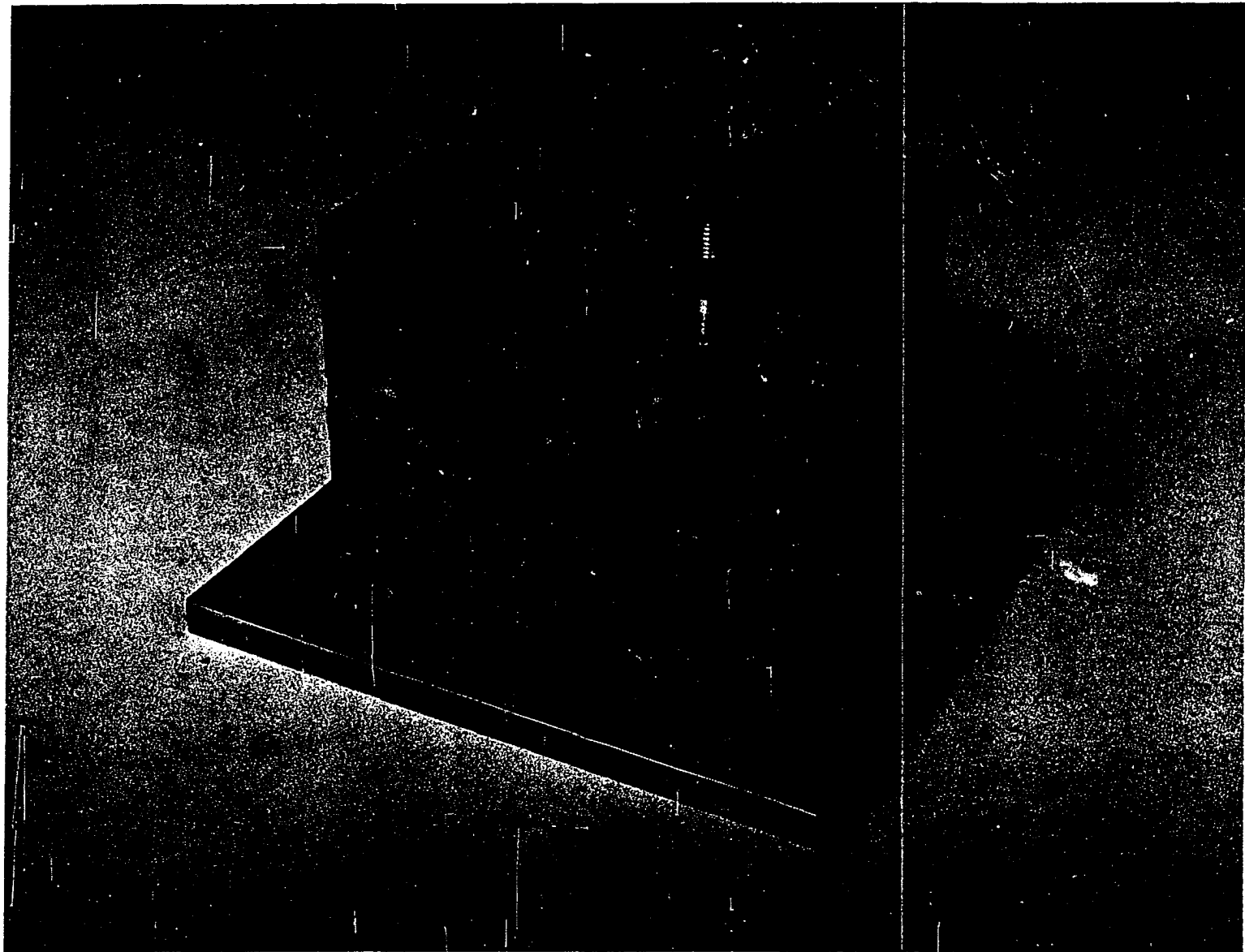


Figure 3-3 Photograph of Biological Phantom Used for Concentration Sensitivity Studies

Construction of the "hot spot" defect phantom is illustrated in Figure 3-4. Here, four holes with diameters ranging from 0.10 to 0.33 cm were drilled radially into the edge of a 0.635-cm thick lucite sheet on the midline. Each hole was then filled with an iodine solution of 25,000 ppm I and sealed with lucite cement.

"Cold spot" defect simulation was provided by the phantom illustrated in Figure 3-5. The defect is a rectangular lucite rod mounted at one end of a cylindrical plastic container filled with a 25,000 ppm I solution.

Several 0.635-cm thick lucite sheets were used to establish defect depth.

3.1.3 X-Ray Detector

X-ray intensity was measured with a scintillation detector mounted in a multihole focused collimator which also shielded the detector from direct excitation source radiation.

The detector was fabricated by coupling a Harshaw type 6D2-1.75 in. dia. x 0.5 in. NaI (Tl) crystal to an RCA 6655A photomultiplier tube having a base-mounted TMC Model DS-11 preamplifier. This assembly was placed in a modified Tracerlab, Inc., Model P-20 D scintillation detector housing. Bias for the photomultiplier tube and preamplifier was provided by a Fluke Model 412B high voltage power supply.

The multihole focused collimator was made of steel and contained nineteen 0.063-in. diameter straight bore holes focused at 10.5 in. as illustrated in Figure 3-6. To a first approximation, the lateral response to a point source located at the collimator focal plane can be determined from the equation (Ref. 51).

$$\text{Relative Response} = 1 - \frac{2}{\pi} \sin^{-1} \frac{r}{R_r} - \frac{2r}{\pi R_r} \sqrt{1 - \left(\frac{r}{R_r}\right)^2} \quad (3-1)$$

where:

r = lateral displacement of point source

R_r = resolution radius.

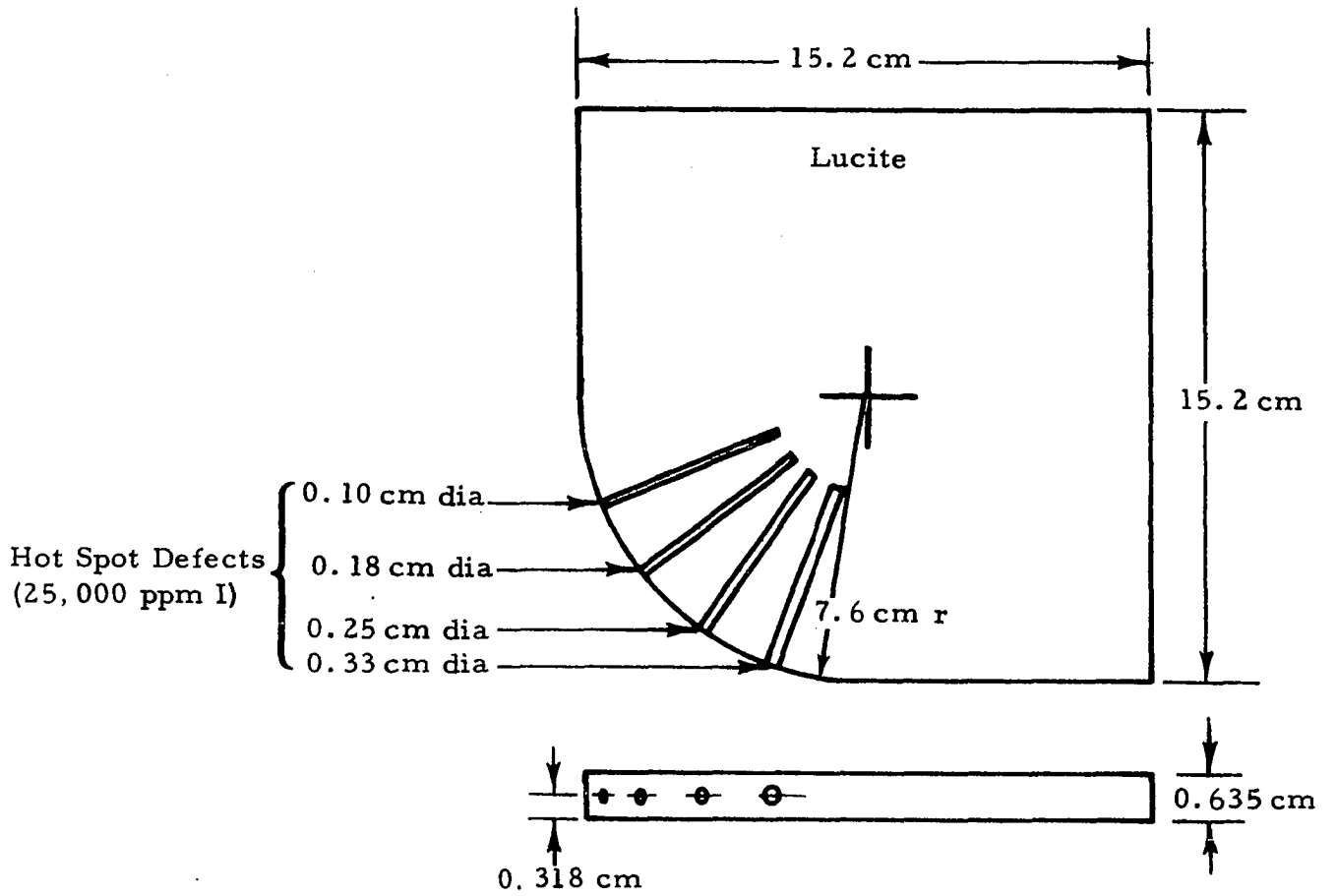


Figure 3-4 "Hot Spot" Defect Phantom Construction

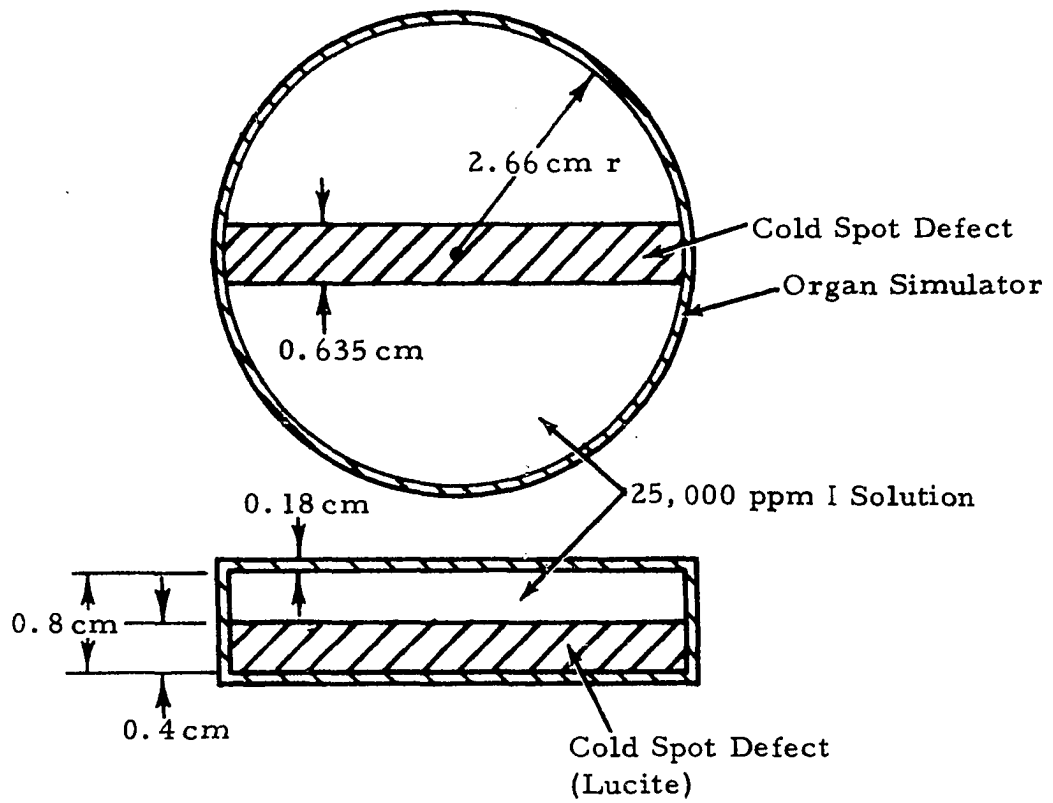


Figure 3-5 "Cold Spot" Defect Phantom Construction

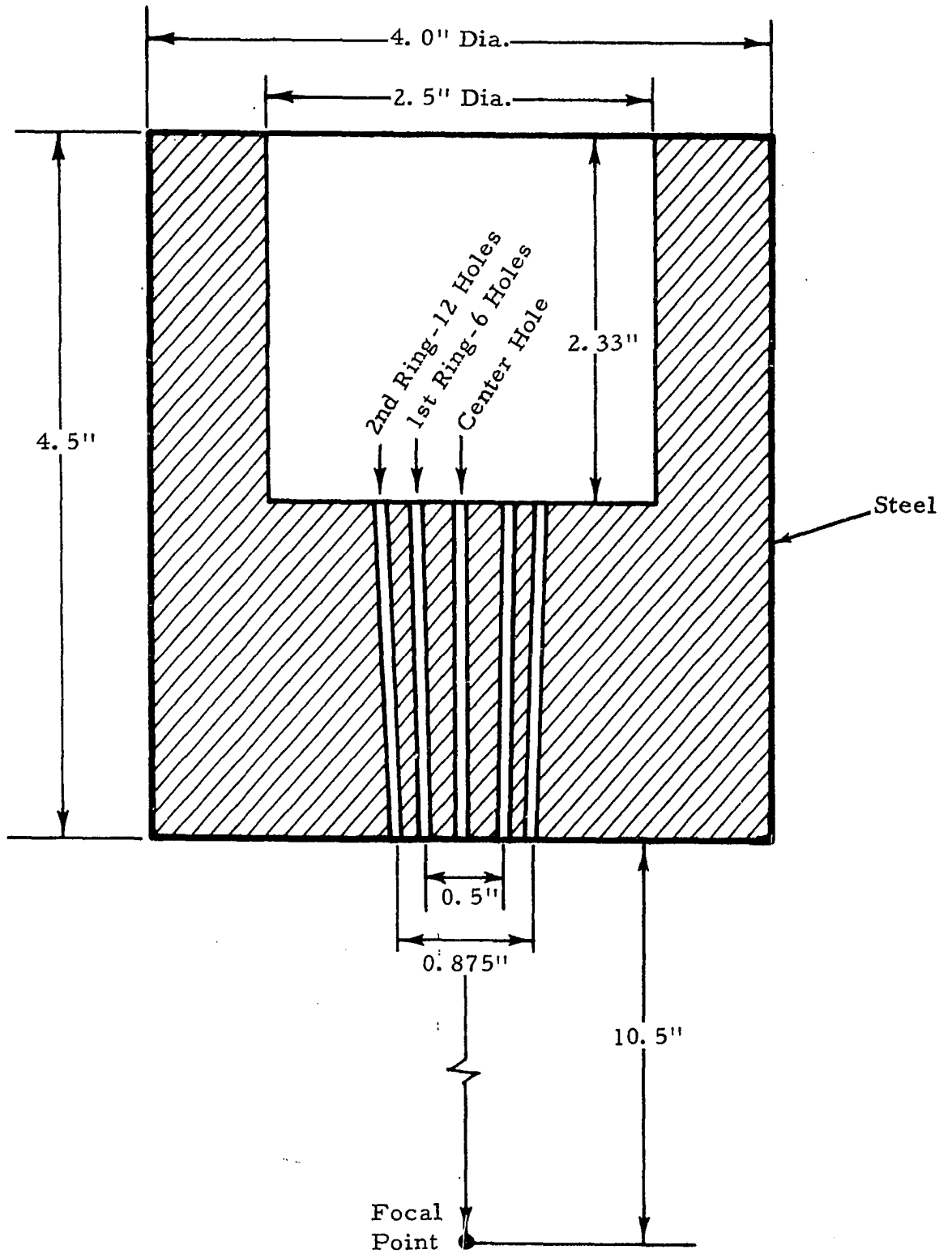


Figure 3-6 Construction of Multihole Focused Collimator

Relative response values calculated from Equation 3-1 for the detector collimator shown in Figure 3-6 are presented graphically in Figure 3-7. At the focal plane, the 50% response width is 0.3 in. and this value will remain nearly constant for vertical displacements of ± 1 in.

3.1.4 Scanner

Single trace "hot spot" and "cold spot" defect scans were made with a modified Atomic Accessories, Inc., Model RSC-5A chromatogram scanner. Since the scanner originally had a variable speed rotating drum synchronized through a gear train to drive a strip chart recorder, the only modification required was the attachment of a phantom-mounting platform to the rotating drum spindle. This arrangement permitted curvilinear scanning of the defect phantoms while the excitation source-detector assembly remained in a fixed position. Normally, the source-detector assembly would scan over a stationary biological system. With the equipment used for this experimental program, however such an arrangement was impractical and not really necessary since the results in either case will be the same.

Gear ratios for the motor drive can be changed to vary the scanning speed at the chromatogram strip mounting radius in fixed increments from 0.0318 to 30.5 cm/min, and other scanning speeds can be obtained by selecting the proper radius and gear combination.

Figure 3-8 is a photograph of the modified chromatogram scanner used for these experiments.

3.1.5 Signal Processing and Readout

Voltage signals from the preamplifier were fed into a Technical Measurements Corporation (TMC) "Gammascopie" Model 101 multichannel analyzer operated in the single channel-fast summation mode. In this mode, input voltage pulses are analyzed without being stored in the memory, and each pulse in the selected energy window generates a +4-V output pulse. These output pulses were processed through an inverting amplifier and counted with a Baird-Atomic Model 134 high speed scaler or a Baird-Atomic Model 432 ratemeter—depending on the type of experiment being conducted.

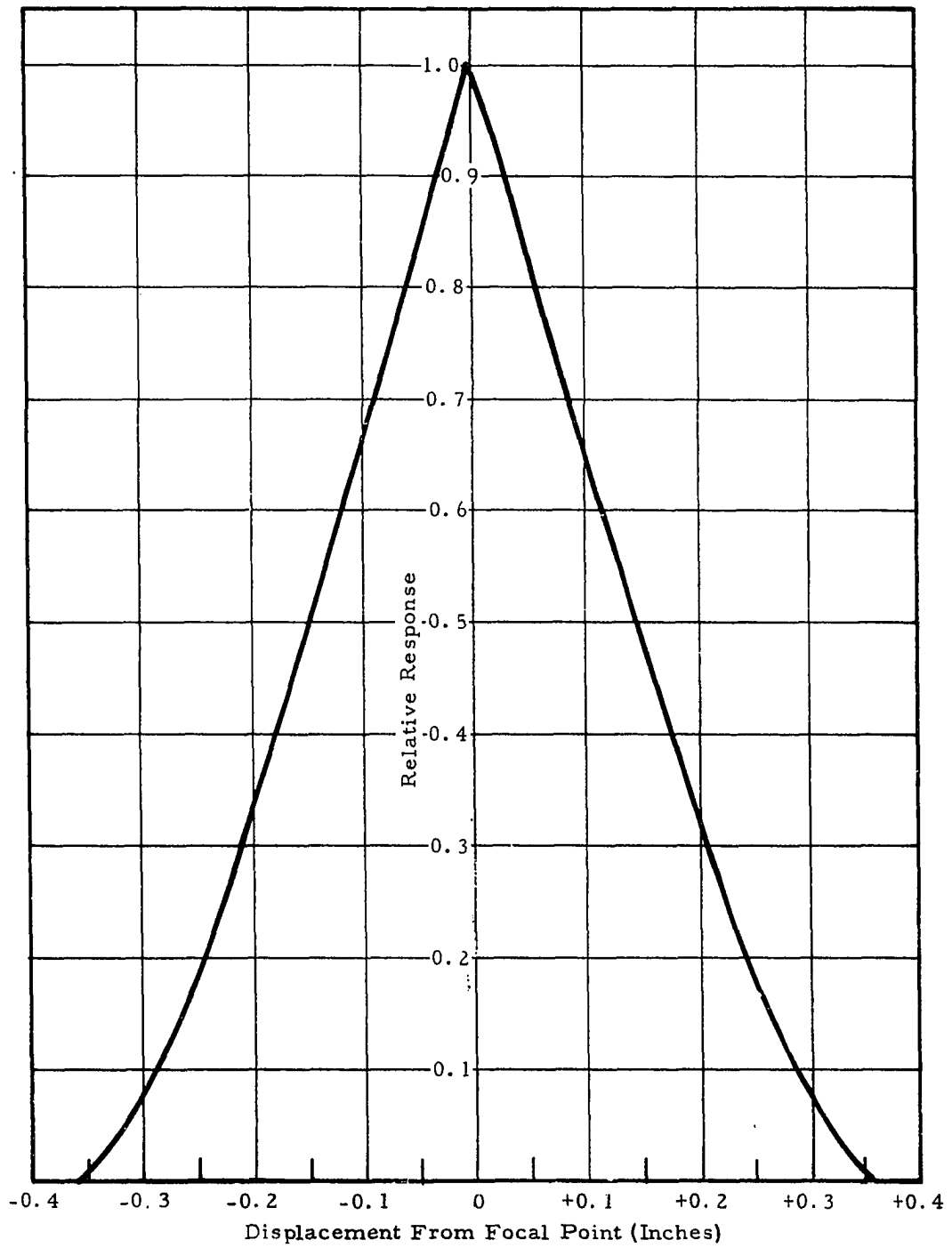


Figure 3-7 Theoretical Point Source Response for Lateral Displacement in Focus Plane

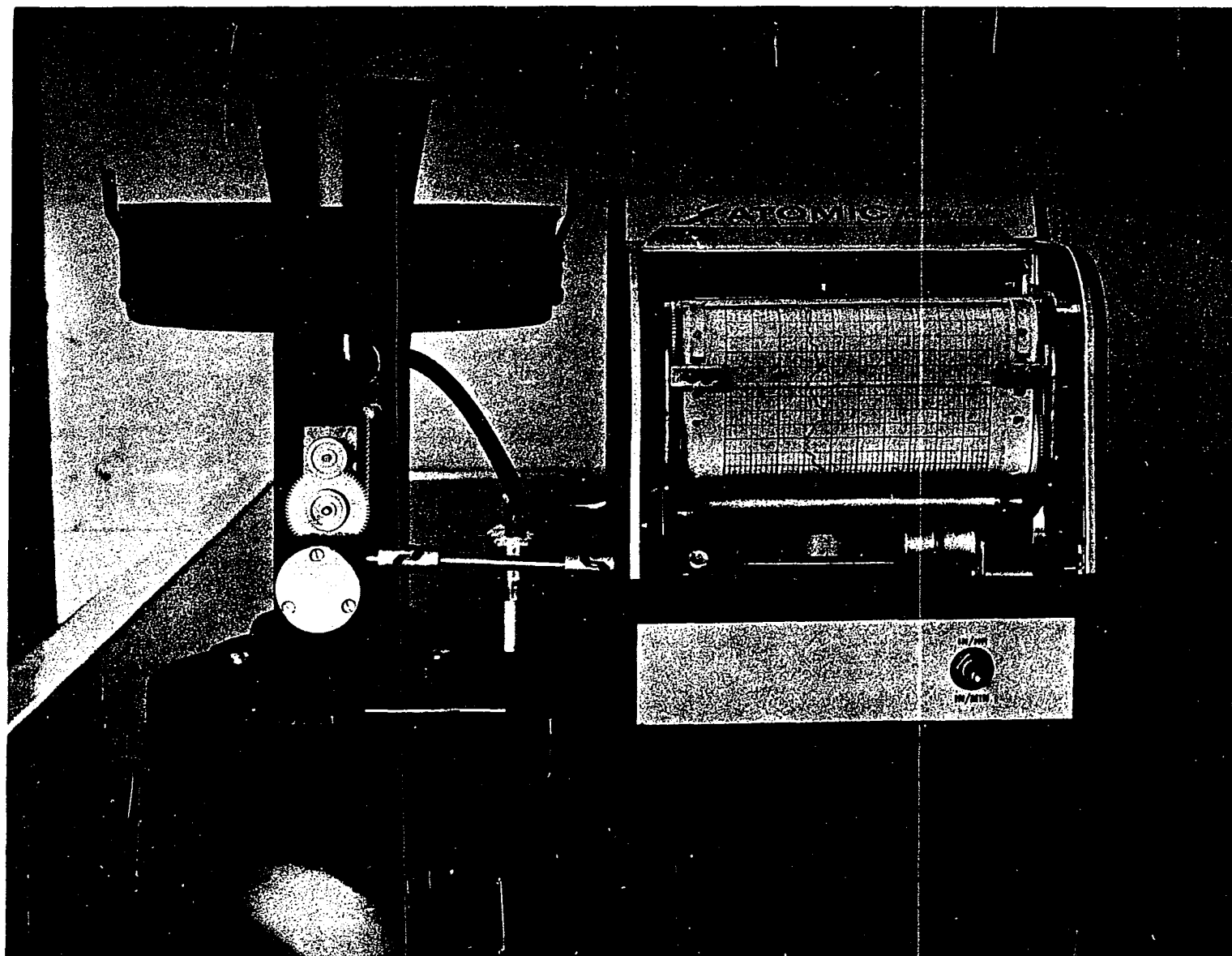


Figure 3-8 Photograph of Modified Chromatogram Scanner

The TMC Gammascopes provides a very rapid and convenient method for determining the intensity under a photopeak, because the single channel window base and width are easily adjusted to bracket the peak. Also, since the pulses are analyzed without storage, the dead time is very low. X-ray intensities measured with the complete detector and electronics system indicated a negligible counting loss for count rates up to 2.5×10^5 cpm.

3.2 EXPERIMENTAL PROCEDURE

3.2.1 Concentration Sensitivity Measurements

Figure 3-9 is a dimensional layout of the source-biological phantom-detector geometry that was used to measure the dependence of fluorescent X-ray intensity on excitation energy, tracer element concentration, and organ depth. A functional block diagram of the complete experimental system is presented in Figure 3-10.

To establish the proper geometry, the X-ray tube head was set for a 60° incidence angle on the horizontal surface of the phantom and positioned vertically so that the distance from the X-ray tube focal spot to the midpoint of the organ simulator (sample) would be 14 in. Source collimators were fabricated to limit the primary X-ray beam dimensions to the cross-sectional area of the sample in an effort to reduce the scattered radiation component from the surrounding lucite. A fluorescent screen was then placed on top of the phantom to locate visually the area being irradiated, and the phantom was moved horizontally to center the sample in the primary X-ray beam.

To align the detector collimator, the detector was replaced by a diffuse light source and light passing through the collimator holes and reflecting from the phantom was used to position the collimator on the vertical axis of the sample. The height of the collimator was adjusted to place the focal plane at the mean depth of the sample.

Various organ depths were simulated by simply rearranging the stacking order of the lucite sheets and raising the phantom with a jack to return the sample to its original position.

Correct single-channel window settings (base and width) on the TMC Gammascopes were selected by first operating the analyzer in the multichannel mode and exposing the scintillation detector to a $0.92 \mu\text{Ci}$ Am^{241} source ($E_\lambda = 59.6 \text{ keV}$). The gain of the amplifier was then adjusted

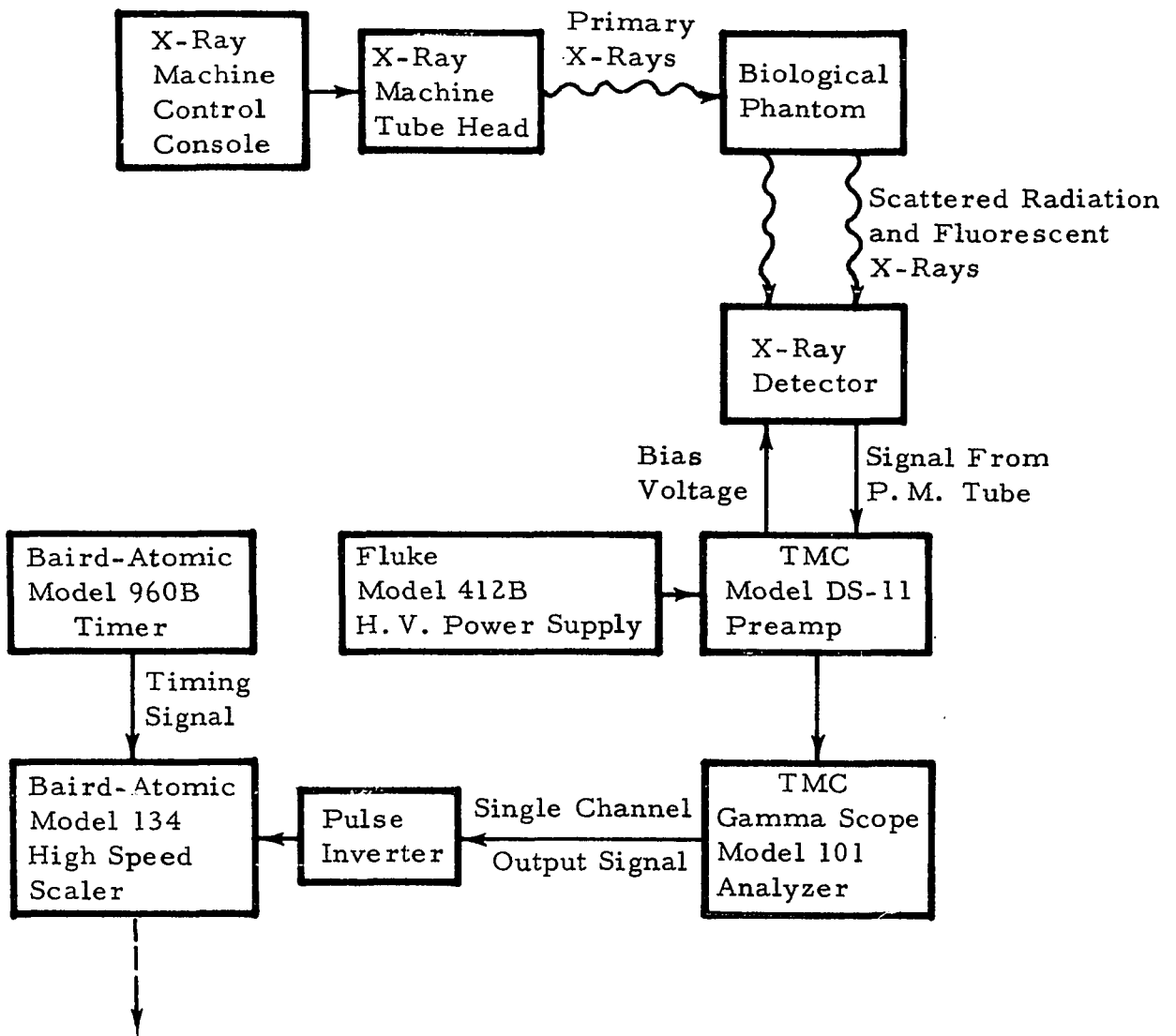


Figure 3-10 Functional Block Diagram of Experimental System for Concentration Sensitivity Measurements

so that channel 60 corresponded to 60 kev (approx 1 kev/channel). With this approximate energy calibration established, a sample containing a high concentration of iodine was placed in the phantom and irradiated by the X-ray machine to accumulate a fluorescent X-ray and scattered radiation spectrum in the analyzer. The scattered radiation component was then subtracted by irradiating a water sample for the same period of time with the analyzer in the subtract mode. With the analyzer display switch in the dynamic display position, the residual iodine K X-ray spectrum was presented on the CRT readout, with the window location being defined by the intensified channels, and the window selector controls were set to bracket the iodine K X-ray peak.

The system was ready for data accumulation after returning the analyzer to the single channel-fast summation mode and connecting the pulse inverter, high speed scaler, and external timer.

Photographs of the assembled experimental system are presented in Figures 3-11 and 3-12. Figure 3-11 shows the experimental area and illustrates the source-biological phantom-detector geometry used for these experiments. The X-ray machine control and data acquisition area shown in Figure 3-12 was separated from the experimental area by a thick wall for radiation safety purposes.

The sequence of events for measuring the dependence of fluorescent X-ray intensity on tracer element concentration and sample depth for a given excitation energy was as follows:

1. A water sample was placed in the phantom and the X-ray controls were set at 78 KV - 3 MA and stabilized for approximately 1 min.
2. Ten 1-min counts of the scattered X-ray intensity in the single-channel window were recorded with the high speed scaler using an external timer.
3. The water sample was then replaced by a sample containing a known concentration of iodine and ten 1-min counts of the scattered X-ray and fluorescent X-ray intensity in the window were recorded.

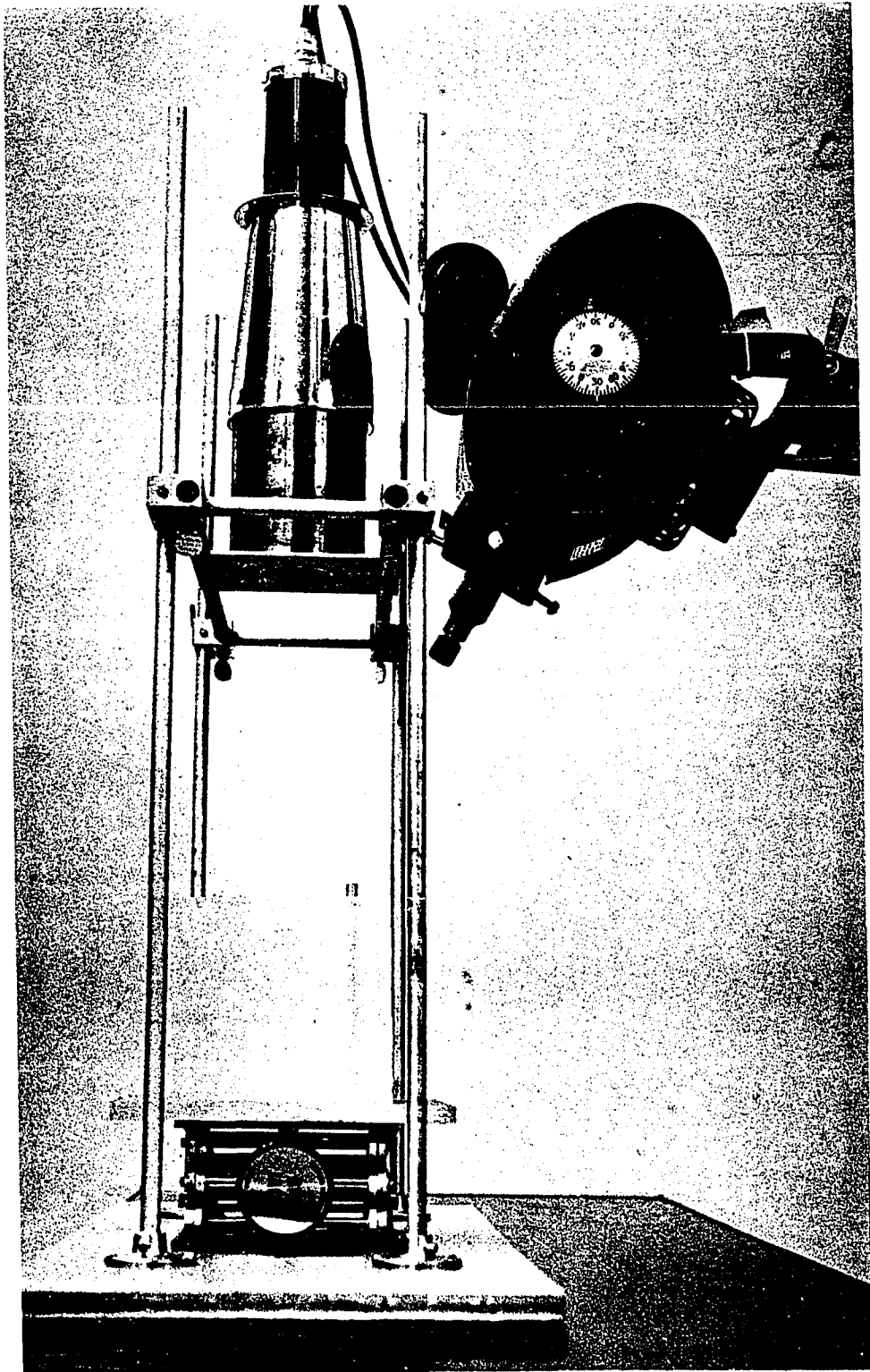


Figure 3-11 Photograph of the Experimental Area for Concentration Sensitivity Measurements

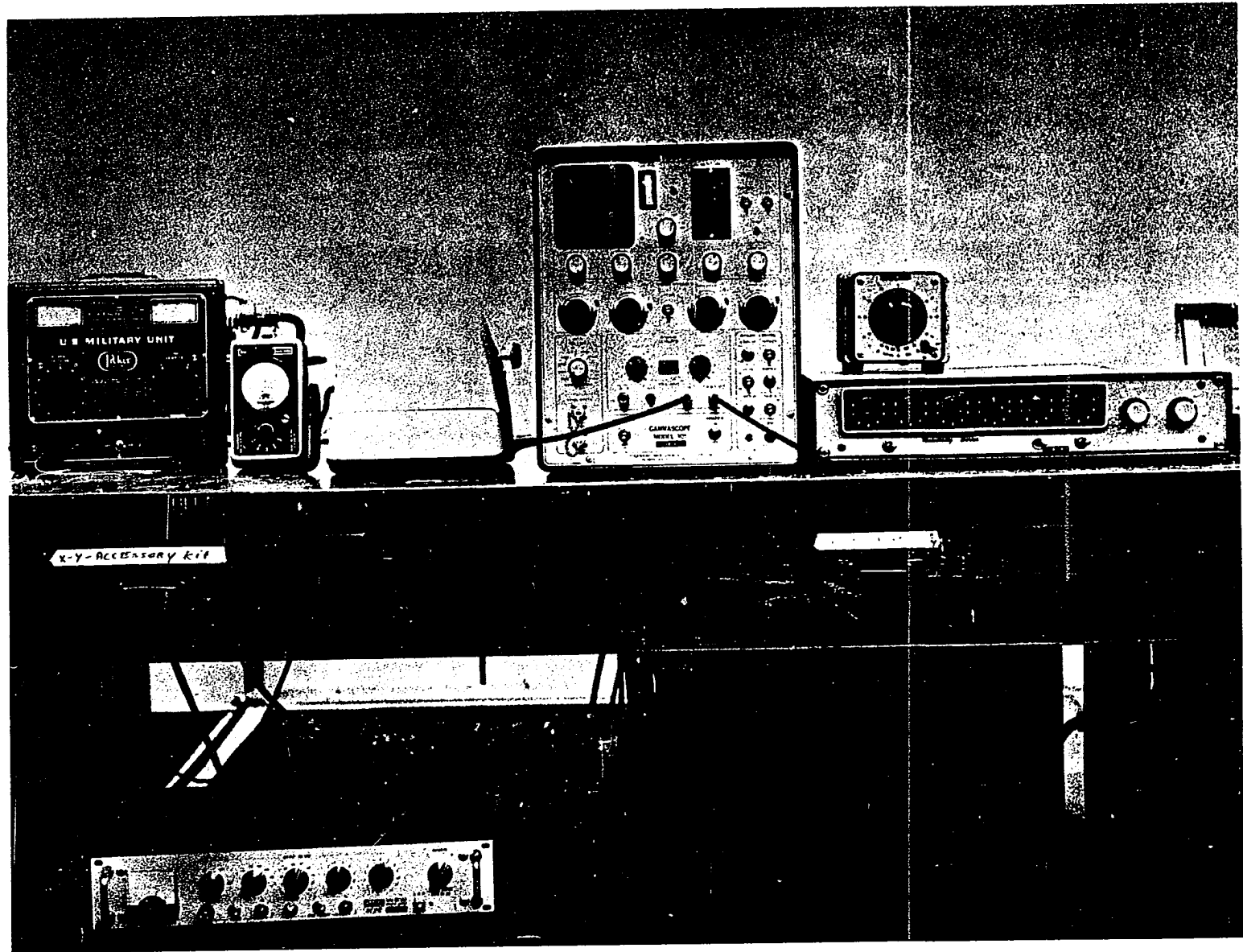


Figure 3-12 Photograph of X-Ray Machine Control and Data Acquisition Area

This procedure was repeated for samples having iodine concentrations that differed by a factor of 2 from 783 to 50,000 ppm at mean sample depths of 1.75, 3.02, 4.29, 5.56, 6.83, and 8.10 cm.

The dependence of fluorescent X-ray intensity on excitation energy (X-ray machine KV setting) for a given tracer element concentration and organ depth was measured as follows:

1. A water sample was placed in the phantom, and the X-ray controls were set at approximately 49 KV-3 MA and stabilized for 1 min.
2. Five 1-min counts of the scattered X-ray intensity in the single-channel window were recorded with the high speed scaler using an external timer.
3. The water sample was then replaced by a sample containing 25,000 ppm I and five 1-min counts of the scattered X-ray and fluorescent X-ray intensity in the window were recorded.

This procedure was repeated for seven KV settings from about 49 to 78 KV at 3 MA for mean sample depths of 1.75, 4.29, and 6.83 cm.

By collecting the data in this manner, the iodine K X-ray intensity could be determined by simply subtracting the water sample count rate from the corresponding iodine sample count rate and multiplying the difference by the appropriate constants.

3.2.2 Defect Localization

The geometry illustrated in Figure 3-13 was used to make a preliminary investigation of "hot spot" and "cold spot" defect localization using fluorescent X-rays. A functional block diagram of the complete system is presented in Figure 3-14.

The diameter of the primary X-ray beam for these experiments was restricted by source collimation to about 3 mm at the defect location. This combination of excitation source and detector collimation uniquely defined the region of the biological phantom under investigation and provided a high signal-to-background intensity ratio at the detector.

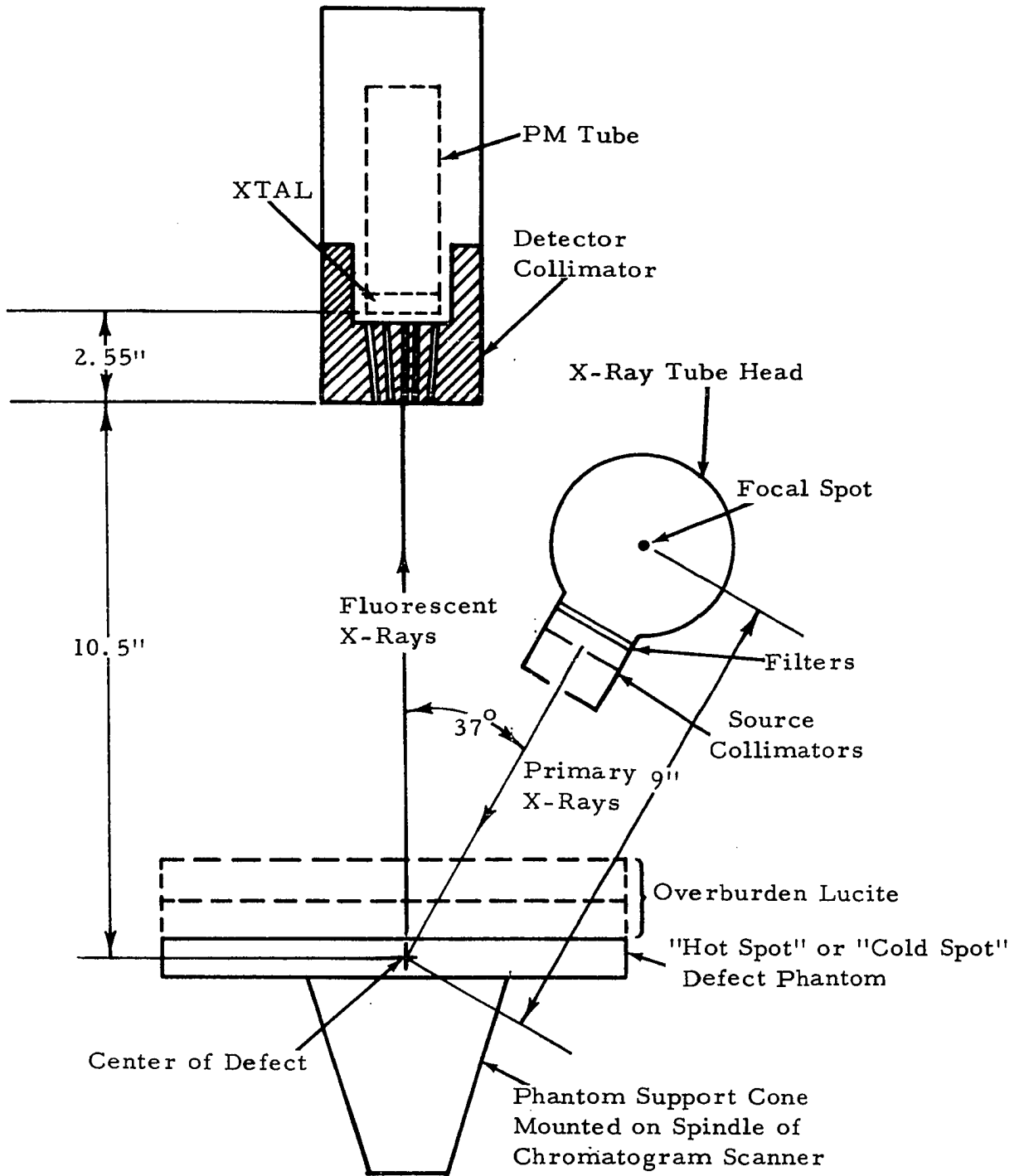


Figure 3-13 Dimensional Layout of Defect Scanning Geometry

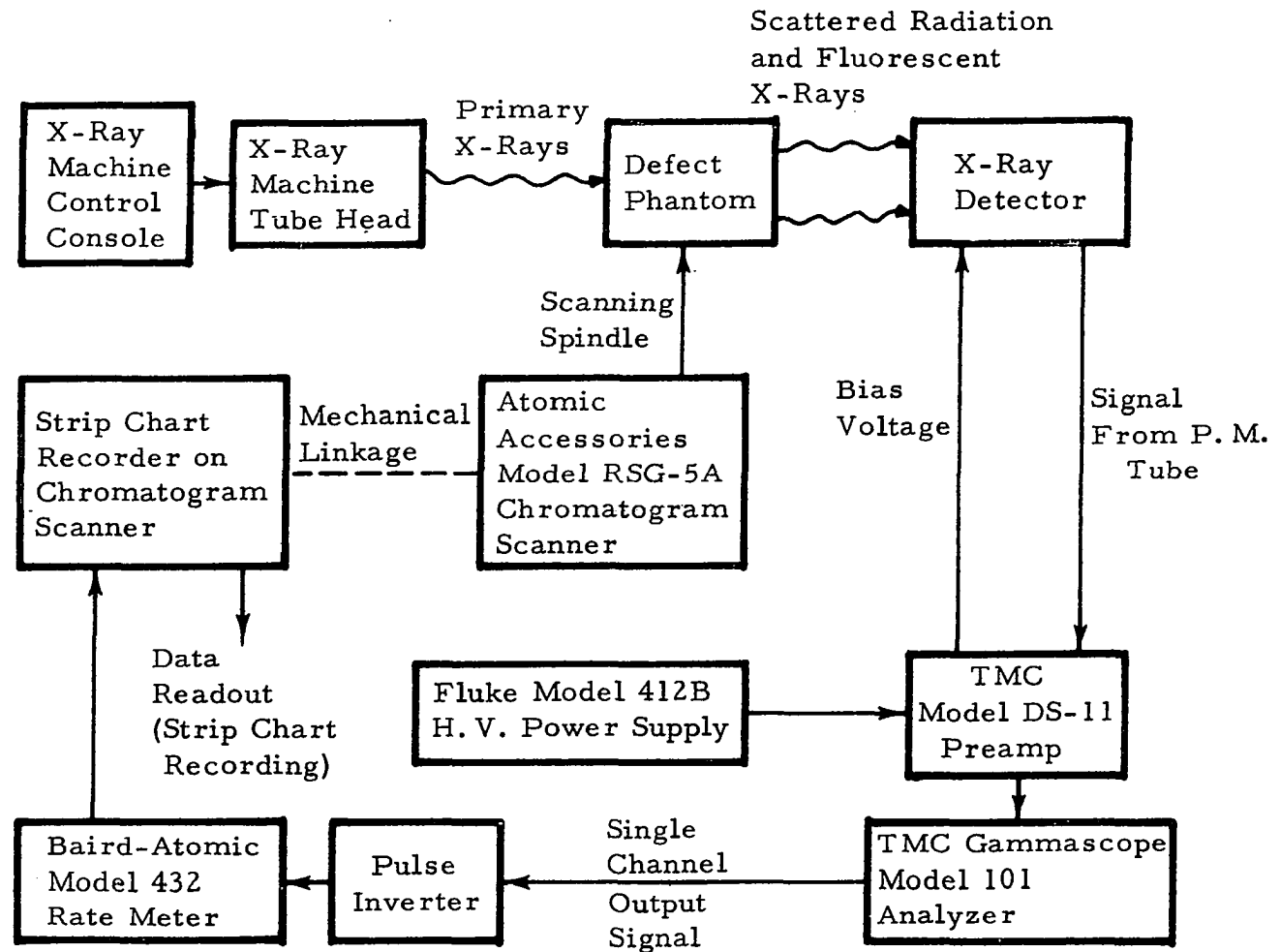


Figure 3-14 Functional Block Diagram of Defect Scanning System

Proper alignment of the system was accomplished by the procedure described in the preceding section. The gear ratio of the chromatogram scanner was selected to provide a scanning speed of 1.27 cm/sec at the beam trace radius of 6.05 cm.

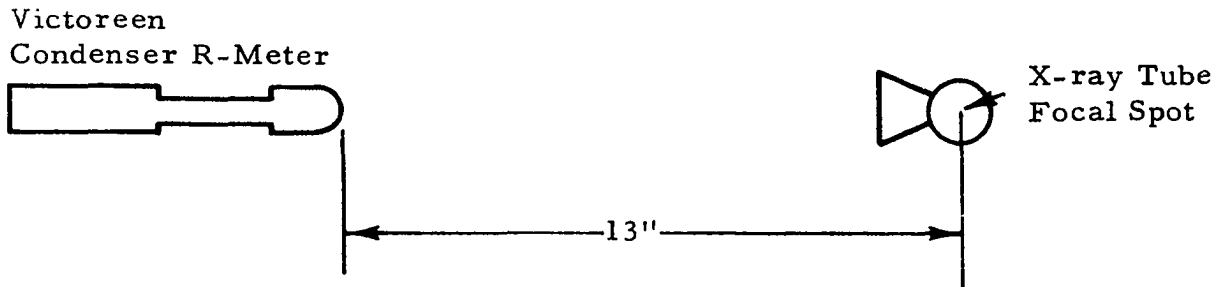
The single-channel output of the TMC Gammascopie was fed through the pulse inverting amplifier to a count rate meter which provided the deflection voltage for the strip chart recorder on the chromatogram scanner. As with the concentration sensitivity measurements, defect depth was simulated by using overburden layers of 0.635-cm-thick lucite sheet.

To complete a single trace scan of the "hot spot" defect phantom, the phantom was mounted on the chromatogram support cone so that the linear defects formed a radial pattern from the center of the spindle. With the chromatogram scanner turned on and the X-ray machine set at 78 KV-3 MA, the scan was initiated with a lead-in time of about 90 sec to record background signal intensity before the first defect entered the excitation beam. After all four defects passed through the excitation beam, the scan was terminated and a 0.635-cm-thick sheet of lucite was added to the overburden to establish a new defect depth. This procedure was repeated until the defect signal could no longer be distinguished from variations in the background count rate.

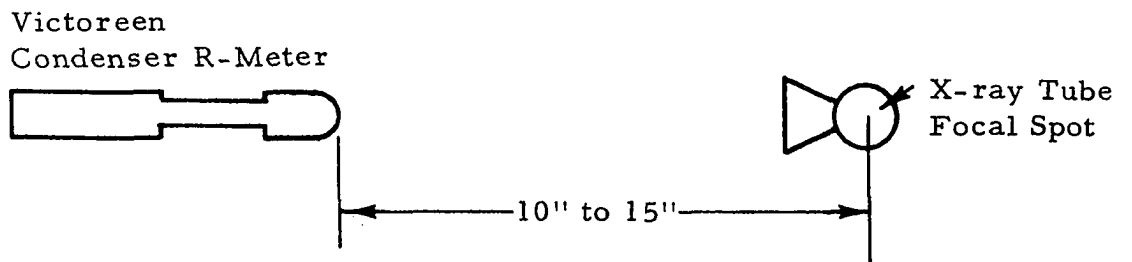
The same scanning procedure was used for the "cold spot" defect phantom.

3.2.3 Dosimetry

The experimental geometries illustrated in Figures 3-15a, b, and c were used to establish the dependence of primary X-ray dose rate on X-ray machine KV setting, distance from the X-ray tube focal spot, and lucite overburden thickness, respectively. In each of these experiments, a Victoreen Instrument Co. Model 326 condenser r-meter was used to measure exposure dose during a time interval that was controlled by the X-ray machine on-off switch. This chamber is designed so that the thickness and composition of the wall and electrode materials produce air-equivalent energy response from 30 to 400 keV (effective energy) with a rated accuracy of $\pm 10\%$. Radiation dosimetry data were required to calculate the iodine K-series fluorescent X-ray intensity per unit surface dose rate under various experimental conditions and to estimate the effective energy of the excitation beam. The lucite attenuation measurements also provided an indication of the depth dose rate distribution in the biological phantom.



- a. Geometry for measuring dependence of primary X-ray dose rate on X-ray machine KV setting



- b. Geometry for measuring dependence of primary X-ray dose rate on distance

Figure 3-15 Geometries Used for Dosimetry Measurements

SECTION 4

DATA REDUCTION AND EXPERIMENTAL RESULTS

4.1 DEPENDENCE OF FLUORESCENT X-RAY INTENSITY ON TRACER ELEMENT CONCENTRATION AND ORGAN DEPTH

The results from both the concentration sensitivity and dosimetry experiments were used to calculate the fluorescent X-ray intensity per unit surface dose rate as a function of tracer element concentration and organ depth.

The experimental data for each fluorescent X-ray intensity measurement consisted of ten 1-min scattered radiation counts from a water sample and ten 1-min counts, under the same experimental conditions, from a sample containing a known concentration of iodine. Since a large number of such measurements were made, a program was written for the University of Oklahoma IBM 360/40 computer to calculate the average count rate from each sample, the difference count rate between each set of samples, and the experimental standard deviations. The results of these calculations are presented graphically in Figure 4-1, and example data for a single point on this graph are listed in Table 4-1.

Smooth curves drawn through the experimental data points in Figure 4-1 were obtained by first calculating the quantity $I_K^Z (4\pi R^2) / I_{11} A_1$ from Equation 2-62A for several assumed monoenergetic excitation source energies. Those curves which provided the best agreement with the experimental results were then normalized to the experimental data points for an iodine concentration of 50,000 ppm. Since a heavily filtered continuous radiation spectrum from an X-ray tube operating at 78 KVP will have a peak intensity at about 52 keV these values do not seem unreasonable.

It is apparent from Figure 4-1 and Table 4-1 that instabilities in the primary X-ray source and detector electronics and a high scattered radiation intensity resulted in large experimental standard deviations at low iodine concentrations. The importance of this is clearly demonstrated by the iodine K X-ray count rate data in Table 4-1 which show an experimental

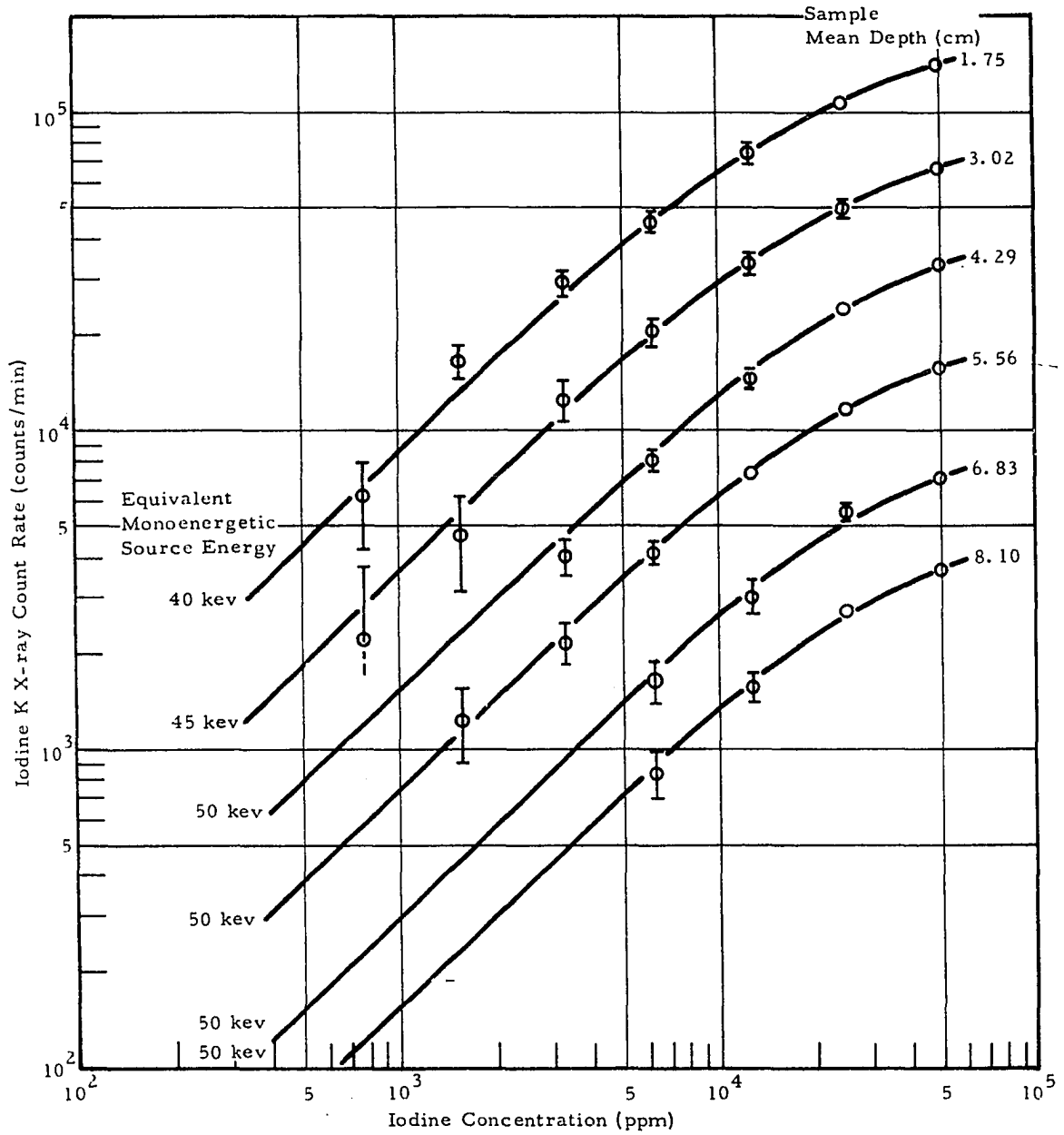


Figure 4-1 Iodine K X-Ray Count Rate as a Function of Iodine Concentration for Several Sample Depths

TABLE 4-1

EXAMPLE IODINE K X-RAY INTENSITY DATA

Sample Mean Depth: 4.29 cm

Iodine Concentration: 3,125 ppm

<u>Count No.</u>	<u>Water Sample Count (1 min)</u>	<u>Iodine Sample Count (1 min)</u>
1	69,005	73,112
2	68,716	72,523
3	69,108	72,636
4	69,026	72,680
5	68,958	72,922
6	68,415	73,488
7	68,267	72,615
8	68,302	72,575
9	68,500	72,649
10	69,047	72,236

Average Count Rate and

Experimental Standard Deviation 68,734 \pm 335 cpm72,745 \pm 350 cpm

Difference Count Rate

and Experimental Standard Deviation: 4,001 \pm 485 cpm

Total Water Sample Count: 687,340 counts

Total Iodine Sample Count: 727,450 counts

Difference Count Rate and \sqrt{N} : 4,001 \pm 63.5 cpm

standard deviation that is over four times greater than would be obtained (\sqrt{N}) if the instrumentation were perfect, and the scattered X-ray intensity negligible.

Since the distance between the X-ray tube target and the biological phantom was changed for each sample depth, the air dose rate at the phantom surface in each position was determined by first measuring the variation in air dose with distance from the X-ray tube target. The results of these measurements are presented in Figure 4-2 and are considered accurate to about $\pm 10\%$. To facilitate extrapolation, a $1/r^2$ dependence was assumed and the experimental data were found to be suitably described by:

$$D = \frac{1,710}{r^2} \quad (\text{r/min}) \quad (4-1)$$

where r is in inches.

The iodine K X-ray intensity measurements from Figure 4-1 were divided by the appropriate air dose rates at the phantom surface to construct the curves shown in Figure 4-3. It should be noted that the ordinate in Figure 4-3 is labeled as the iodine K X-ray intensity per unit surface dose rate, whereas only air dose rates at the surface were actually measured. This direct conversion of units is justified in this case, since the uncertainty in the air dose rate measurements ($\pm 10\%$) was greater than the difference between the absorbed dose per röntgen and the absorbed dose per rad in lucite ($\approx 7\%$).

Since the experimental geometry used for these measurements is quite similar to that shown in Figure 2-3, Equations 2-16, 2-29, and 2-31 can be combined to obtain the following expression for the iodine fluorescent X-ray count rate per unit surface dose rate:

$$\frac{C_K^Z}{D} = \frac{6.25 \times 10^7 (\pi R_1^2) A_2 \epsilon_K^Z \omega_K^Z}{E_1 (\mu_{m-abs})^W E_1 (4\pi R^2) \sin^2 \phi} \cdot \frac{r_K^{Z-1}}{r_K^Z} \cdot \frac{e^{-\alpha^I X_1} \tau_1^{Z,0}}{\alpha^O} \left[1 - e^{-\alpha^O (X_4 - X_1)} \right] \quad (4-2)$$

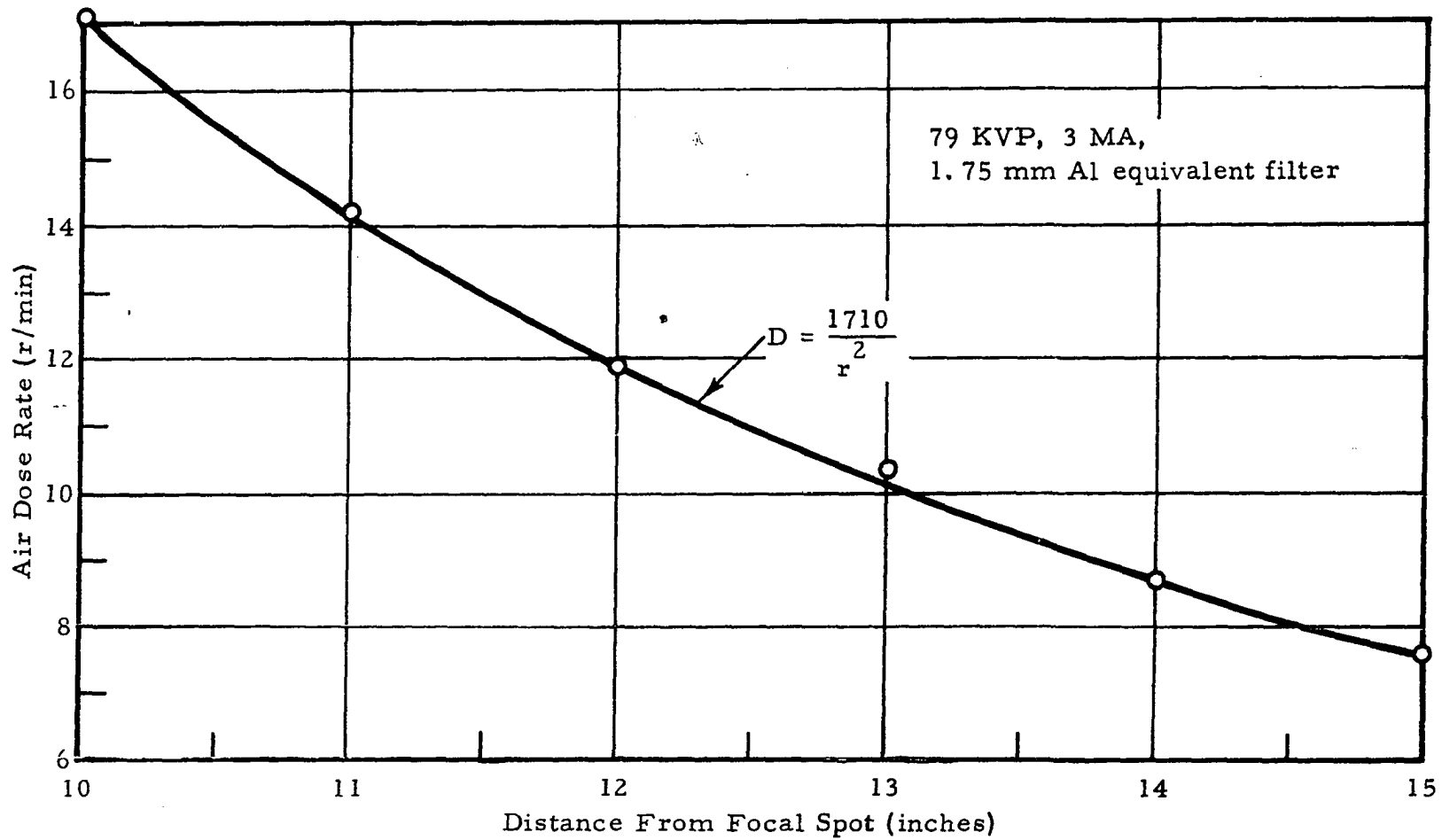


Figure 4-2 Dependence of Air Dose Rate on Distance From X-Ray Tube Target

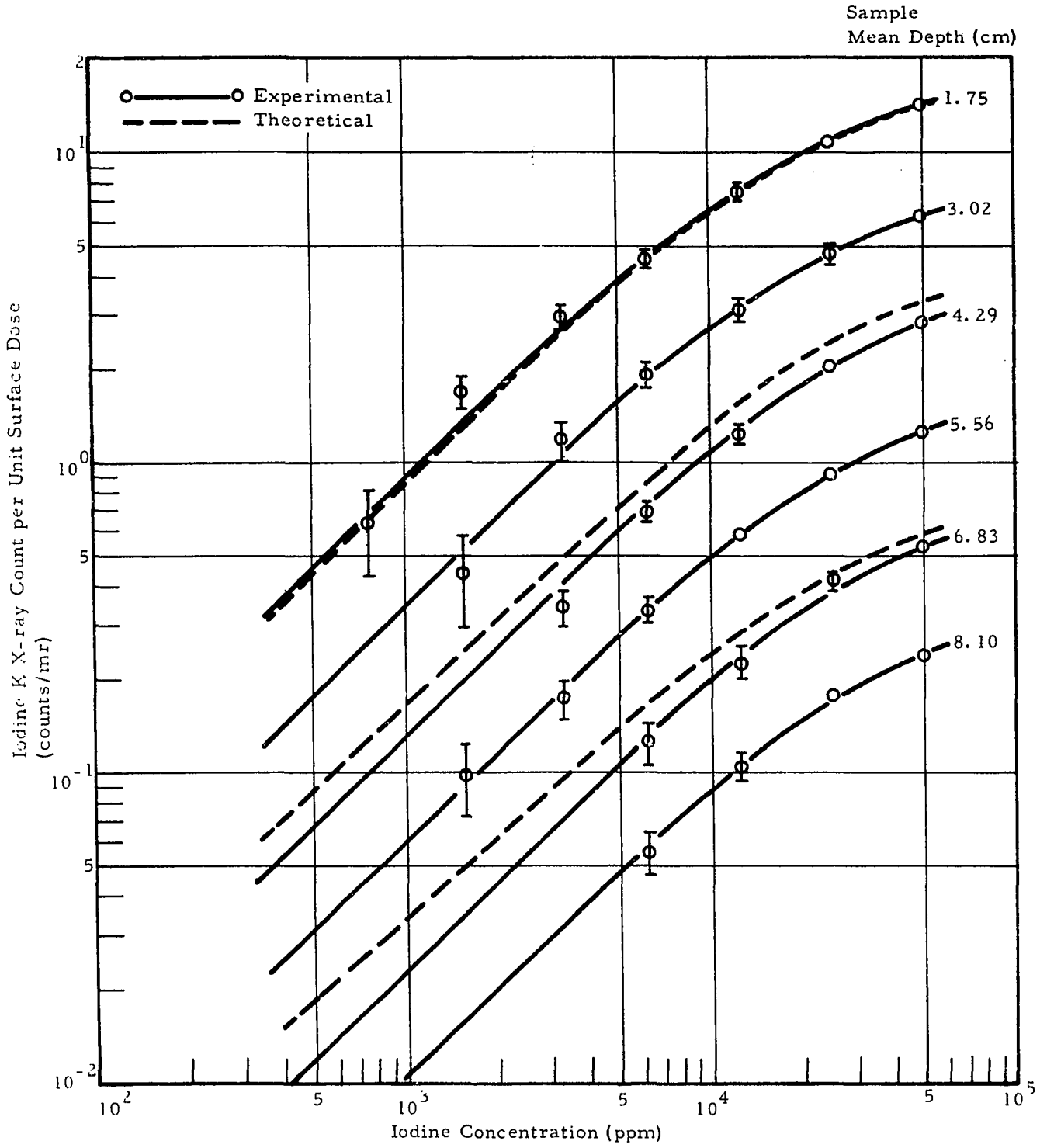


Figure 4-3 Iodine K X-Ray Count per Unit Surface Dose as a Function of Iodine Concentration for Several Sample Depths

In this case, approximate values of the energy-independent terms are:

$$\pi R_1^2 = \text{effective collimator resolution area} = 0.954 \text{ cm}^2$$

$$A_2 = \text{detector open area} = 0.376 \text{ cm}^2$$

$$\epsilon_K^Z = \text{detector efficiency} \approx 100 \% \text{ cm}$$

$$\omega_K^Z = \text{iodine fluorescence yield} = 0.88$$

$$r_K^Z = \text{iodine absorption jump ratio} = 6.34$$

$$\phi = \text{primary X-ray incidence angle} = 60^\circ$$

$$X_1 = \text{sample depth} = 0.0, 1.27, 2.54, 3.81, 5.08, 6.35 \text{ cm}$$

$$X_4 - X_1 = \text{sample thickness} = 3.3 \text{ cm}$$

$$R = \text{sample-detector distance} = 26.7 \text{ cm}$$

The effective collimator resolution area (πR_1^2), was determined from Figure 3-7 using the integration scheme illustrated in Figure 4-4. This was accomplished by multiplying the incremental area dA at a radius r from the focal point in the focal plane by the relative response at this radius, $\eta(r)$, and integrating the product over r from $r = 0$ to $r = R_r$, the resolution radius.

$$\pi R_1^2 = \int_0^{R_r} \eta(r) \cdot 2\pi r dr \quad (4-3)$$

For simplicity, it was assumed that $\eta(r)$ could be described by the straight line

$$\eta(r) = 1 - 3.33 r \quad (4-4)$$

for which the effective collimator resolution area is 0.607 cm^2 .

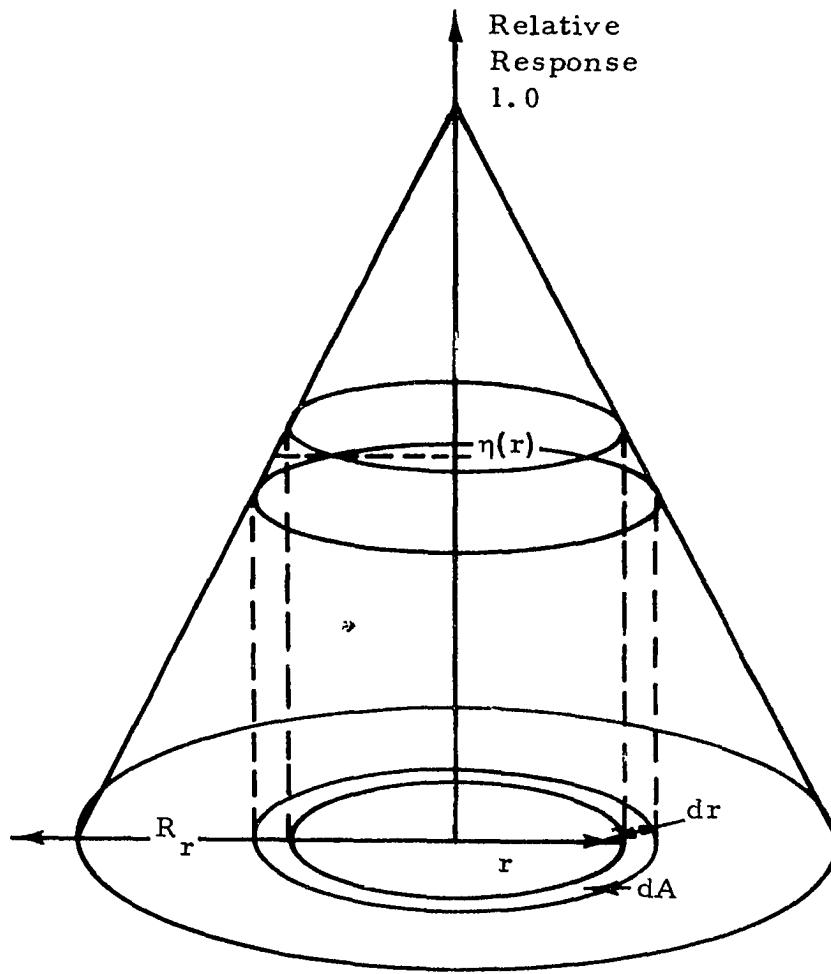


Figure 4-4 Geometry for Calculating Effective Collimator Resolution Area

Evans (Ref. 51) has shown that if the source is spherical instead of planar, the effective collimator resolution area should be increased by the ratio $0.107 R_r/0.0625$. Since the cylindrical sample holders for these experiments were more nearly spherical than planar, the effective collimator resolution area was taken as 0.954 cm^2 .

If Equation 4-2 is correct one should be able to calculate the fluorescent X-ray count per unit surface dose from the energy spectrum of the excitation source.

To substantiate this line of reasoning and in turn to verify the theoretical calculations presented in Section 2, the energy spectrum of the excitation source used in these experiments was measured by placing the scintillation detector 250 cm from the X-ray tube focal spot and covering all holes, except the center hole, of the detector collimator with 0.094-in.-thick lead sheet. The measured energy spectrum divided into 5-keV energy intervals is presented in Figure 4-5. For calculation purposes, all of the primary photons in each energy interval were assumed to have the mean energy of that interval and the spectrum was corrected to an air attenuation path length of 35 cm as indicated by the dotted lines in Figure 4-5. It should be noted at this point that Equation 4-2 is only applicable for primary X-rays with energies greater than the K-absorption edge energy of the tracer element. A calculation procedure must therefore be devised which properly accounts for the radiation dose delivered to the biological system by low energy primary X-rays ($E_1 < E_{K\text{-abs}}$). In equation form, a suitable procedure can be defined as follows:

$$\frac{C_K^Z}{D} = \frac{\sum_{E_1 = E_{K\text{-abs}}}^{E_1 \text{ max}} \left[\left(\frac{C_K^Z}{D} \right)' \cdot \frac{D}{I_1} \cdot I_1' \right]_{E_1}}{\sum_{E_1 = E_{1 \text{ min}}}^{E_1 \text{ max}} \left[\frac{D}{I_1} \cdot I_1' \right]_{E_1}} \quad (\text{counts/mrad}) \quad (4-5)$$

Here, I_1' denotes the fractional intensity of primary X-rays with energy E_1 , and $(C_K^Z/D)'$ is the fluorescent X-ray intensity per unit surface dose rate calculated from Equation 4-2 for excitation energy E_1 . For this analysis, a computer program was written to calculate values of $(C_K^Z/D)'$,

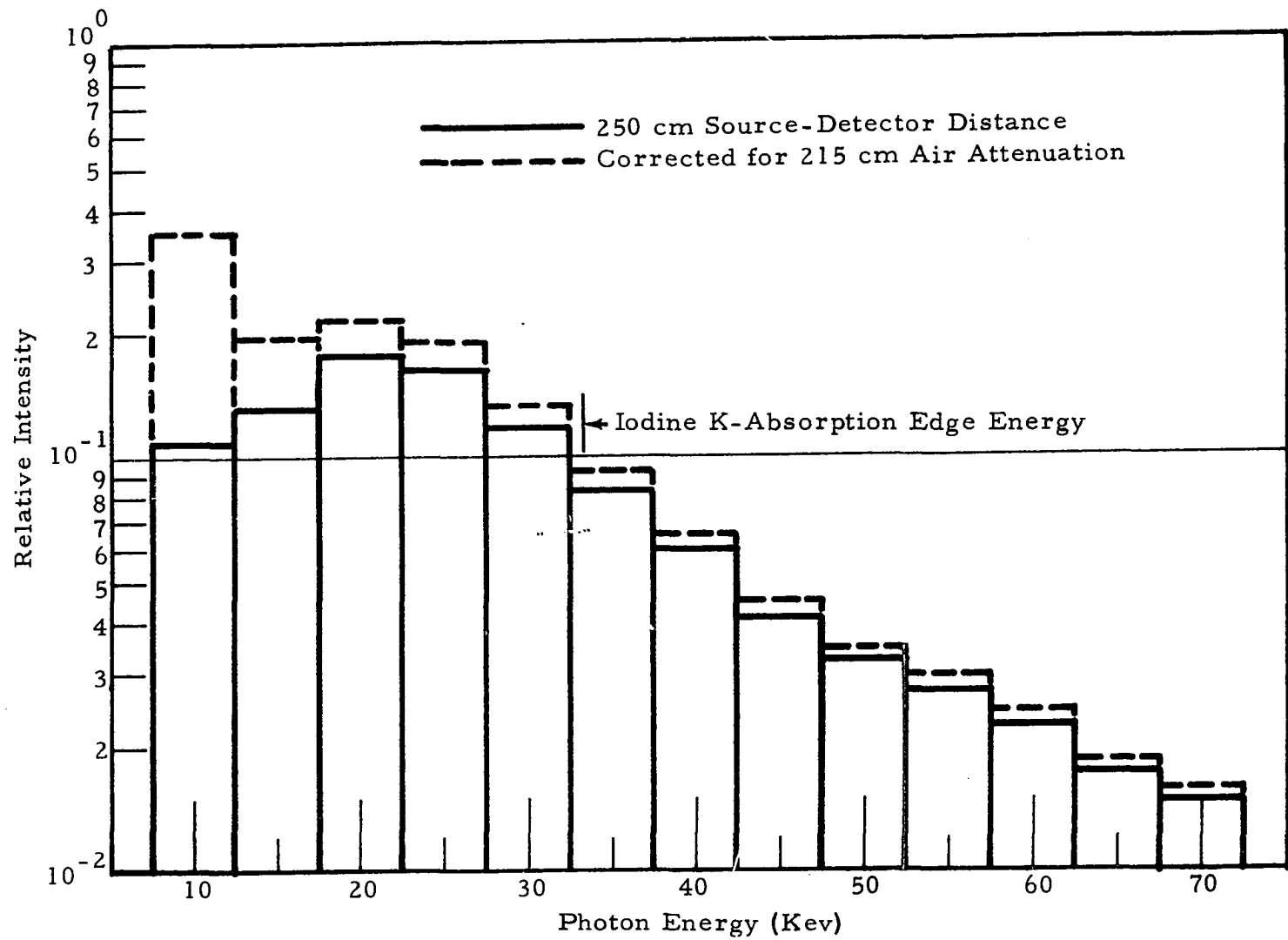


Figure 4-5 Measured Excitation Source X-Ray Spectrum and Spectrum Corrected to 35 cm Source-Detector Distance

and appropriate values for D/I_1 and I_1^1 were obtained from Figures 2-10 and 4-5, respectively. Values of C_K^Z/D calculated by use of this technique for mean sample depths of 1.75, 4.29, and 6.83 cm are shown as dotted lines in Figure 4-3.

The close agreement between the experimental and theoretical results is fortuitous in view of the numerous assumptions involved in the calculations and the errors associated with the experiment. Important sources of error in the theoretical calculations are the assumptions that were made concerning the detector collimator resolution area, the energy spectrum of the primary X-ray beam, the experimental geometry, and the atomic properties of the biological phantom. Errors in the experimental values of C_K^Z/D could result from geometrical misalignment of the system components, instabilities in the X-ray machine and detector electronics, the statistical nature of the accumulated data, as well as uncertainties in the dose rate measurements.

It should be noted that the values of C_K^Z/D presented in Figure 4-3 are 15 to 20 times smaller than the values calculated from Equation 4-2 for a 35-keV monoenergetic excitation source under these same experimental conditions.

4.2 DEPENDENCE OF FLUORESCENT X-RAY INTENSITY ON EXCITATION ENERGY

In this series of experiments, the dependence of the iodine fluorescent X-ray count rate on X-ray machine KV setting at 3 MA was measured for a sample containing 2.5×10^4 ppm I at mean sample depths of 1.75, 4.29, and 6.83 cm. The results of these measurements are presented graphically in Figure 4-6. The calculated experimental standard deviations are indicated by vertical bars through each data point, and horizontal bars indicate the estimated uncertainty in reading the KV meter (± 1 keV). The dotted curves on this graph were obtained by normalizing Blokhin's (Ref. 1) empirical equation:

$$I_K^Z \propto (V - E_{K-abs})^{1.79}$$

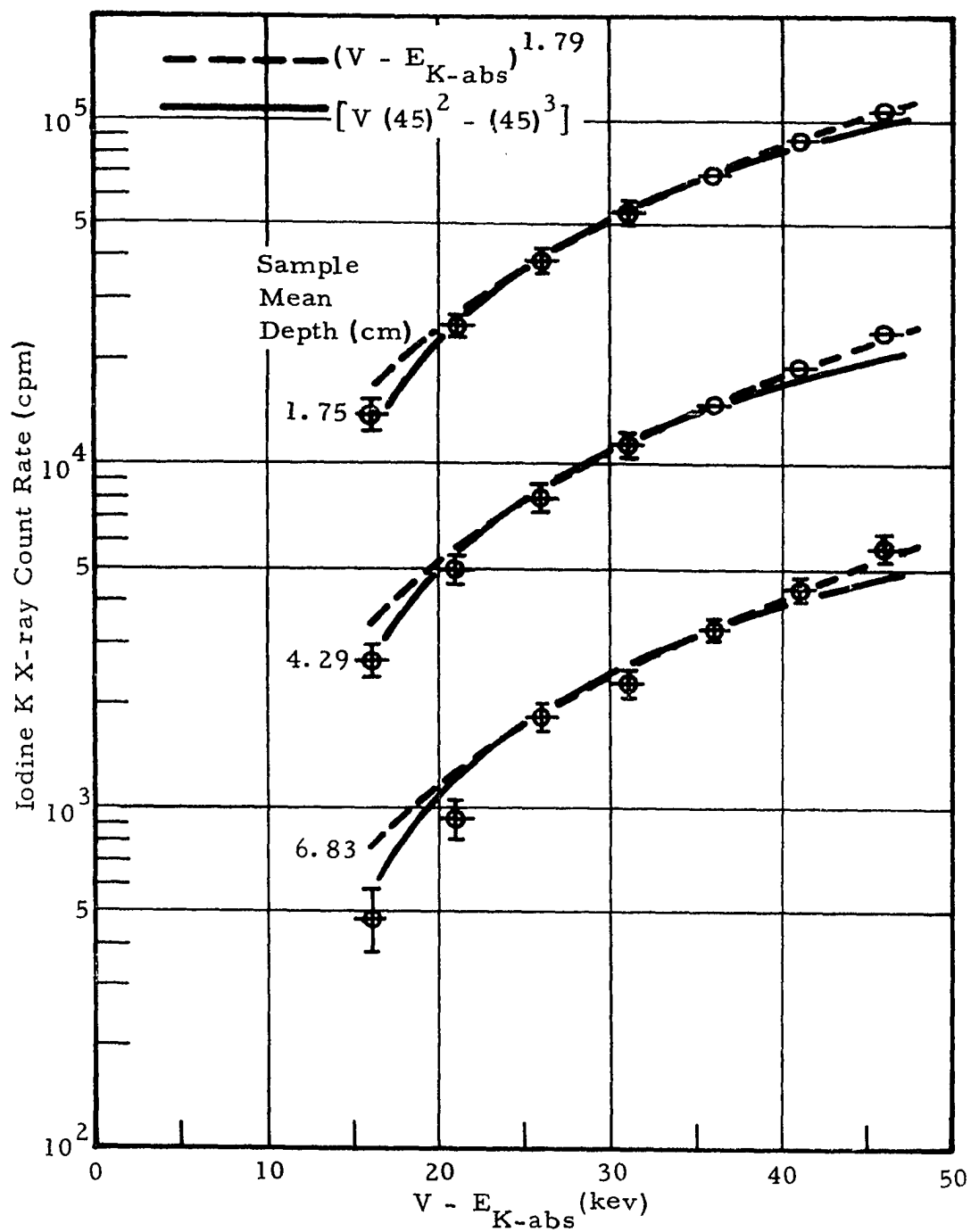


Figure 4-6 Dependence of Iodine K X-Ray Count Rate on X-Ray Machine KV Setting

to the experimental data points at $(V - E_{K-abs}) = 36$ kev. This energy was selected for normalization because, theoretically, the dotted curves should fall below the measured values of I_K^Z as the X-ray tube voltage is increased beyond the tungsten target K excitation level (69.5 kev). Above this energy level, the iodine K-series fluorescent X-ray excitation by the continuous spectrum is supplemented by tungsten target K X-ray excitation which is described by the dependence:

$$I_K^Z \propto (V - E_{K-abs})^2.$$

Such an effect is noticeable on the two lower curves where the continuous spectrum is heavily filtered by overburden lucite, but at these voltage levels only a small fraction of the excitation is provided by tungsten target K X-rays.

The experimental data presented in Figure 4-1 indicate that the effective excitation energy increased from about 40 to 50 kev as the sample mean depth increased from 1.75 to 6.83 cm. One would therefore expect reasonably good agreement between the iodine K X-ray count rate and the intensity of 45-kev X-rays in the continuous spectrum which can be calculated from Equation 2-78. This dependence is indicated by the solid curves in Figure 4-6 where the theoretical calculations were again normalized to the data points at $(V - E_{K-abs}) = 36$ kev.

Both of the calculation procedures described above provide results that are in good agreement with the experimental data over the KV range used in these experiments.

To determine the iodine K-series fluorescent X-ray intensity per unit surface dose rate as a function of X-ray machine KV setting, air dose rates were measured for several KV settings at 3 MA using the geometry illustrated in Figure 3-15. The results of these measurements are shown in Figure 4-7. The smooth curve through the data points was obtained by normalizing the equation

$$D = K V^M \tag{4-6}$$

to the dose rate measurements at 49 and 69 KV. Assuming that this dose rate dependence on voltage does not change appreciably with distance over

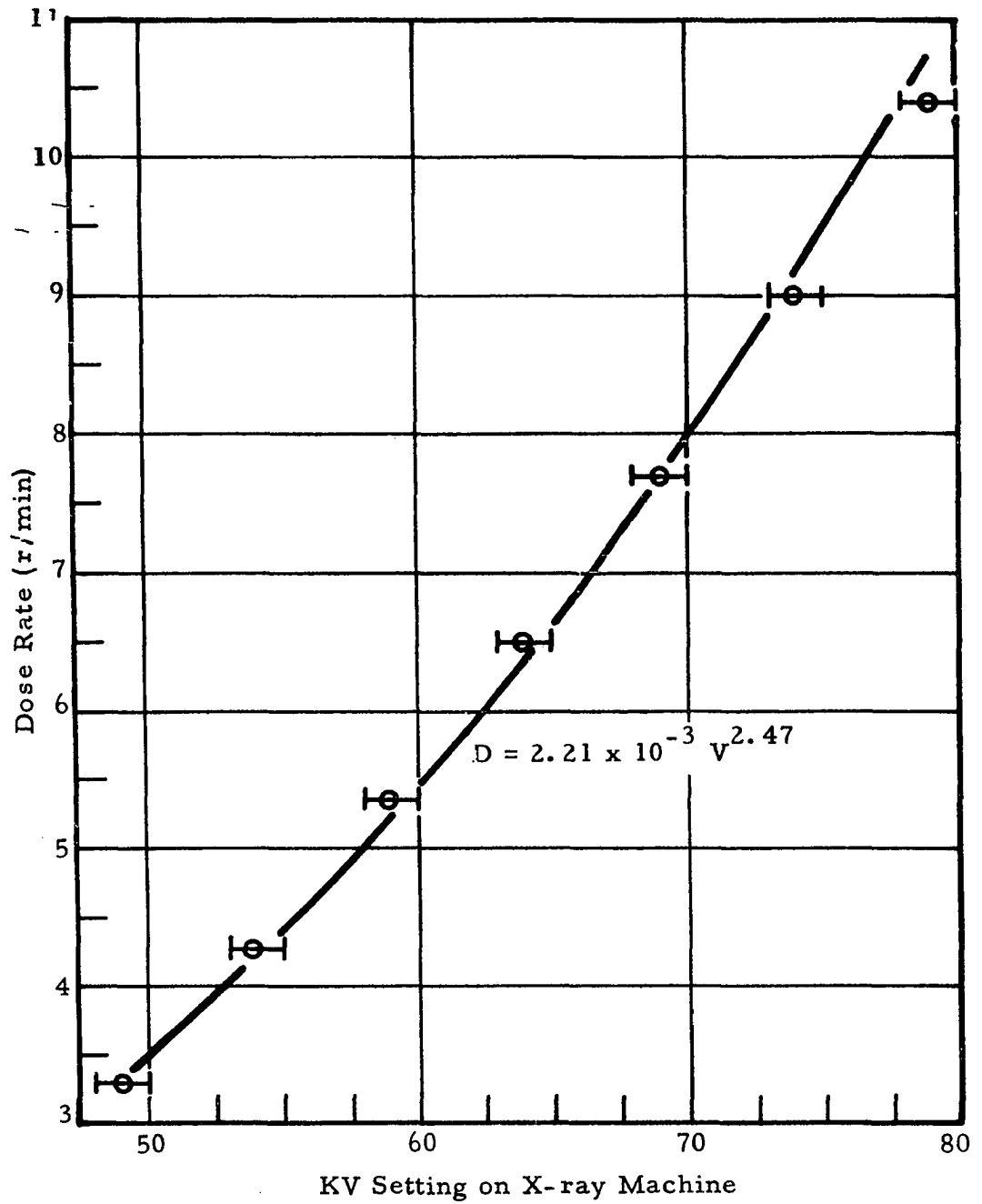


Figure 4-7 Dependence of Air Dose Rate on X-Ray Machine KV Setting

the short range of interest in this application, one can use the results presented in Figures 4-2, 4-6, and 4-7 to calculate the dependence of the ratio C_K^Z/D on X-ray tube voltage. The results of these calculations are presented in Figure 4-8. The smooth curves on this graph were calculated from the equation

$$\frac{C_K^Z}{D} \propto \frac{V(45)^2 - (45)^3}{V^{2.47}} \quad (4-7)$$

normalized to the experimental data points at $(V - E_{K-abs}) = 36$ kev. These results show a general increase in C_K^Z/D with increasing X-ray tube voltage.

4.3 DEFECT LOCALIZATION

Preliminary experiments were conducted to examine "hot spot" and "cold spot" defect localization using combined excitation source and X-ray detector collimation with the geometry illustrated in Figure 3-13. The results of these experiments are presented in Figures 4-9 and 4-10.

The "hot spot" defect phantom scans in Figure 4-9 show that the 0.25-cm-diameter defect can be suitably defined at a depth of 3.49 cm and that the 0.18-cm-diameter defect is clearly visible at a depth of 1.59 cm. Results of subsequent experiments using this same equipment with a new detector collimator show that the 0.25-cm-diameter defect can still be resolved at a depth of 5.4 cm (Ref. 52).

It can be seen in Figure 4-10 that the "cold spot" defect produced a significant decrease in count rate for defect depths up to 3.35 cm. However, at greater depths the change in count rate at the defect could not be distinguished from background count rate variations.

The results presented here are only preliminary, and several changes in experimental equipment and techniques could be made to improve the delineation of tracer element distributions in a biological system. For example, a substantial improvement would result from the use of a monoenergetic excitation source with an energy that just

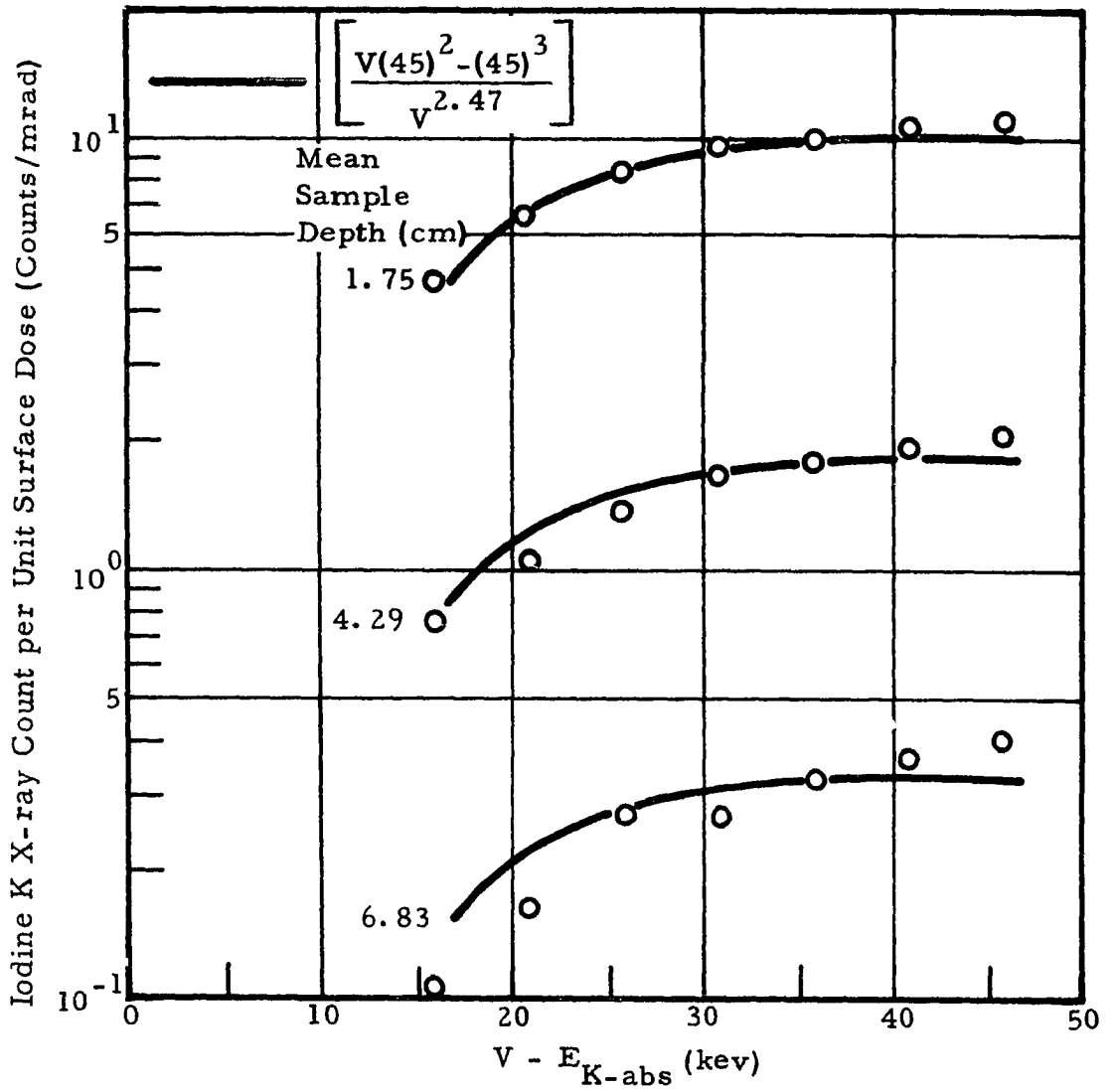


Figure 4-8 Variation of Iodine K X-Ray Count per Unit Surface Dose With X-Ray Machine KV Setting

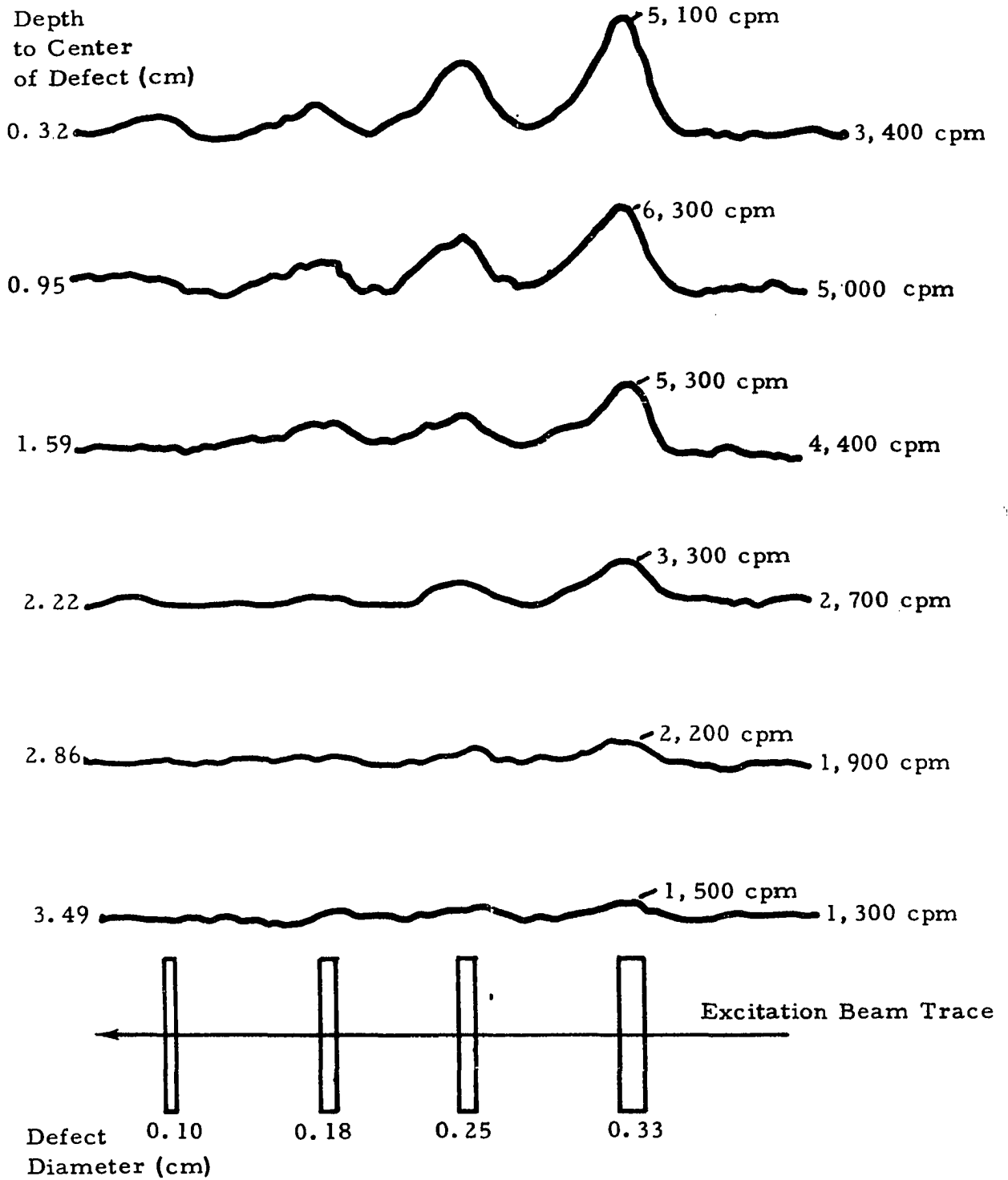


Figure 4-9 Linear Scans of "Hot Spot" Defect Phantom

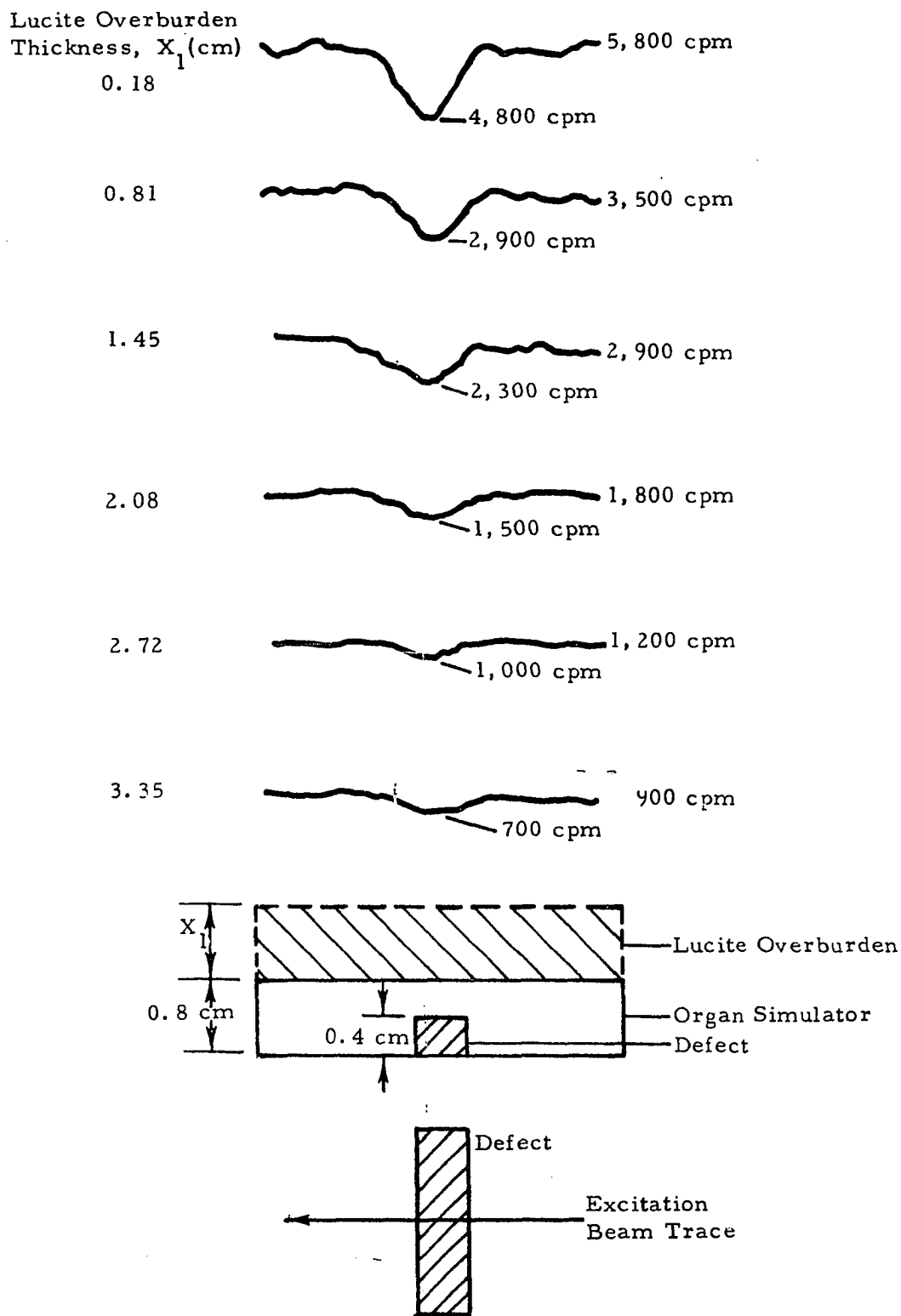


Figure 4-10 Linear Scans of "Cold Spot" Defect Phantom

exceeds the K-absorption edge energy of the tracer element. Such a source would provide an increase in the signal-to-background intensity ratio at the detector with a lower dose rate to the biological system. In addition, with an excitation source of this type many of the Compton-scattered primary photons would not have sufficient energy to excite K-series fluorescent X-rays in the tracer element. This would limit the effective diameter of the excitation beam and improve resolution. Other refinements include the use of a radiation detector with better energy resolution and a source-detector configuration that would maximize the fluorescent X-ray count per unit surface dose.

In spite of the limitations of the equipment used for these experiments, the results are very encouraging and indicate the need for continued experimental work in this area.

SECTION 5

SUMMARY

The application of fluorescent X-ray techniques to biological studies is not new. A number of investigations have been reported (Ref. 21, 53 - 66) in which bone, tissue, and blood samples were chemically analyzed using X-ray fluorescence spectroscopy. However, in each case, the samples were extracted from the biological system prior to analysis and in many instances, the samples were chemically processed to increase the concentration of the trace elements being studied.

The results obtained in this preliminary experimental program verify a number of the theoretical concepts and semiempirical equations presented in Section 2, and indicate that externally excited high-Z tracer element fluorescent X-rays could be useful for some types of in vivo biological and medical investigations that are presently being conducted with radioactive tracers. An extensive research effort, however, involving close cooperation between physicians, physicists, engineers, and pharmaceutical chemists will be required to fully evaluate the usefulness of this technique.

Three major objectives in designing a fluorescent X-ray instrumentation system for conducting in vivo biological and medical studies are:

1. To obtain a fluorescent X-ray signal of suitable intensity from a localized region of the biological system with a minimum radiation dose rate
2. To separate the fluorescent X-ray signal from background "noise"
3. To process and display the information obtained in such a manner that it is easy to understand and interpret.

These objectives can only be accomplished by ensuring that the excitation source, the fluorescent X-ray detector, and the source-detector geometry are selected to achieve optimum performance under the constraints imposed by the biological system. It is possible therefore that a number of instrumentation systems or modifications of a particular system will be needed to perform different types of investigations.

Fortunately, much of the technology required for the application described in this report has been established for fluorescent X-ray chemical analysis, nuclear medical studies, and radiological diagnostics. A wide variety of excitation sources and fluorescent X-ray detectors, as well as the techniques for using these devices to maximum advantage, have been developed through several years of research in the field of fluorescent X-ray chemical analysis. Medical radioactive tracer studies with both stationary and scanning detection systems have provided an excellent understanding of the problems associated with data acquisition and interpretation. In addition, high-Z elements (e.g. iodine and barium) have been used extensively to improve contrast for radiological diagnostic procedures. By combining the basic technologies that exist in these three separate disciplines and making the necessary modifications in experimental equipment and techniques, it is felt that a new and useful method of studying organ circulation, function, and structure in vivo can be developed.

SECTION 6

LIST OF REFERENCES

1. Compton, A.H., and Allison, S.K., "X-Rays in Theory and Experiment," D. Van Nostrand Company, Inc., New York (1935).
2. Blokhin, M.A., "The Physics of X-Rays," 2nd rev. ed., Trans. Series AEC-tr-4502, Phys. Office of Technical Services, Department of Commerce (1957).
3. Blokhin, M.A., "X-Ray Spectroscopy," Hindustan Publ. Corp., Delhi, India (1962) English Ed.
4. Prince, B.T., Horton, C.C., and Spinney, K.T., "Radiation Shielding," Reactor Design Physics, Vol. 2, Pergamon Press, Oxford, England (1957).
5. Glass, H.I., "A Depth-Focussing Collimator for the Investigation of the Brain Cortex," Proceedings of the Symposium on Medical Radioisotope Scanning, I.A.E.A. (1964).
6. Sherman, J., "The Theoretical Derivation of Fluorescent X-Ray Intensities from Mixtures," Spectrochim. Acta, 7, No. 5 (1955).
7. Abramowitz, M., and Stegun, I.A., Eds. "Handbook of Mathematical Functions," National Bureau of Standards (US) AMS, 55, (1964).
8. Broyles, C.D., Thomas, D.A., and Haynes, S.K., "The Measurement and Interpretation of the K Auger Intensities of Sn^{113} , Cs^{137} , and Au^{198} ," Phys. Rev. 89, No. 4, Feb. 15 (1953) pp. 715-24.
9. Heintz, J.Z., Physics 143, (1955) p. 153.
10. Davidson, F.D., and Wyckoff, R.W.G., "X-Ray Fluorescent Yields from Several Light Elements," J. Appl. Phys. 33, No. 12 (Dec. 1962) pp. 3528-29.
11. Burhop, E.H.S., The Auger Effect and Other Radiationless Transitions, Cambridge University Press, London (1952).
12. Berkey, D.K., Phys. Rev. 45, (1934) p. 437.
13. Pincherle, L., Nuovo Cim. 12, (1935) p. 81.

14. Jonsson, E., Dissertation, Uppsala (1929).
15. Grodstein, G. W., "X-Ray Attenuation Coefficients from 10 Kev to 100 Mev," NBS Circular 583, (1957). (Revised by McGinnies, R. T. in 1959).
16. McMasters, R. C., ed., Nondestructive Testing Handbook, Vol. I, New York, The Ronald Press Co., (1959).
17. Leroux, J., "Absorption Coefficients (Mass): Empirical Determination Between 1 and 50 KEV," The Encyclopedia of X-Rays and Gamma Rays, ed. George L. Clark, Reinhold Publishing Corp., New York, (1963).
18. Cameron, J. F., and Rhodes, J. R., "Filters for Energy Selection in Radioisotope X-Ray Techniques," The Encyclopedia of X-Rays and Gamma Rays, ed. George L. Clark, Reinhold Publishing Corp., New York, (1963).
19. Evans, R. D., The Atomic Nucleus, McGraw-Hill Book Company, Inc., (1955).
20. Rogers, T. H., "Production of Monochromatic X-Radiation for Microradiography by Excitation of Fluorescent Characteristic Radiation," J. Appl. Phys., Vol. 23, No. 8, August (1952), pp. 881-887.
21. Hall, T., "X-Ray Fluorescence Analysis in Biology," Science 134, (1961), pp. 449-455.
22. Florowski, T., Kosiara, A., and Wasilewska, M., "Comparison of Radioisotope Bremsstrahlung Sources for Excitation of the Characteristic Radiation in Elements of $14 < Z < 50$," Nukleonika, 10, (1965), pp. 661-668.
23. Tanemura, T., "Performance of an X-Ray Spectro-Analyzer Using Pm^{147} Beta-Ray Source," Jap. J. Appl. Phys., 5, (Jan. 1966), pp. 51-58.

24. Martin, T. C., and Blake, K. R., "A Study of Fluorescent Excitation Using Isotopic X-Ray Emission," Contract AT (40-1)-3224, (1965), (Texas Nuclear Corporation, Austin, Texas).
25. Preuss, L. E., Collins, H., and Wilson, E. R., "A Compilation of Beta-Ray Stimulated X-Ray Spectra," Advan. X-Ray Anal., 8, (1965), pp. 198-203.
26. Karttunen, J. O. and Henderson, D. J., "Developments in a Portable X-Ray Fluorescence Instrument Using Radioisotope Excitation Sources," Proc. Symp. on Low Energy X- and Gamma-Ray Sources and Applications, Chicago (1964), ORNL-11C-5 (1965), p. 154.
27. Ezpo, J. J., and Stinchcomb, T. G., "Study, Design, and Applications of Beta-Excited X-Ray Sources," Proc. Symp. on Low Energy X- and Gamma Sources and Applications, Chicago (1964), ORNL-11C-5 (1965), p. 4.
28. Preuss, L. E., Collins, H., and Kann, J., "X-Ray Absorptiometry with Beta-Stimulated X-Ray Sources and Progress Report on Compilation of Beta-Excited Spectra," Proc. Symp. on Low Energy X- and Gamma Sources and Applications, Chicago (1964), ORNL-11C-5 (1965), pp. 51-71.
29. Bustard, T. S., and Silverman, J., "Bremsstrahlung from ^{90}Sr - ^{90}Y in Thin Absorbers," Proc. Symp. on Low Energy X- and Gamma-Ray Sources and Applications, Chicago (1964), ORNL-11C-5 (1965), pp. 91-98.
30. Truscello, V. C., and Silverman, J., "External Bremsstrahlung Produced in Thin Foils by ^{147}Pm ," Proc. Symp. on Low Energy X- and Gamma-Ray Sources and Applications, Chicago (1964), ORNL-11C-5 (1965), pp. 99-106.
31. Cameron, J. F., and Rhodes, J. R., "Beta-Excited Characteristic X-Rays and Energy Reference Sources," Intern. J. of Appl. Rad. and Iso., 7, (1960), p. 244.
32. Preuss, L. E., Horn, H., and Keiser, T. W., "The Spectra of Some Beta-Excited X-Ray Sources with the Multichannel Analyzer," Advances in X-Ray Analysis, Vol. 4, Plenum Press, New York, (1960).

33. Rhodes, J. R., "Optimization of Excitation and Detection Techniques for Analysis of Silver Ores by Radioisotope X-Ray Spectrometry," Second Symp. on Low Energy X- and Gamma Sources and Applications, University of Texas, Austin, Texas, (March 1967).
34. MacIntyre, W. J., "In Vivo Tracer Studies by External γ -Ray Counting," Instrumentation in Nuclear Medicine, Vol. 1, Gerald J. Hines, ed., Academic Press, (1967).
35. Burkle, J. S., and Gliedman, M. L., "External Recording Method for Estimating Hepatic Blood Flow with the Use of Radiogold," Gastroenterology 36, (1959), p. 112.
36. Taplin, G. V., Hayashi, J., Johnson, D. E., and Dore, E. K., "Liver Blood Flow and Cellular Function in Hepatobiliary Disease. Tracer Studies with Radiogold and Rose Bengal," J. Nucl. Med. 2, (1961), p. 204.
37. Tauxe, W. N., Maher, F. T., and Hunt, J. C., "The Isotope Renogram as a Test of Renal Function," Dynamic Clinical Studies with Radioisotopes (R. M. Kniseley and W. N. Tauxe, eds.), TID-7678, p. 383, U.S. Atomic Energy Commission, Washington, D. C., (1964).
38. Wagner, H. N., Jr., "Regional Blood Flow Measurements with Krypton-85 and Xenon-133," Dynamic Clinical Studies with Radioisotopes (R. M. Kniseley and W. N. Tauxe, eds.), TID-7678, p. 189, U.S. Atomic Energy Commission, Washington, D. C., (1964).
39. Hamilton, W. F., Moore, J. W., Kinsman, J. M., and Spurling, R. G., "Simultaneous Determination of the Pulmonary and Systemic Circulation Times in Man and a Figure Related to the Cardiac Output," Am. J. Physiol. 84, (1928), p. 338.
40. Huff, R. L., Feller, D. D., Judd, O. J., and Bogardus, G. M., "Cardiac Output of Men and Dogs Measured by in vivo Analysis of Iodinated (I^{131}) Human Serum Albumin," Circulation Res. 3, (1955), p. 564.
41. MacIntyre, W. J., Pritchard, W. H., Eckstein, R. W., and Friedell, H. L., "The Determination of Cardiac Output by a Continuous Recording System Utilizing Iodinated (I^{131}) Human Serum Albumin. Animal Studies," Circulation 4, (1951), p. 552.

42. MacIntyre, W. J. Pritchard, W. H., and Moir, T. W., "The Determination of Cardiac Output by the Dilution Method without Arterial Sampling. I. Analytical Concepts," Circulation 18, (1958), p. 1139.
43. Pritchard, W. H., MacIntyre, W. J., and Moir, T. W., "The Determination of Cardiac Output by the Dilution Method without Arterial Sampling. II. Validation of Precordial Recording." Circulation 18, (1958), p. 1147.
44. Taplin, G. V., Dore, E. K., and Johnson, D. E., "Hepatic Blood-Flow and Reticuloendothelial-System Studies with Radiocolloids," Dynamic Clinical Studies with Radioisotopes (R. M. Kniseley and W. N. Tauxe, eds.), TID-7678, p. 285, U.S. Atomic Energy Commission, Washington, D.C., (1964).
45. Brownell, G. L., and Aronow, S., "Radioisotope Scanning," Instrumentation in Nuclear Medicine, Vol. I, (G. J. Hine, ed.) Academic Press, (1967).
46. Dunne, J. A., Nickle, N. L., "Balanced Filters for the Analysis of Al, Si, K, Ca, Fe, and Ni," Second Symp. on Low Energy X- and Gamma Sources and Applications, University of Texas, Austin, Texas (March 1967).
47. Broquet, C., Vacher, M., and Robin, G., "The Realization and Use of X-Ray Filters for Energy Selection," Second Symp. on Low Energy X- and Gamma Sources and Applications, University of Texas, Austin, Texas, (March 1967).
48. Bisi, A., and Zappa, L., Nuovo Cimento, II (5), (1949), p. 985.
49. Narayan, G. H., and Prescott, J. R., I. E. E. E., Trans. Nucl. Sci., 13, (3), (1966), p. 132.
50. Heath, R. L., "Review of Solid-State Detector Systems for X-Ray Spectrometry," Second Symp. on Low Energy X- and Gamma Sources and Applications, University of Texas, Austin, Texas, (March 1967).
51. Evans, W., Experimental Evaluation of Medical Scanners, " PhD. Dissertation, University of Oklahoma, 1965.

52. Shotts, J., (University of Oklahoma) personal communication.
53. Natelson, S., and Shield, B., "X-ray Spectroscopy in the Clinical Laboratory, VI. Acid-Labile Protein-Bound Iodine (PBI)" Clin. Chem. 8, (1962) p. 17
54. Natelson, S., and Shield, B., "X-ray Spectrometric Determination of Strontium in Human Serum and Bone," Anal. Chem., Vol. 33, No. 3, (1961) p. 396.
55. Grant, C. L., "Spectrochemical Determination of Yttrium in Biological Materials," Analytical Chemistry, Vol. 33, No. 3, (1961) p. 401.
56. Lund, P. K., and Mathies, J. C., "X-Ray Spectroscopy in Biology and Medicine V. Total Serum Iodine," Am. J. Clin. Pathol. 40: (1963) p. 132.
57. Anspaugh, L. R., (UCRL-10873) "Chemical Elements in the Serum of Man in Health and Diabetes Mellitus. X-Ray Emission Spectrographic Determinations." (Thesis) Contract W-7405-ing-48. (1963) p. 78.
58. Gofman, J. W., "Chemical Elements of the Blood of Man in Health; X-Ray Spectrochemical Studies," Advan. Biol. Med. Phys. 8 (1962) p. 1.
59. Omnell, K. A., Lindstrom, B., Hoh, F. C. and Hammarlund - Esser, E., "Method for Nondestructive Determination of Inorganic and Organic Material in Mineralized Tissues." Acta radiol. 54 (1960) p. 209.
60. Lund, P. K., Morningstar, D. A., Mathies, J. C., "X-Ray Fluorescence Spectroscopy in Biology and Medicine," from (Liebhafsky, H. A.) X-Ray Absorption and Emission in Analytical Chemistry. John Wiley and Sons, (1960) p. 523.
61. Anspaugh, L. R., Gofman, J. W., Lowe, O. A., and Martin, W. H., "X-Ray Fluorescence Analysis Applied to Biological Problems," Second Symp. on Low Energy X- and Gamma Sources and Applications, University of Texas, Austin, Texas, (March, 1967).

62. Natelson, S. , Richelson, M. R. , Sheid, B. , and Bender, S. L. , "X-ray Spectroscopy in the Clinical Laboratory, I. Calcium and Potassium," Clin. Chem. 5, (1959) p. 519.
63. Natelson, S. , and Bender, S. L. , "X-ray Fluorescence as a Tool for the Analysis of Submicrogram Quantities of the Elements in Biological Systems," Microchem. J. , 3 (1959) p. 19.
64. Natelson, S. , and Sheid, B. , "X-ray Spectroscopy in the Clinical Laboratory, II. Chlorine and Sulfur - Automatic Analysis of Ultramicro Samples," Clin. Chem. 6, (1960) p. 299.
65. Mathies, J. C. , Lund, P. K. , and Eide, W. , "X-Ray Spectroscopy in the Clinical Laboratory, IV. Phosphorus - Total Blood Fe as a Measure of Hemoglobin Content," Anal. Biochem. 3 (1962) p. 408
66. Natelson, S. , and Sheid, B. , "X-Ray Spectroscopy in the Clinical Laboratory, III. S Distribution in the Electrophoretic Protein Fractions of Human Serum - Abnormalities Observed in Certain Disease States." Clin. Chem. 7, (1961) 115-129